

The Pennsylvania State University
The Graduate School
Department of Electrical Engineering

**NONLINEAR OPTICAL RESPONSES OF BLUE-PHASE LIQUID CRYSTALS
AND THEIR APPLICATIONS**

A Dissertation in
Electrical Engineering
by
Tsung-Jui Ho

Submitted in Partial Fulfillment
of the Requirements
for the Degree of

Doctor of Philosophy

December 2018

The dissertation of Tsung-Jui Ho was reviewed and approved* by the following:

Iam-Choon Khoo
William E. Leonhard Professor of Electrical Engineering
Dissertation Advisor
Chair of Committee

Victor Pasko
Professor and Coordinator of Graduate Program of Electrical Engineering

Zhiwen Liu
Professor of Electrical Engineering

Thomas E. Mallouk
Head of the Chemistry Department
Evan Pugh University Professor of Chemistry, Biochemistry and
Molecular Biology, Physics, and Engineering Science and Mechanics

Kultegin Aydin
Professor of Electrical Engineering
Head of the Department of Electrical Engineering

*Signatures are on file in the Graduate School

ABSTRACT

“Are they called ‘blue phases’ because they are in blue color?” This is the most common question asked by many people. The answer is yes but no. The name was given by the scientist who first observed the special liquid crystalline phase reflecting the color blue, however, the reflection color does not represent the phases. The major difference of blue-phase liquid crystal from other phases is their self-assembly three-dimensional photonic crystalline structure with a lattice constant typically around hundreds of nanometers, and their ability to show Bragg reflection over the visible spectrum.

At first, blue-phases were not popular because they are optically isotropic, i.e. no birefringence. However, they attracted wide attention over academic or industrial studies owing to their unique optical properties, such as a fast response time, being polarization-free, possessing no restriction on thickness, and having a self-assembly 3-D structure. Nowadays, scientists in chemistry are able to expand the temperature range from 1 K to almost 100 K and cover the room temperature. Therefore, blue phase are shown to be a promising material to overcome the disadvantage of typical liquid crystal materials.

In this dissertation, I will present a comprehensive study of nonlinear optical properties in blue-phase liquid crystal as well as their applications. First, ultrafast optical response of BPLC will be introduced. The results showed that pure transparent BPLC is capable of significantly attenuating a picosecond laser pulse with very high intensity. The mechanism is Maxwell stress-induced flow-reorientation effect. Owing to its tightly bounded structure, BPLC is a promising material for optical switching or optical limiter devices.

Furthermore, a detailed study of all-optical image processing with dye-doped BPLC will be revealed. Unlike typical nematic liquid crystals, blue phases are not restricted to sample thickness, and, therefore, Bragg grating condition can be applied to BPLC. The results showed that the diffraction efficiency of BPLC under holographic setup can provide results nearly one hundred times greater than that of the case with nematic liquid crystal. The high diffraction efficiency makes BPLC capable of many different applications, such as hologram reconstruction, phase conjugation, or photorefractive effect. Moreover, an interesting and simple way to prolong the grating memory is discovered, and the detail dynamical studies are shown in the dissertation.

TABLE OF CONTENTS

List of Figures	vii
Acknowledgements.....	xi
Chapter 1 Introduction of Liquid Crystals	1
1.1 Classification of Liquid Crystal Phase	3
1.2 Order Parameter	6
1.3 Birefringence of Liquid Crystals	9
1.4 Oseen-Frank Theory	11
1.5 Nonlinear Optical Response of Liquid Crystal.....	12
1.5.1 Optical Reorientation with Intense Short Pulses	15
1.5.2 Laser-Induced Flow-Reorientation.....	17
1.5.3 Density Effect	18
1.5.4 Photoisomerization in Liquid Crystals	20
Chapter 2 Blue-phase Liquid Crystal.....	21
2.1 Brief Introduction of BPLC	21
2.2 Theory of BPLC	24
Chapter 3 Ultrafast Optical Responses of BPLCs	27
3.1 Introduction of Optical Limiting	27
3.2 Introduction of Maxwell Stress in Liquid Crystal	32
3.2.1 Estimate of Optical Nonlinearity – Flat-Top Square Pulse	35
3.2.2 Estimate of Optical Nonlinearity – Gaussian Pulse	39
3.2.3 All-Optical Switching with Twist Nematic Alignment Cell	40
3.3 Laser-Induced Lattice Distortion in BPLC Cell	46
Chapter 4 Photorefractive Effect of BPLCs.....	51
4.1 Introduction of Photorefractive Effect.....	52
4.2 Sample Preparation and Experimental Setup	55
4.3 Experimental Result of Photorefractive Effect in BPLC.....	57
Chapter 5 High-Efficiency Bragg Grating with BPLCs	66
5.1 A Promising Holography Material: BPLC	67
5.2 Wave-Mixing Setup and Sample Preparation.....	71
5.3 High-Efficiency Diffraction Result and Dynamical Response of A-BPLC ...	73
5.4 Optically Prolong Memory Effect	82

5.5 Phase Conjugation Using A-BPLC	90
Chapter 6 Conclusion and Future Work	93
6.1 Optical Limiting with BPLC	93
6.2 Fast Optical Response with Bragg Grating In BPLC	95
6.3 Theoretical Simulation.....	96
References.....	98

LIST OF FIGURES

Fig. 1-1. Molecular structure of a typical liquid crystalline material .	4
Fig. 1-2. Chemical structure and phase transition temperature of 5CB.	5
Fig. 1-3. Spatial arrangement of four common liquid crystals. (a) Nematic. (b) Sematic (c) Cholesteric. (d) Blue phase.	6
Fig. 1-4. Order parameter dependence on temperature. The phase transition is from Crystal phase to Smectic A phase, Nematic phase, and Isotropic. Figure obtained from reference [13].	7
Fig. 1-5. Schematic depiction of polarizability ellipsoid for uniaxial liquid crystals. The optic axis is given by the director. The s direction denotes the light propagation direction.	10
Fig. 1-6. Birefringence of typical nematic liquid crystals in the visible-infrared wavelength region from reference [14].	10
Fig. 1-7. Elastic distortion in nematic liquid crystals.	12
Fig. 1-8. Interaction of a linear polarized laser with an aligned nematic liquid crystal film.	15
Fig. 1-9. Exemplary values for steady-state and effective nonlinear index coefficients and response times of major mechanisms for laser-induced refractive index modification of NLC from reference [18].	19
Fig. 1-10. Schematic figure of dye-doped nematic liquid crystals and the optical field direction.	20
Fig. 2-1. Microscopic image of blue-phase liquid crystal from reference [21].	22
Fig. 2-2. Schematic depictions of director distribution in nematic phase, cholesteric phase, and blue-phase	22
Fig. 2-3. Conceptual depiction: (a) director distribution in a DTC; (b) three-dimensional stacking of DTCs and the corresponding director distribution of the (c) continuous and (d) discontinuous portions; arrangements of DTCs and disclinations in (e), (f) BPI and (g), (h) BPII, obtained from reference [21].	23
Fig. 3-1. Schematic illustrations of optical limiting.	29
Fig. 3-2. MPE fluence for direct ocular exposure for a range of exposure durations, as per various wavelength ranges from reference [36].	30

Fig. 3-3. Side view of coherent optical wave mixing of two crossed-polarized lasers in a homeotropically aligned NLC cell.....	32
Fig. 3-4. Refractive index changes under different input intensity from reference [42].....	40
Fig. 3-5. Optical switching cell: Twist Nematic Liquid Crystal sandwiched between crossed polarizers.....	41
Fig. 3-6. Dynamical simulation of transmission under different input energies from reference [42].....	43
Fig. 3-7. Input versus output pulse shapes under different input pulse energies from reference [42].....	43
Fig. 3-8. (a) Oscilloscope traces of the input and output laser pulses for input laser energy = 109 μJ ; (b) input laser energy = 133 μJ from reference [42].....	45
Fig. 3-9. Plot of the radial dependence of the magnitude of the Maxwell stress associated with a Gaussian laser beam from reference [42].....	47
Fig. 3-10(a) Schematic depiction of the experiment set up for probing pulse laser induced flow and self-defocusing effect. (b) Measurement of the probe beam transmission showing the instant drop following by slowly recovering in [42]...	49
Fig. 4-1. Schematic depiction of the photorefractive effect along the spatial distribution.....	54
Fig. 4-2. Schematic depiction of the wave mixing experiment set up. Upper left photo shows the reflection colors corresponding to BPII and BPI phase of sample maintained at different temperatures. Upper right photo depicts the transmitted pump beams and diffractions under positive and negative DC biases.....	57
Fig. 4-3. Observed first-order (+1 and -1) diffractions as a function of increasing applied DC voltages from a 55- μm thick sample. [Error bars of <0.5% in each data point not shown]. In the voltage region between 40 – 140 V_{dc} , the asymmetry in the +1 and -1 diffraction powers is particularly evident from reference [52].....	58
Fig. 4-4. Observed Pump Beam 1 to Beam 2 ratio as a function of applied DC voltage, showing the beam coupling effect [Error bars of <0.5% in each data point not shown] from reference [52].....	63

- Fig. 4-5. Transmission spectra of a 55- μm thick BPLC cell maintained at BPII phase for two representative regions (a) and (b) of applied DC voltages with or without illumination by a 6 mW pump laser from reference [52]. 65
- Fig. 5-1. (a) Schematic of the Raman-Nath grating with multi-order diffraction and (b) Bragg grating with single order diffraction..... 68
- Fig. 5-2. Schematic depiction of the make-up of an azobenzene-doped blue-phase liquid crystal: (a) liquid crystal molecules in tightly wound double-twist cylinder; (b) BPI crystalline lattice; (c) BPII crystalline lattice; (d) enlarged view of the crystalline lattice and defect region where majority of dopant dye molecules aggregate, and participate actively in laser-induced lattice distortion (e) Photograph of the BPLC placed on top of the Air Force resolution chart; reddish coloration is due to the CPND-57 azo-dopant in BPLC; (f) Same as (e) but photo is taken with flash and exhibits more color display and contrast from the two blue-phase regions [regions of sample deliberately maintained at different temperatures] from reference [67]. 70
- Fig. 5-3. Schematic depiction of the experimental setup for the wave-mixing and grating formation. The phase matching condition is shown at the upper-right diagram involving two pump beams ($\lambda=532\text{nm}$) and two probe beams ($\lambda=633\text{nm}$). P: polarizer; BP: a-BPLC sample; S: mechanical shutter; BS: beam splitter; $\lambda/2$: half-wave plate; D: photodetector; M: mirror]. The photo insert on lower left corner shows the writing beams, the probe beam and the diffracted beam on the screen from reference [67]...... 73
- Fig. 5-4. Typical dynamical evolution of the probe diffraction with step-on/off writing beams for beam powers: 3.2 mW and 3.7 mW; samples maintained in BPII phase. Similar results are obtained in BPI phase. (a) 5 s writing time, showing a smooth build up and decay (b) 8 s writing time, showing an abrupt increase when the writing beams are turned off. (c) Plot of the diffraction signal showing the sharp spike centered at the phase-matched angle, obtained from reference [67]...... 76
- Fig. 5-5. (a) Time evolution of the diffraction signals in BPI and BPII phases for gated (1 second square pulse) writing beams at different temperatures. Sample thickness: 1 mm; grating spacing: 2 μm . Pump beam input powers at sample: ~ 7.5 mW. (b) Peak diffraction efficiency as a function of the sample temperature from reference [76]. 78
- Fig. 5-6. Peak diffraction efficiency in BPII as a function of the writing beam pulse width. (a) Grating spacing: 4 μm ; temperature: 28.8°C; pump beam power: 5 mW. (b) Grating spacing: 2 μm ; temperature: 28.4°C; pump beam power: 15 mW from the reference [76]. 79

- Fig. 5-7. Comparison of the diffraction efficiency from BPLC (BPI near the BPI–BPII transition point) and NLC samples. (Left) Both samples. Thickness: 100 μm thick; dopant: methyl red; pump beam power $\sim 1\text{ mW}$; probe beam 1.5 mW. (Right): BPLC thickness: 1 mm; NLC thickness: 100 μm ; dopant: CPND-57 (BPLC), methyl red (NLC). In the case of NLC, the incident laser polarization is set to be parallel (\parallel) or perpendicular (\perp) to the director axis n from the reference [76]. 80
- Fig. 5-8. Observed dependence of the maximum Bragg diffraction efficiency on the sample temperature in the BPI-BPII phases. Writing beam powers: 5.5 mW and 4.8 mW; writing time: 2 seconds from the reference [67]. 81
- Fig. 5-9. (a) BPII phase, one beam on for 2 seconds and switched off while the other beam is kept on for 55 seconds. Writing beam powers: 2.4 and 2.1 mW. (b) Same as (a) but for writing beam powers: 3.6 and 3.1 mW. (c) BPI phase, one beam on for ~ 6 seconds and switched off while the other beam is kept on for ~ 45 seconds. Writing beam powers: 2.4 and 2.1 mW. (d) Same as (c) but for writing beam powers: 3.6 and 3.1 mW. Dotted line indicates how the diffracted signal would persist for another 2 to 3 minutes if the reference beams are not switched off. In all cases, when the second beam is turned off, the diffraction signal disappears in <5 sec from reference [67]. 83
- Fig. 5-10. Schematic depiction of the optical intensity grating, cis-isomers population grating, and lattice distortion grating for various time regimes 86
- Fig. 5-11. Transmission spectra exhibiting photonic bandgap (transmission dips) of the 1-mm thick A-BPLC sample illuminated by a 532-nm pump beam intensity $\sim 15\text{ mW/cm}^2$ (pump power $\sim 1.5\text{ mW}$). The spectra are normalizing with the transmission spectrum of the sample in the isotropic (liquid) phase. Photo inserts show the different reflection colors from the regions under prolonged laser illumination at higher pump intensity $\sim 80\text{ mW/cm}^2$ for BPI and BPII phase, obtained from reference [67]. 89
- Fig. 5-12. (a) Schematic depiction of the experimental setup for optical phase conjugation by degenerate four wave mixing in A-BPLC. (b) Photograph of the input object. (c) Reconstructed image without the aberration. (d) Input object beam after traversing the corrugated plastic film exhibiting severe aberration. (e) Reconstructed image that demonstrates the ability of optical phase conjugation to correct for the aberration from reference [76]. 92
- Fig. 6-1. Schematic depiction of the various mechanisms that could come into play in affecting the transmission of a laser pulse through a BPLC cored constituent fiber in a BPLC fiber array for passive sensor protection applications[42]. 94

ACKNOWLEDGEMENTS

Foremost, I would like to express my sincere gratitude to my advisor, Prof. Iam-Choon Khoo, for his guidance, patience, encouragement and being my mentor. I will always remember the days he spent in the lab with everyone doing the experiment. The passion in his eyes is the most inspiring feeling I have ever seen. It is my great honor to work under his supervision. Without his help and guidance, my journey of PhD degree wouldn't be that smooth.

I also would like to thank Chun-Wei Chen for all his help on my research. He is the most smart and unselfish friend of my life and I appreciate his assistance on my experiment and providing me the precious opinion. And I am also grateful for Dr. Shuo Zhao helping me with everything when I first came to Penn State.

I would like to also acknowledge all the friends supporting me through the whole journey. It is great to have them accompany for the last four years.

Finally, I would like to express my greatest appreciation to my mom. She is my only family and the one always supports me with all my decision.

There is a quote from my advisor, Dr. Iam-Choon Khoo, that I want to use to close my acknowledgment. These words help me go through many difficulties, not only in research but also in my life:

“Just try it, you never know what the result would be!”

Chapter 1

Introduction of Liquid Crystals

Liquid crystal (LC), as its name implies, is the material transition occurred from the ordered crystalline phase to the disordered liquid phase, and it was first noted in a cholesteric material by a botanist, F. Reinitzer, in 1888 [1]. However, it was not until the 1950s when F.C Frank and others pursued further progress to create a greater understanding in liquid crystals [2]. Such materials exhibit interesting optical properties that are useful for electro-optic elements with low optical power requirement, low cost, and large birefringence [3-9]. In this chapter, we will introduce the basic properties of liquid crystals as well as the nonlinear optical response of LCs in different condition.

In this dissertation, a comprehensive study of the unique type of liquid crystalline phase blue-phase liquid crystals (BPLC) will be presented. First, a brief introduction of liquid crystalline materials will be covered in Chapter 1, including basic mechanisms, liquid crystalline formation, and nonlinear optical response in LC.

Chapter 2 provides a deeper understanding of the photonic crystalline structure in BPLC and the unique optical properties of it. BPLC is a naturally formed 3-D photonic crystalline material, and it has some advantages, such as being polarization- and alignment-free, possessing a faster response, and being capable of a thick sample.

Chapter 3 is the experimental result of the nonlinear optical response in BPLC under intense laser pulse. The focused Gaussian laser beam generates a so-called Maxwell

stress in a pure BPLC sample and, therefore, forms a volcano-shaped refractive index profile by lattice distortion of the BPLC. The lattice distortion further induced flow-reorientation and, finally, de-focusing of the input field. The results indicate that BPLC has a very fast response under picosecond laser pulses, which makes it a promising candidate of optical limiting devices. The research results are published and documented in the journal of Progress In Electromagnetics Research as shown in [10]

Chapter 4 shows the photorefractive effect in fullerene- C_{60} -doped BPLC. The detail of the experiment is introduced in this section as well as the analyzation of the dynamical response of the diffraction signal in the wave-mixing experiment. Moreover, we demonstrated the two-beam coupling effect, i.e. beam energy transferring. The detail of the research is shown and published in [52].

Chapter 5 provides a new discovery of the BPLC in holographic application. BPLC was found to be capable of high-efficiency Bragg grating formation. The diffraction efficiency is around 70%, unlike 1% in nematic liquid crystal, and only one order diffraction is presented because of the condition in Bragg grating regime. The huge improvement of diffraction efficiency now makes BPLC a very promising material for holographic display or holographic storage systems. A detailed explanation of the dynamics under the wave-mixing setup will be discussed. Furthermore, we found an interesting and simple way to prolong the grating memory by simply leaving one of the pump beams on and having the BPLC illuminate uniformly. Also, phase conjugation results will be shown in the chapter. The experimental results are published in the journal of Scientific Report and Liquid Crystals as shown in [11, 12].

Finally, Chapter 6 presents the conclusion of the research on BPLC and provides ideas for future studies. Many research groups are interested in this material because of the unique optical properties and trying to develop the new applications based on BPLC.

1.1 Classification of Liquid Crystal Phase

Liquid crystals represent an intermediate phase between the traditional liquid and solid crystal. The so-called “mesogens” possess the physical properties characteristic of crystals and hydrodynamic of liquid. Typically, liquid crystals can be classified into three types: lyotropic, polymeric and thermotropic. Lyotropic LCs undergo phase transition as a function of both temperature and concentration. The main variable of phase control is the amount of solvent (usually water). Polymeric LCs are characterized by the degree of flexibility, which is useful for optical storage applications. Of the three types of LCs, thermotropic LCs are the most widely used. The phases are decided by the function of temperature. Their linear optical effect dominates the electronic display applications, and the nonlinearities are also extremely large. Typical thermotropic LCs, such as 4-pentyl-4'-cyanobiphenyl (5CB) and 1-1'-biphenyl (E7), are composed of rod-like molecules (i.e. rigid rod). At the condition of the temperature over clearing point (T_c), the molecules are randomly distributed. However, between a range of temperature, the LC's molecules can self-orientate into a certain direction, and the director axis are normally described as a vector field \mathbf{n} , which will be discussed later.

Most of the liquid crystal molecules have the chemical structure as shown in Fig. 1-1. The basic formation of liquid crystal molecules is composed of two aromatic rings (e.g. biphenyl, phenyl, or others) connected with a linkage group. The linkage group can be a tolane, ester, or Schiff base, and the group typically determines the chemical stability in the molecules. The side chain and terminal group can be cyano, alkyl, or others.

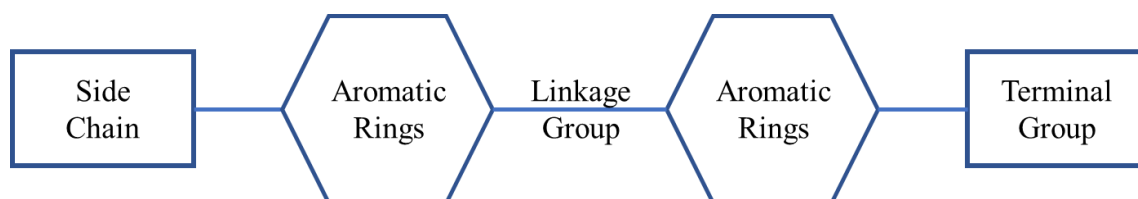


Fig. 1-1. Molecular structure of a typical liquid crystalline material.

Take a common liquid crystal, 5CB, for an example. Its molecule consists of a cyano terminal group, an alkyl side chain, and two phenyl rings. As mentioned above, 5CB is a thermotropic type of liquid crystal, and the phase is determined by the temperature. Figure 1-2 shows the phase transition diagram of 5CB. The nematic phase exists between 18°C to 35°C.

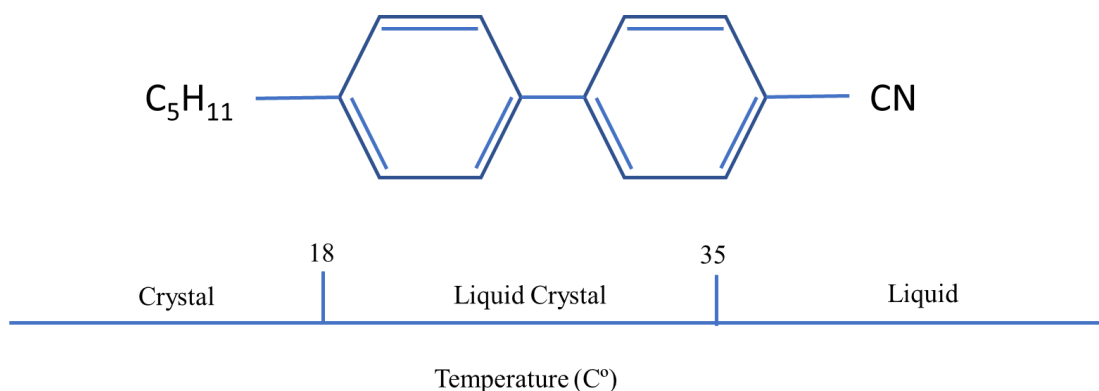


Fig. 1-2. Chemical structure and phase transition temperature of 5CB.

Thermotropic liquid crystals are most widely used for both scientific research and industrial application, such as displays or photonic devices. Typical LC molecules are rod-like, as depicted in Fig. 1-3, and the directional orientation of the molecules are described as the director axis \hat{n} .

The common mesophases of thermotropic LCs are smectic, nematic, cholesteric, and blue phase. The first, nematic, is the most-used type of LC for the display industry. In this phase, molecules tend to align themselves with the director axis. Note that liquid crystals are centrosymmetric, meaning the physical properties are the same in $+\hat{n}$ and $-\hat{n}$ direction. In smectic phase, a degree of orientational and positional order are required. The molecules tend to align in layers. Cholesteric liquid crystals are formed by the assistance of chiral dopant, and the pitch is the key parameter to determine their property.

Finally, blue-phase liquid crystal is a unique kind of phase that only exists in highly chiral materials. The phase exhibits between the cholesteric phase and the isotropic phase,

and the structure is a self-assembly 3-D photonic crystal. The detailed explanation will be covered in the next chapter.

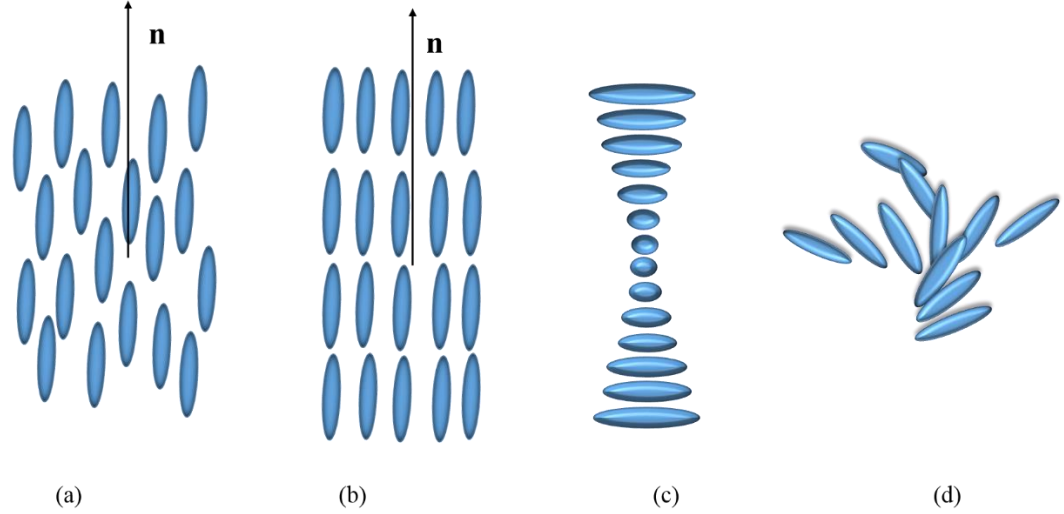


Fig. 1-3. Spatial arrangement of four common liquid crystals. (a) Nematic. (b) Smectic (c) Cholesteric. (d) Blue phase.

1.2 Order Parameter

To describe the physical properties of liquid crystals, it is important to find a theory to explain the coexistence of liquid and solid. The most-used theory is elastic continuum theory [2, 13, 14]. Although there are a wide variety of liquid crystal phases, their physical properties can be simply described by so-called order parameter, i.e. a unit length vector field \hat{n} . The unit vector is further used to explain the order parameter by Tsvetkov [15] in the following equation:

$$S = \frac{1}{2} \langle 3 (\hat{k} \cdot \hat{n})(\hat{k} \cdot \hat{n}) - 1 \rangle = \frac{1}{2} \langle 3 \cos^2 \theta - 1 \rangle, \quad (1-1)$$

where \hat{k} is the rotation symmetric axis and θ is the angle between the axis of the single molecule and the director axis of the liquid crystals. The dependence of the order parameter on temperature is shown in Fig. 1-4 [13].

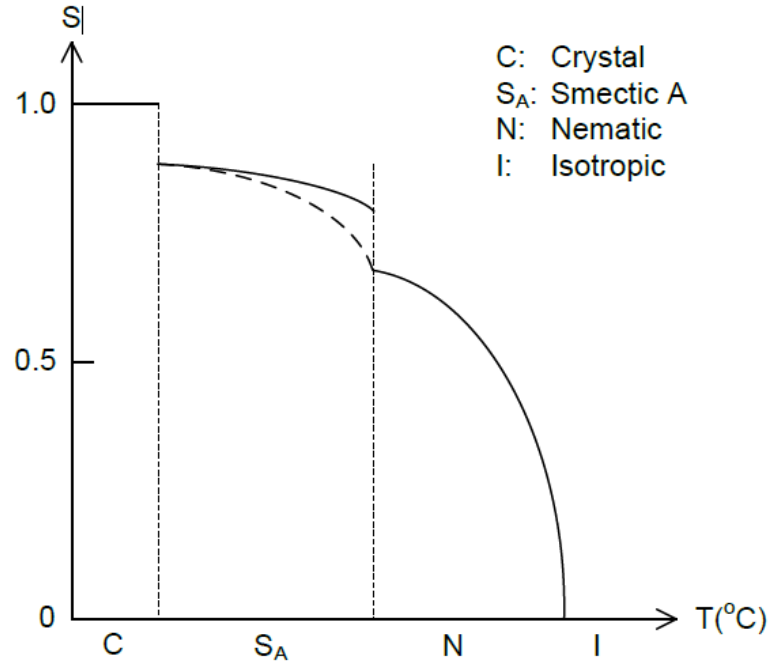


Fig. 1-4. Order parameter dependence on temperature. The phase transition is from Crystal phase to Smectic A phase, Nematic phase, and Isotropic. Figure obtained from reference [16].

The bracket in Eq. 1-1 is an average in the entire assembly of the material. For the case of perfect molecular alignment, ($\langle \cos^2 \theta \rangle = 1$), the value of $S = 1$. Conversely, in the

isotropic phase where the molecules are completely randomly aligned, $\langle \cos^2 \theta \rangle = 1/3$ and $S = 0$. Typically, the liquid crystalline phase is located at between these two limits, and the maximum value of S in nematic liquid crystal, for example, is around 0.6~0.7.

1.3 Birefringence of Liquid Crystals

Uniaxial material exhibits an elliptical refractive index profile, as shown in Fig. 1-5. For rod-like liquid crystal molecules, two refractive indices can be observed; n_o represents the “ordinary” index that the electric field of incident ray is oscillating perpendicular to the optical axis of LC molecule, and n_e is the “extraordinary” index that the electric field oscillating parallel to the axis. The birefringence is given by:

$$\Delta n = n_e - n_o = n_{\parallel} - n_{\perp}, \quad (1-2)$$

and, for an arbitrary oriented director axis, the extraordinary refractive index is

$$n_e(\theta) = \frac{n_{\parallel} n_{\perp}}{[n_{\parallel}^2 \cos^2 \theta + n_{\perp}^2 \sin^2 \theta]^{\frac{1}{2}}}. \quad (1-3)$$

Moreover, the large birefringence of a liquid crystal covers a very broad spectral range from near ultraviolet to near infrared (400nm ~ 1.2 μ m) with a value around 0.2 as shown in Fig. 1-6 [17].

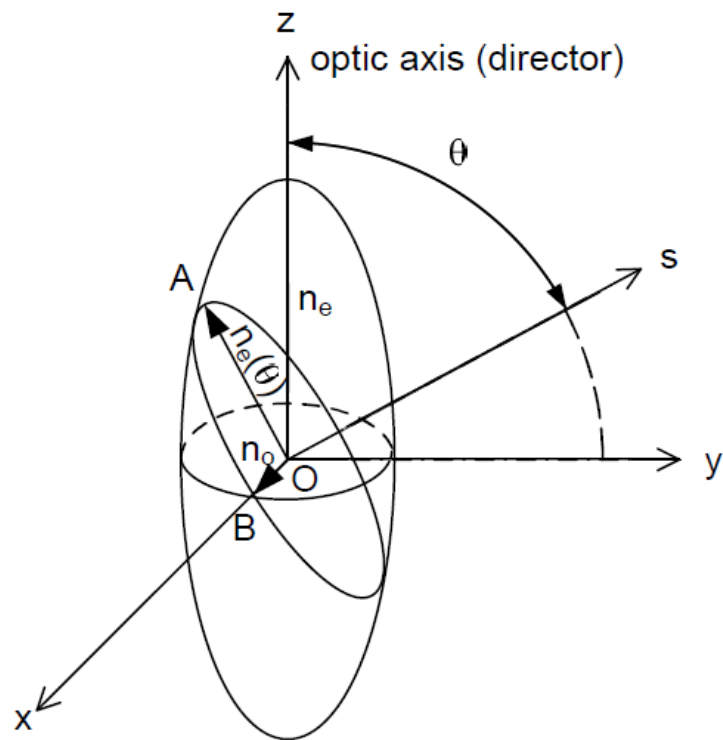


Fig. 1-5. Schematic depiction of polarizability ellipsoid for uniaxial liquid crystals. The optic axis is given by the director. The s direction denotes the light propagation direction.

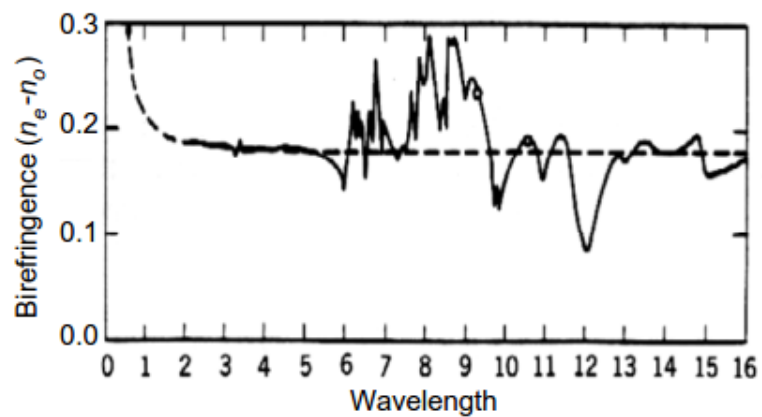


Fig. 1-6. Birefringence of typical nematic liquid crystals in the visible-infrared wavelength region from reference [17].

1.4 Oseen-Frank Theory

In liquid crystals, an external electrical field or optical field can produce many kinds of axis orientations. Therefore, it is important to understand the physical movement and the underlying theory. Using the nematic liquid crystals as a sample, three major elastic distortions of the director field are splay, twist, and bend, as shown in Fig. 1-7. Those movements can be described by the director axis associated with free energy density [14]:

$$\text{Splay: } F_1 = \frac{1}{2} K_1 (\nabla \cdot \vec{n})^2 \quad (1-4)$$

$$\text{Twist: } F_2 = \frac{1}{2} K_2 (\vec{n} \cdot \nabla \times \vec{n})^2 \quad (1-5)$$

$$\text{Bend: } F_3 = \frac{1}{2} K_3 (\vec{n} \times \nabla \times \vec{n})^2 \quad (1-6)$$

where K_1 , K_2 , K_3 are presenting Frank splay, twist, and bend elastic constant, respectively. Here, \vec{n} and $-\vec{n}$ share the same physical properties since nematic liquid crystals are uniaxial. Liquid crystals prefer to align in one of uniform orientation with lowest free energy of each elastic distortion, leading to the Frank free energy density [2]:

$$F_{Frank} = \frac{1}{2} K_1 (\nabla \cdot \vec{n})^2 + \frac{1}{2} K_2 (\vec{n} \cdot \nabla \times \vec{n} + q_0)^2 + \frac{1}{2} K_3 (\vec{n} \times \nabla \times \vec{n})^2 \quad (1-7)$$

The constant q_0 added in Eq. 1-7 appears when the system is lacking inversion symmetry, i.e., in chiral liquid crystals. In such a chiral system, this constant will not be

zero and produces a twist distortion with $\vec{n} \cdot \nabla \times \vec{n} = q_0$. In addition, the repeat length of the liquid crystals rotating by 180° is defined as π/q_0 , known as pitch.

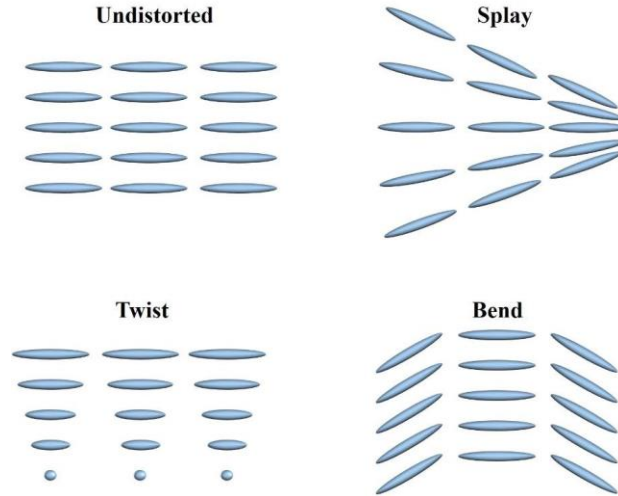


Fig. 1-7. Elastic distortion in nematic liquid crystals.

1.5 Nonlinear Optical Response of Liquid Crystal

Liquid crystalline dynamic movements, such as axis orientation, density, flow, or thermal effect, produce the optical nonlinear effect. It is, however, complicated. The simplest model uses nematic liquid crystals to describe the theory because of the simpler geometric shape. Since the nematic liquid crystalline molecules are anisotropic, a polarized light can induce the axis reorientation, or reordering of the phase, causing refractive indices to change, which can be characterized by electronic and non-electronic effect.

The nonlinear optic start with the electrical field induced polarization is shown below:

$$\vec{P}^{NL} = \varepsilon_0 \chi^{(2)} \vec{E} \vec{E} + \varepsilon_0 \chi^{(3)} \vec{E} \vec{E} \vec{E} + \dots, \quad (1-8)$$

where $\chi^{(n)}$ is the nth order susceptibility and ε_0 is the dielectric constant of the liquid crystals. In order to understand to light-matter interaction, the wave equation needs to involve

$$\nabla^2 \vec{E} - \mu \varepsilon \frac{\partial^2 \vec{E}}{\partial t^2} = \mu_0 \frac{\partial^2 \vec{P}^{NL}}{\partial t^2} \quad (1-9)$$

Because the director axis of liquid crystals is indistinguishable between \vec{n} and $-\vec{n}$, the second-order susceptibility is vanished in centrosymmetric materials, such that the most nonlinear effect is associated with $\chi^{(3)}$ [18-20]. Therefore, the refractive index can by written as:

$$n = n_0 + \frac{3\chi^{(3)}}{\varepsilon_0 c n_0^2} I \equiv n_0 + n_2 I \quad (1-10)$$

This equation leads to the major mechanism, the Kerr effect, in which the laser-induced refractive indices change is proportional to light intensity and nonlinear coefficient n_2 . Since $\chi^{(3)}$ is relatively small, typical third order susceptibility values for liquid crystals are around $10^{-18} \text{ m}^2/\text{V}^2$ [21], the large intensity is required to generate

sufficient effect. In this case, short pulses and a high-intensity laser field are needed. The comparison of nonlinear coefficients and switching efficiency $\chi^{(3)}/\alpha t$ is list below in table 1 and table 2, α is the absorption coefficient and t is response time of the nonlinear effect [16].

Materials	Order of magnitude of n_2 (cm^2/W)
Nematic liquid crystal	
Purely optically induced	$\sim 10^{-4} - 10^{-3}$
Thermal and order parameter change	$\sim 10^{-5} - 10^{-3}$
Excited dopant (dye molecule) assisted	$\sim 10^{-1} - 10^{-3}$
Photorefractive - C60 doped	$\sim 10^{-3} - 10^{-2}$
Methyl-red doped	$\sim 1 - 2000$
Azobenzene LC (BMAB) doped NLC	$> 10^{-2} - 10^{-1}$
C60/nanotube doped film	$> 10^{-2} - 10^{-1}$
OASLM-LC [estimated]	$\sim 10 - 200$
Electronic non-resonant nonlinearities	$\sim 10^{-13} - 10^{-12}$
GaAs bulk	$\sim 10^{-5}$
GaAs Multiple Quantum Well MQW	$\sim 10^{-3}$
Photorefractive crystals/polymers	$\sim 10^{-4}$
Bacteriorhodopsin	$\sim 10^{-3}$

Table 1-1. Nonlinear refractive index coefficients of liquid crystals and some optoelectronics materials from reference [16]

Materials [Ref.]	$\chi^{(3)}/\alpha\tau$ ($10^{-10} \text{ m}^3 \text{ V}^{-2} \text{ s}^{-1}$)
GaAs bulk	30
GaAs MQW	300
Bacteriorhodopsin	0.05
Photorefractive crystals/polymers	10^{-1}
methyl-red doped LC film	> 100
C60/nanotube doped LC film	> 100
OALC SLM	> 100

Table 1-2. Switching efficiency of various materials [16]

1.5.1 Optical Reorientation with Intense Short Pulses

Consider the exemplary light interaction configuration in Fig. 1-8, where the liquid crystals are aligned perpendicular to the surface boundary with a small angle β . Under the illumination of a polarized plane wave in z-direction, the director axis experiences a shift in x-z plane by an angle θ , where the director axis vector field is described as $[\sin(\theta+\beta), \cos(\theta+\beta)]$.

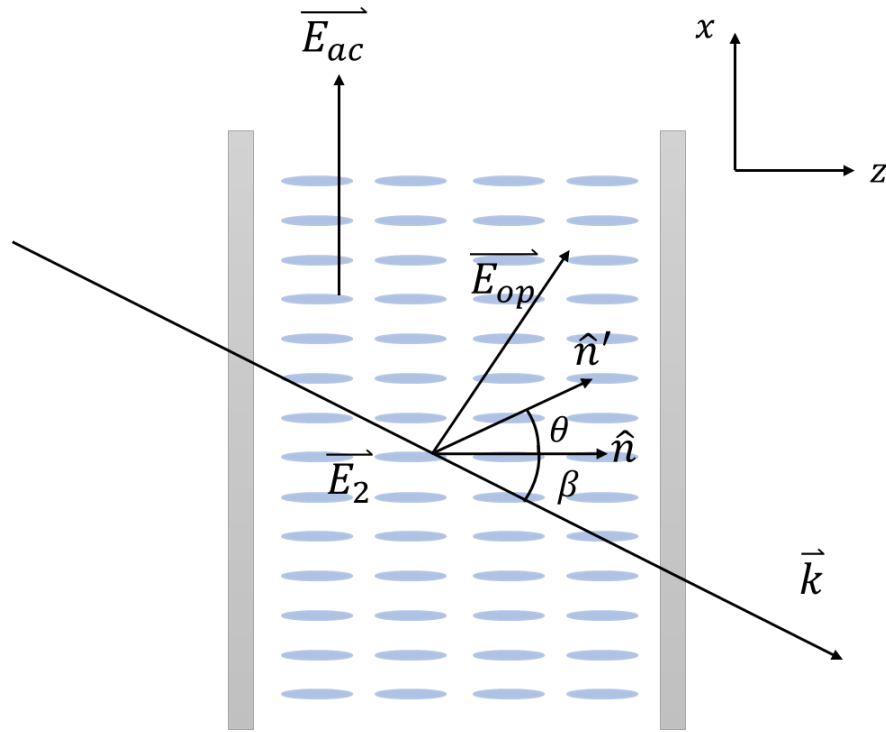


Fig. 1-8. Interaction of a linear polarized laser with an aligned nematic liquid crystal film.

Based on previous studies, the dynamic equation of field-induced axis orientation can be interpreted as in:

$$\gamma_1 \frac{d\theta}{dt} = K \frac{d^2\theta}{dz^2} + \varepsilon_0 \Delta \varepsilon E_{op}^2 \sin 2\beta, \quad (1-11)$$

where we apply the one elastic constant approximation $K_1=K_2=K_3=K$, and $\theta \gg \beta$ [22]. γ_1 is the viscosity coefficient. Consider that the laser pulse is a flat top square pulse (i.e., $E_{op}^2(t) = E_{op}^2$ for $0 < t < \tau_p$, $E_{op}^2(t) = 0$ elsewhere.). The solution of $\theta(t)$ is

$$\theta(t) = \tau_\theta \varepsilon_0 \Delta \varepsilon E_{op}^2 (\sin 2\beta) (1 - e^{-t/\tau_\theta}) \quad (1-12)$$

For a short pulse ($\tau_p \ll \tau_\theta$), we can find that $\theta(t)$ is proportional to t/τ_θ .

Therefore, the refractive index changes, $\Delta n(t)$ is proportional to $(t/\tau_\theta) \Delta n_{ss}$, and the response time τ_R can be defined as the time it takes for the maximum phase shift, which is inversely proportional to the light intensity.

$$\tau_R \propto 1/I_{op} \quad (1-13)$$

The relaxation time may be in the millisecond time region, while the time for intense laser induced axis reorientation can be in sub-nanosecond range, depending on the input. For a typical Nd:YAG laser with 10 ns pulses, the effective n_2 is $4 \times 10^{-12} \text{ cm}^2/\text{W}$.

1.5.2 Laser-Induced Flow-Reorientation

Since the liquid crystals contain the physical properties of hydrodynamic, a high-intensity pulse laser can induce flow reorientation due to two major mechanisms: Maxwell stress and electrostriction. This interaction is also a promising way to achieve all-optical switching and optical limiting. In transparent nematic liquid crystals, free charges exist due to the impurities where the Maxwell stress is applied as:

$$F_E = (\nabla \cdot D)E^* - D \times \nabla \times E^* \quad (1-14)$$

By putting Eq. 1-14 into the flow reorientation process as a driving force, we can get a hydrodynamic equation in a transient state:

$$\mu \frac{\partial^2 \theta}{\partial t^2} + \gamma_1 \frac{\partial \theta}{\partial t} - K \Delta \theta - \frac{1}{2} (\gamma_1 - \gamma_2 \cos 2\theta) \frac{\partial v_x}{\partial y} = 0 \quad (1-15)$$

$$\rho_0 \frac{\partial v_x}{\partial t} - \gamma_s \Delta v_x = F_x \quad (1-16)$$

Here, μ is the moment of inertia, K is the elastic constant, v_x is the flow velocity (in the x-direction), and γ_s , γ_1 , and γ_2 are the viscosity coefficients. The driving force F_x is from Maxwell stress in the x-direction.

Assuming the incident-polarized light is a square top pulse, the flow-reorientation equation can be solved, and, therefore, the rise time of the laser induced orientation process τ_R can be found. The typical value of τ_R is around the nanosecond range (~ 500 ns) in nematic liquid crystals. The importance of this mechanism is that the axis reorientation

is sensitive to light intensity instead of laser frequency, meaning this effect is capable of all-optical switching and limiting applications in the microseconds or nanoseconds time scale [23, 24].

1.5.3 Density Effect

As in many other materials, the nature of optical absorption in liquid crystals depends on wavelength. Under the intense laser pulses in transparent NLC, the electrostriction effect can explain the dynamic of laser-induced density fluctuation (i.e., the movement of a dielectric material into the region of high field strength). In Section 1.5.2, Maxwell stress is introduced in the condition that liquid crystals are an incompressible liquid. However, there are also expansions and contraction manifesting the crystalline properties where the electrostriction is applied. This kind of effect causes the density change in liquid crystals by a high electric field.

In the typical grating diffraction setup, the field-induced density modulation created by a square top laser pulse is given by:

$$\rho^e(t) = \frac{\gamma^e E_0^2}{4\pi v^2} \left(1 - e^{-\frac{t}{\tau_B}} \cos \Omega t \right); \quad \tau_B = \frac{2\rho_0}{\eta q^2} \quad (1-17)$$

Here, $\rho^e(t)$ is proportional to γ^e and is characterized by the Brillouin relaxation constant τ_B and frequency Ω , where $\Omega = \sqrt{q^2 v^2 - \tau_B^{-2}}$. Taking nematic liquid crystals as

an example, $\eta = 7 \times 10^{-2} \text{ kg/m} \cdot \text{s}$, $\rho_0 = 10^3 \text{ kg/m}^3$, the grating period of $20 \text{ } \mu\text{m}$, and $\tau_B \sim 200 \text{ ns}$.

Figure 1.9 summarizes the major nonlinear effect that contributes to optical switching and provides the time scale. Here, having multiple time scales corresponds to a different nonlinear coefficient, n_2 , indicating the mechanism is chosen according to the optical field we use [22].

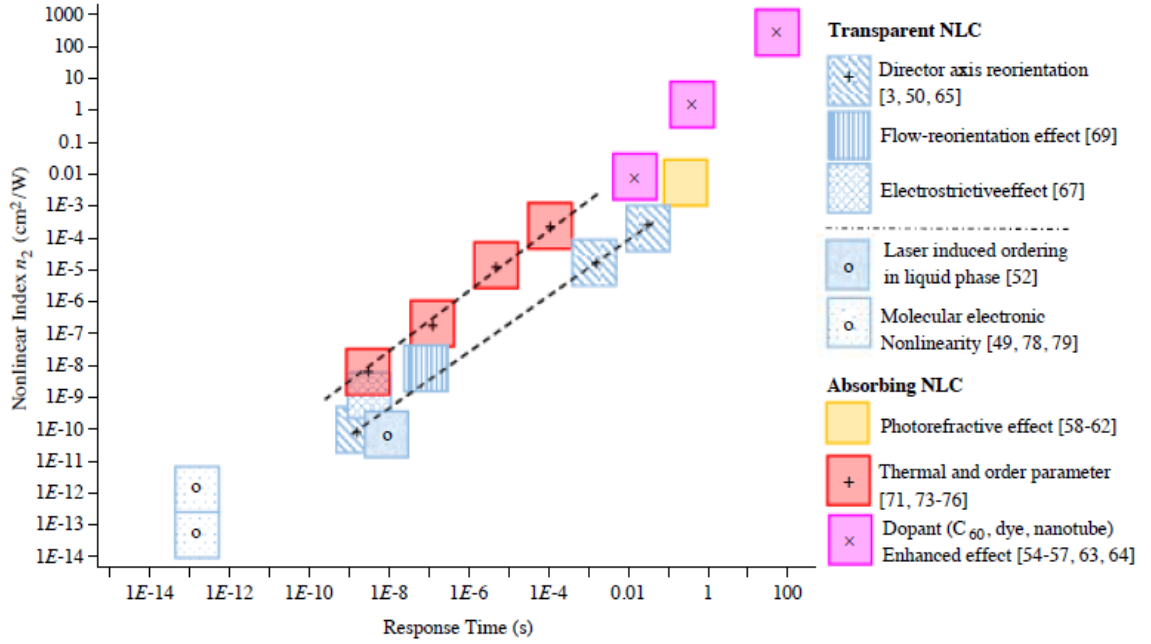


Fig. 1-9. Exemplary values for steady-state and effective nonlinear index coefficients and response times of major mechanisms for laser-induced refractive index modification of NLC from reference [22].

1.5.4 Photoisomerization in Liquid Crystals

Photoisomerization is the molecular behavior of structural change between isomers caused by photoexcitation. The most-widely investigated material is azobenzene, where the optical input can produce trans-cis transition and are mostly reversible. Liquid crystals' films containing photosensitive dopants exhibit large nonlinear properties, such as optically tunable refractive index [23], image storage, or optical switching [24].

The trans state of azobenzene is rod-like, which can stabilize the liquid crystals. On the other hand, the cis state is bent and able to disorientate the local liquid crystals and cause director axis orientation effect, and, therefore, can generate the refractive index change. Here, the dye molecules will align themselves in the direction orthogonal to the optical electric field. As shown in Fig. 1-10, the azobenzene molecules (i.e. the red rod) intend to rotate to the \hat{z} or \hat{y} direction if the optical field is on the \hat{x} direction. Additionally, the intermolecular torque acting on liquid crystals can be stronger than optical torque. Moreover, since the trans-cis isomerism is a fast process, typically in the nanosecond range, the liquid crystal phase transition can be created just as rapidly.

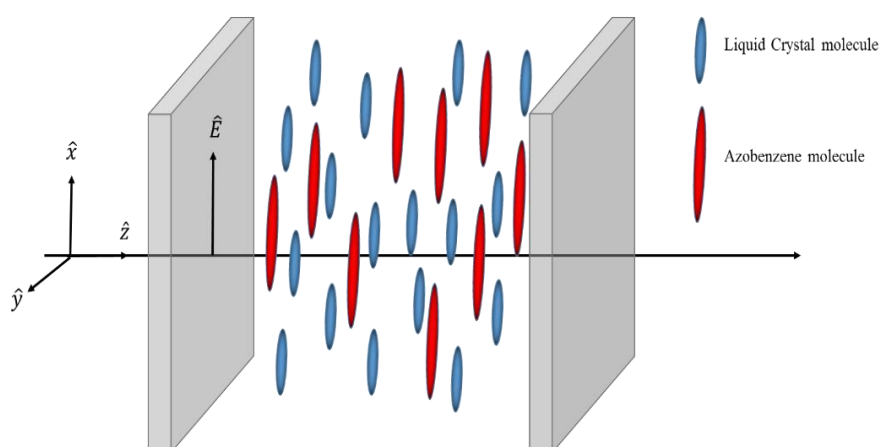


Fig. 1-10. Schematic figure of dye-doped nematic liquid crystals and the optical field direction.

Chapter 2

Blue-phase Liquid Crystal

Blue-phase liquid crystals (BPLC) have brought huge attraction to research groups in recent years due to their unique optical properties and periodic structure. BPLC is a promising material for many applications, such as display, photonic devices, light modulator, and optical filter as a result of their self-assembly 3-D structure. This chapter will introduce the basic material properties and their formation. Additionally, the Oseen-Frank free energy model will be applied to explain the structure of BPLC. Finally, the unique electro-optical mechanism will be shown.

2.1 Brief Introduction of BPLC

Blue-phases were first observed by Reinitzer [1] in highly chiral liquid crystals with a narrow temperature range between the isotropic and cholesteric phases in 1888. This remarkable mesophase exhibits a colorful texture of micron-sized platelets, as shown in Fig. 2-1 [25]. The colorful reflection is due to selective reflection from periodic structures, such as a typical crystal structure. The reflection spectra show that the Bragg reflection peaks are indexed by the lattice constant within the three-dimensional structure of several hundred nanometers. Blue-phases are not really a crystal in the traditional sense; BPLCs do not have a long range of positional order, and they are still fluid [26].

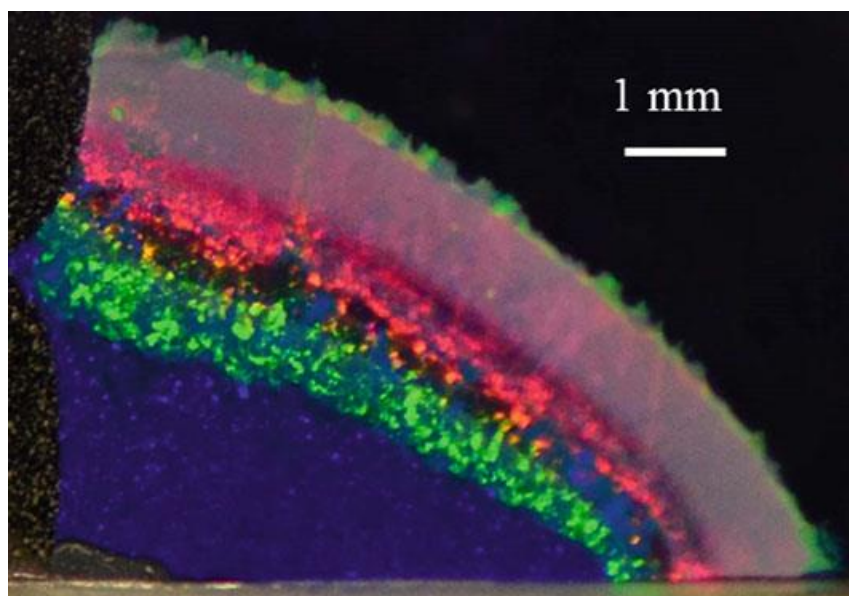


Fig. 2-1. Microscopic image of blue-phase liquid crystal from reference [25].

The key to understanding the formation of blue-phases involves the double twist structure in the highly chiral liquid crystals, as shown in Fig. 2-2 [27-29]. One can see the double twist cylinder (DTC) as multiple chiral helixes simply added together. Usually, when the chirality in the system is high enough, a double twist structure is more stable than a simple helical system.

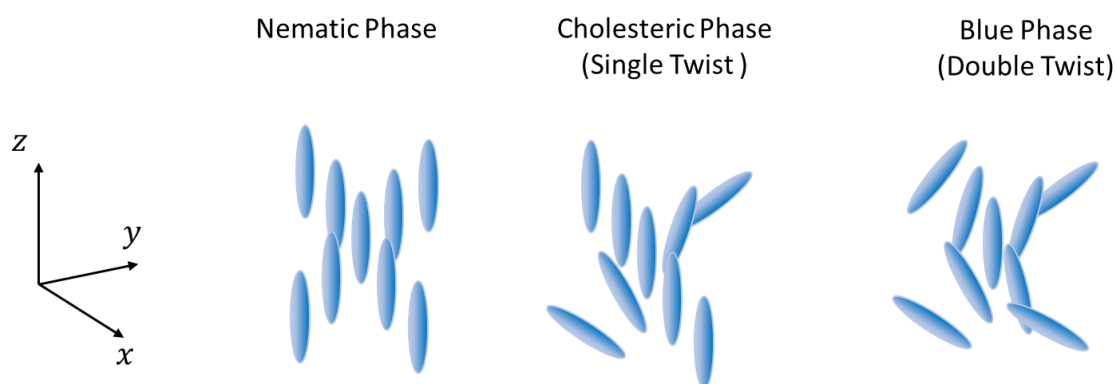


Fig. 2-2. Schematic depictions of director distribution in nematic phase, cholesteric phase, and blue-phase

Moreover, the double twist cylinders are separated by a network of disclinations, as shown in Fig. 2-3 [25]. The blue-phases are delicately balanced crystalline system of defect structure [30, 31]. Three distinct blue-phases have been shown experimentally, with blue-phase III, blue-phase II, blue-phase I occurring in the order of cooling from isotropic state [32, 33]. The crystalline structures in blue-phases are body-centered-cubic for BPI, simple-cubic for BP II, and amorphous structure close to isotropic for BPIII [30].

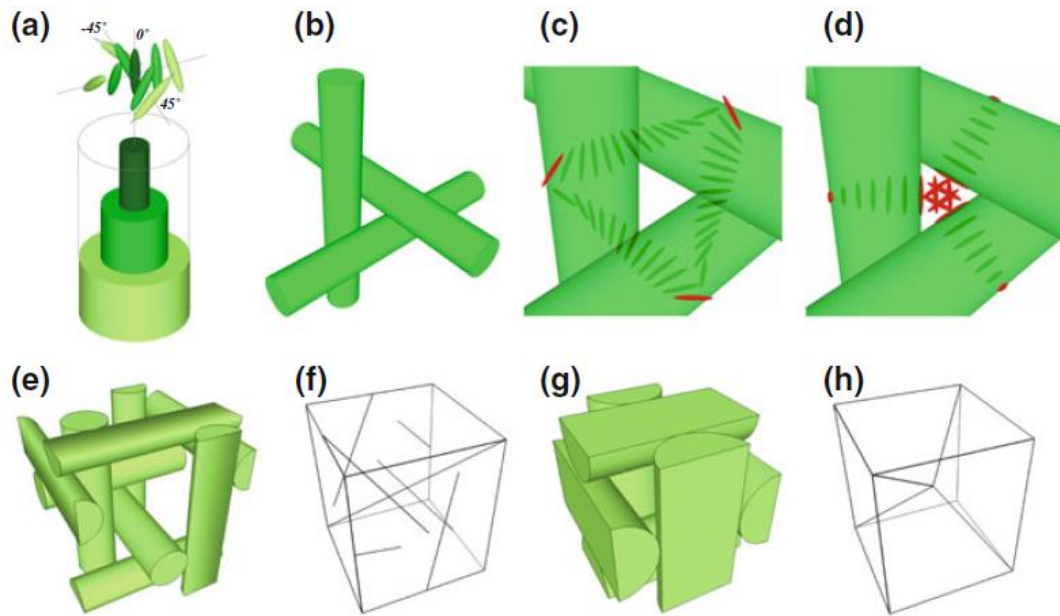


Fig. 2-3. Conceptual depiction: (a) director distribution in a DTC; (b) three-dimensional stacking of DTCs and the corresponding director distribution of the (c) continuous and (d) discontinuous portions; arrangements of DTCs and disclinations in (e), (f) BPI and (g), (h) BP II, obtained from reference [25].

2.2 Theory of BPLC

In the 1980s, two major theories were developed to gain a further understanding of the cubic structure of blue-phases: the Landau-de Gennes free energy theory [34-36] and the Oseen-Frank defect theory [2, 37]. The Landau-de Gennes theory is frequently used in both theoretical and numerical calculation and predicts phase transition using order parameter tensor, i.e. Q tensor.

An alternative model of blue-phases can be explained by the Oseen-Frank defect theory in a more simple way. The model was based on the Frank elastic model, and it was first discussed by Meiboom [37]. Take BPI as an example. The body-centered-cubic structure with $S = -\frac{1}{2}$ disclinations is observed. In this chiral system, the free energy elastic density can be expressed as:

$$F_1 = \frac{1}{2} \left\{ k_{11} (\vec{\nabla} \cdot \vec{n})^2 + k_{22} (\vec{n} \cdot \vec{\nabla} \times \vec{n} + q_0)^2 + k_{33} [\vec{n} \times (\vec{\nabla} \times \vec{n})]^2 \right\} \quad (2-1)$$

$$F_2 = (k_{22} + k_{24}) \vec{\nabla} \cdot [(\vec{n} \cdot \vec{\nabla}) \vec{n} - (\vec{\nabla} \cdot \vec{n}) \vec{n}] \quad (2-2)$$

The first equation was described in Eq. 1-7 as splay, twist, and bend distortion in the bulk, respectively. The second equation is the saddle-splay deformation as well as the surface term in BPLC, since the surface integral is non-zero in blue-phases. Lastly, k_{ij} is the elastic coefficient. For simplicity, we take $K_{11}=K_{22}=K_{33}=K$ and $K_{24}=0$. Therefore, the integration over the surface of a cylinder surrounding the disclination is

$$F_2 = -\pi (k_{22} + k_{24}) = -\pi K, \quad (2-3)$$

where F_2 is the energy per unit length along the disclination. Now, the total energy of BPLC with $S = -\frac{1}{2}$ disclinations can be written as:

$$F = F_{core} + F_{interface} + F_1 + F_2 \quad (2-4)$$

The first term represents the excess free energy of the disclination core. When the temperature T is close to the clearing point T_c , this term can be shown as:

$$F_{core} = a(T_c - T)\pi R^2, \quad (2-5)$$

where R is the radius of the core around 10 nm and the coefficient a is about 8 kJ/m³K in typical value. The second term describes a surface energy at the interface between cholesteric liquid crystals and disclination core given by:

$$F_{interface} = 2\sigma\pi R, \quad (2-6)$$

where σ represents a surface tension of the disclination. By approximating $S = -\frac{1}{2}$ and simplifying only one elastic constant K , the total free energy is

$$F = \frac{\pi}{4} K \ln(R_{max}/R) - \frac{\pi}{2} K + a(T_c - T)\pi R^2 + 2\sigma\pi R \quad (2-7)$$

Here, the minimum free energy (i.e., $F=0$) can be found. R_{max} indicates the maximum core radius of disclination, which is around 100nm.

Chapter 3

Ultrafast Optical Responses of BPLCs

3.1 Introduction of Optical Limiting

The extensive integration of high-power laser devices into modern technology has led to the development of efficiently manipulating the amplitude, phase, or the direction of the optical beam. The use of lasers in our daily life, such as optical communication, medical surgery, manufacturing, or military uses, shows how important they are. However, the illumination intensity is very crucial to determining how dangerous the system is. For military uses, night vision goggles can help a soldier to reveal a surrounding target with very low ambient light, but with exposure to high-intensity illumination, the optical system can be easily be disabled and cause damage to the soldier's eyes. Additionally, we have seen reports from news media in which people have been arrested for shooting lasers into the sky. This act is of great concern because the laser beam could accidentally pass over a military aircraft and blind its pilot [38].

Generally, optical limiting can be categorized into two method group: mechanical and passive. Mechanical methods, like shutter, which controls an iris for blocking transmitted light, are usually combined with multiple optical components, such photosensors and processors. The complex system results in slower speeds than passive methods due to the communication of each components, and it is only capable of limiting milliseconds laser pulses or continuous wave (CW) lasers. For modern laser technology,

the pulse width can be as short as a picosecond, where the mechanical methods can no longer be effective.

By contrast, much research interest is directed toward nonlinear optical materials as a passive limiter. Nonlinear optical properties, such as fast response, large nonlinearity, and broader spectral response are important to accomplish simple and efficient limiting. Typically, the process of sensing and processing and the actuation function in the passive limiting materials are synchronized. The speed of attenuation is determined by their physical properties, and the devices can potentially respond fast enough to block the ultra-short laser pulse.

Ideally, a passive optical limiter should have linear transmission under low intensity illumination but block the incident light when it exceeds the threshold. Therefore, the device can protect sensitive optical sensors or even human eyes. Those materials all exhibit at least one nonlinear optical property, such as nonlinear absorption, nonlinear refraction, nonlinear scattering, or optically induced phase transition. Those mechanisms can be associated with two-photon absorption, excited-state absorption, Kerr effect, or optically induced heating effect and lead to different results, such as defocusing, scattering, or photorefractive, as shown in Fig. 3-1 [39].

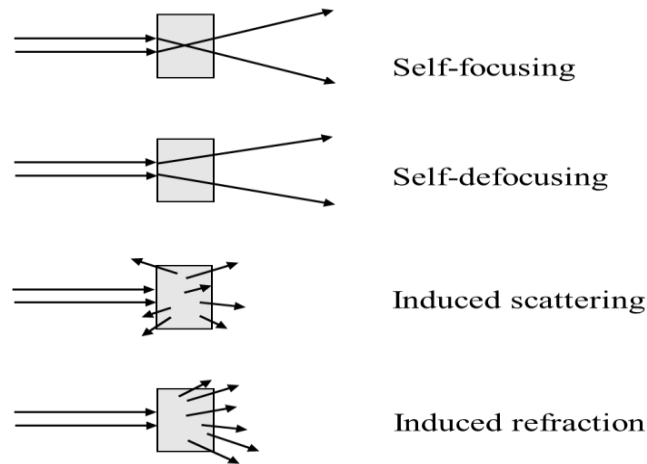


Fig. 3-1. Schematic illustrations of optical limiting.

One of the most important applications of an optical limiter, which will be focused on, is the protection of sensors and human eyes. These delicate optical sensors, which includes eyes, have certain light exposure thresholds that can cause irreversible damage. According to the American National Standard for Safe Use of Lasers (ANSI), the maximum permissible exposure chart (MPE), shown below, indicates that a human eye could be permanently damaged under $0.5 \mu\text{J}/\text{cm}^2$ light exposure within the visible spectral range [40]. Therefore, applying appropriate optical limiting devices to the system is important to allow the sensors or eyes to continue to remain fully functional under harsh conditions.

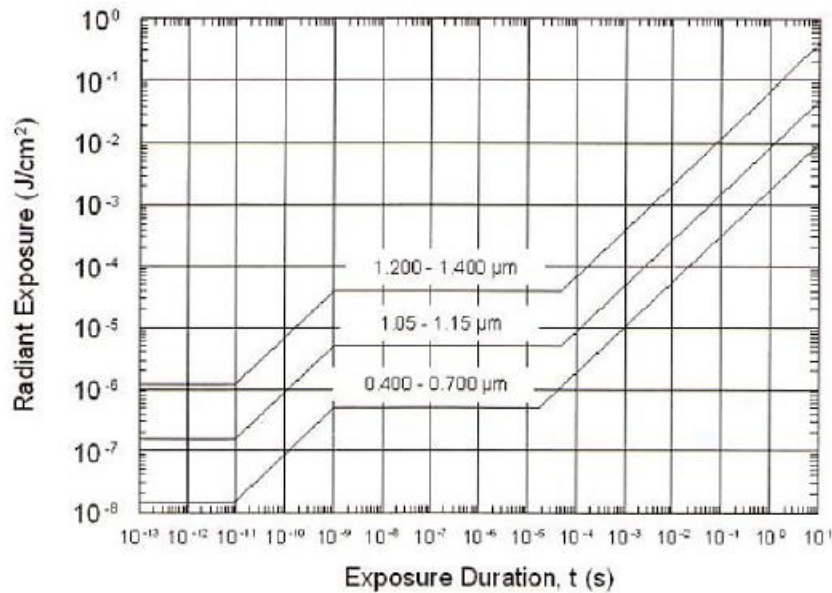


Fig. 3-2. MPE fluence for direct ocular exposure for a range of exposure durations, as per various wavelength ranges from reference [40].

For passive optical limiting, the processes can be achieved by various nonlinear optical mechanism, such as self-defocusing, refraction, and scattering. Varieties of materials are studied for those nonlinear processes for optical limiting. The goal is to develop materials with high optical nonlinearity and fast response within the visible spectrum range and be able to incorporate them into optical systems or compact devices. The most-widely studied materials are fullerenes, semiconductors, photorefractive materials, organic materials, and liquid crystals. The materials generally exhibit multiple nonlinear optical properties, but one of them usually dominates the others. Organic materials, like Indanthrone, are well-known for their reversible saturable absorption (RSA),

which is caused by photoinduced excited-state absorption [41]. These kind of materials exhibit very fast responses because of the electronic interaction. However, the responding spectrum is confined to a certain wavelength range, and the extinction ratio is low, which makes them not suitable for eye-protection devices. The optical properties in fullerenes includes nonlinear absorption and nonlinear scattering over the visible spectrum. This is ideal for broadband optical limiting, but the response time can only fit in a short pulse laser because of the triplet life time [42].

Among these materials, liquid crystals are undoubtedly the best candidate of optical limiting devices. With the largest optical nonlinearity and the ease of modulation, liquid crystals stand out for all-optical switch applications. Many researches have indicated liquid crystals, especially nematic phase, are sensitive to a very wide spectrum range and give rise to large birefringence while still transparent. This is attributed to accumulated molecular response along with temperature and density effect, which will be discussed in the next section.

3.2 Introduction of Maxwell Stress in Liquid Crystal

Owing to the free charges in the liquid crystals caused by impurities [43], the Maxwell stress theory can be applied to the optical response of transparent liquid crystals under an electric field or intense laser pulse. As a result, the ability to flow and the strong coupling effect between flow and crystalline axis rotation or lattice distortion can be explained. This approach was first used by Eichler and Macdonald in 1991 [44] to interpret the flow-reorientation effect generated by an optical polarization grating structure in the transparent nematic liquid crystal, as shown in Fig. 3-3.

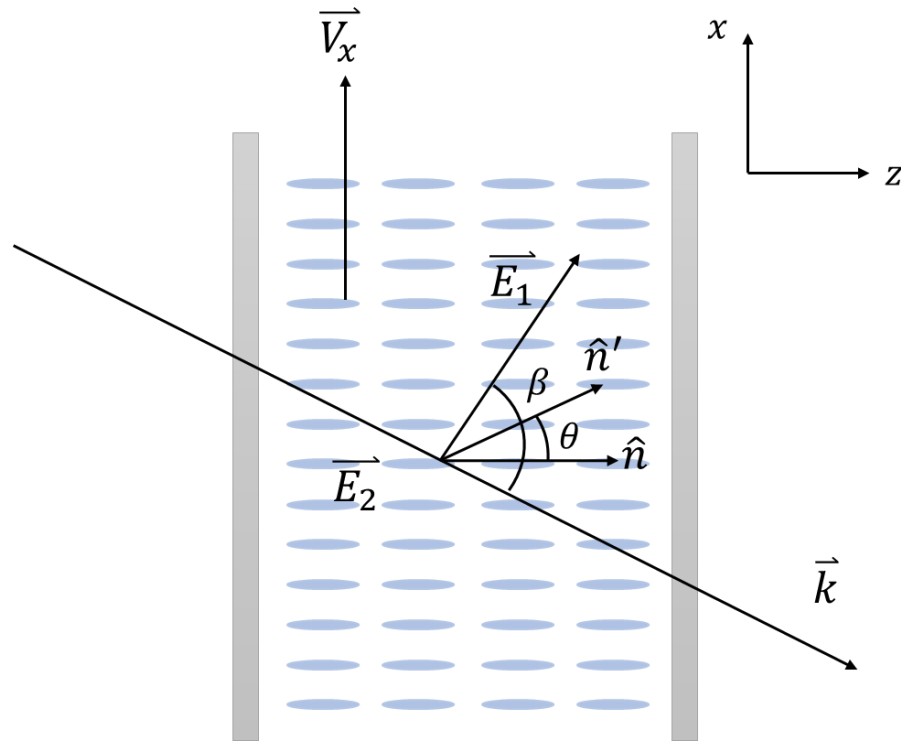


Fig. 3-3. Side view of coherent optical wave mixing of two crossed-polarized lasers in a homeotropically aligned NLC cell.

In the figure, the alignment of liquid crystal is in z-direction, and two coherent laser beams derived from splitting the laser with the same optical intensity and cross-polarization intersect at a small angle of β on the NLC. The optical field vector of the polarization grating can be described as $[E(t)e^{ik_t y + ik_l z}, E(t)e^{-ik_t y + ik_l z}, 0]$, where k_t is the wave vector in the transverse direction and k_l is in longitudinal direction.

The flow-reorientation effect can be derived from extending Jackson's theory of Maxwell stress in a vacuum [45] to the case of liquid crystal by assuming the materials are linear, non-dispersive, and lossless. Therefore, the force density acting on the liquid crystals can be described as

$$f = \rho E + J \times B \quad (3-1)$$

According to Gauss's law and Ampere's circuital law,

$$\rho = \nabla \cdot D, J = \nabla \times H - \frac{\partial D}{\partial t}, \quad (3-2)$$

and

$$\frac{\partial}{\partial t} (D \times B) = \frac{\partial D}{\partial t} \times B + D \times \frac{\partial B}{\partial t}, \quad (3-3)$$

we have

$$f = (\nabla \cdot D)E - B \times \nabla \times H + D \times \frac{\partial B}{\partial t} - \frac{\partial}{\partial t} (D \times B) \quad (3-4)$$

By substituting $\frac{\partial B}{\partial t}$ and $\nabla \cdot B = 0$, we have

$$f = (\nabla \cdot D)E - D \times \nabla \times E + (\nabla \cdot B)H - B \times \nabla \times H - \frac{\partial}{\partial t} (D \times B) \quad (3-5)$$

The time-average of electrical momentum term $g = D \times B$ is zero, and, as mentioned in the first chapter, the dielectric anisotropy is much larger than the diamagnetic anisotropy. Therefore, only the electric part of Eq. 3-5 is left. The expression of Maxwell stress becomes

$$f_E = (\nabla \cdot D)E - D \times \nabla \times E \quad (3-6)$$

Additionally, owing to the slow response of liquid crystal, the result of Maxwell stress would be the time-averaged value

$$\langle f_{E,x} \rangle = \frac{1}{2} \text{Re} [(\nabla \cdot D)E^* - D \times \nabla \times E^*] \quad (3-7)$$

Under the optical polarization grating field, as given above, the Maxwell stress can have the following components:

$$\langle f_{E,x} \rangle = -\frac{1}{2} \varepsilon_0 \varepsilon_{\perp} q_t E_0^2 \sin(q_t y) \quad (\langle f_{E,y} \rangle = 0, \langle f_{E,z} \rangle = 0), \quad (3-8)$$

where $q_t = 2 k_t$ is the difference between two optical field vectors with the grating constant $\Lambda = 2\pi/q_t$. The general form of flow-orientation effect is [44]

$$\rho_0 \frac{\partial v_x}{\partial t} - \eta \Delta V_x = F_x \quad (3-9)$$

$$\gamma_1 \frac{\partial \theta}{\partial t} - K \nabla^2 \theta + \frac{1}{2} (\gamma_1 + \gamma_2 \cos 2\theta) \frac{\partial V_x}{\partial t} = 0 \quad (3-10)$$

Here, V_x is the flow velocity in the x-direction, K is the elastic constant, θ is the angle of director axis reorientation, and γ_1, γ_2 , and η are the viscosity coefficient. In Eq. 3-9, F_x is a non-vanishing component, which provides the flow along the x-direction. By substituting 3-8 into 3-9, we obtain the following flow-reorientation equations:

$$\rho_0 \frac{\partial V_x}{\partial t} - \eta \frac{\partial^2 V_x}{\partial y^2} = -\frac{1}{2} \varepsilon_0 \varepsilon_{\perp} q_t |E(t)E^*(t)| \sin(q_t y) \quad (3-11)$$

$$\gamma_1 \frac{\partial \varphi}{\partial t} - K \frac{\partial^2 \varphi}{\partial y^2} + \frac{1}{2} (\gamma_1 + \gamma_2 \cos 2\varphi) \frac{\partial V_x}{\partial t} = 0 \quad (3-12)$$

For calculation, we assume φ would be relatively small and neglectable. By combining 3-11 and 3-12, the flow-reorientation of liquid crystal can be solved.

3.2.1 Estimate of Optical Nonlinearity – Flat-Top Square Pulse

To estimate the nonlinear index coefficient of the transparent liquid crystal sample under an intense laser pulse, we consider the case where both of the input optical fields are represented by a flat top-hat function:

$$|E(t)E^*(t)| = \begin{cases} E_0^2 & (0 \leq t \leq \tau_p) \\ 0 & (t < 0, t > \tau_p) \end{cases} \quad (3-13)$$

Because $\langle f_E \rangle$ contains the sinusoidal function in space, the reorientation angle φ and the velocity are in the form of

$$\varphi = \varphi_m \cos(q_t y) \quad (3-14)$$

$$v = v_x \sin(q_t y) \quad (3-15)$$

By substituting the condition into Eq. 3-12, we can thus have

$$\gamma_1 \frac{\partial \varphi_m}{\partial t} \cos(q_t y) + K q_t^2 \varphi_m \cos(q_t y) + \frac{1}{2} (\gamma_1 + \gamma_2) q_t v_m \cos(q_t y) = 0 \quad (3-16)$$

The maximum value of v_m can be obtained as

$$v_m = -\frac{2}{(\gamma_1 + \gamma_2) q_t} \left[\gamma_1 \frac{\partial \varphi_m}{\partial t} + K q_t^2 \varphi_m \right] \quad (3-17)$$

Substituting 3-17 into 3-11, we get

$$A \frac{\partial^2 \varphi_m}{\partial t^2} + B \frac{\partial \varphi_m}{\partial t} + C \varphi_m = -\frac{1}{2} \varepsilon_0 \varepsilon_{\perp} E_0^2, \quad (3-18)$$

where

$$A = \frac{2\rho_0\gamma_1}{(\gamma_1+\gamma_2)q_t^2} ; B = \frac{2(\rho_0K+\eta\gamma_1)}{(\gamma_1+\gamma_2)} ; C = \frac{2\eta Kq_t^2}{(\gamma_1+\gamma_2)} \quad (3-19)$$

The analytical solution to Eq. 3-18 during the optical pulse ($0 \leq t \leq \tau_p$) is, therefore, able to be solved:

$$\varphi(t) = -\frac{\varepsilon_0\varepsilon_\perp E_0^2(\gamma_1+\gamma_2)}{4\eta Kq_t^2} \left[1 - \frac{\tau_d e^{-t/\tau_d} - \tau_r e^{-t/\tau_r}}{\tau_d - \tau_r} \right] \quad (3-20)$$

$$\tau_d = \frac{\gamma_1}{Kq_t^2} ; \tau_r = \frac{\rho_0}{\eta q_t^2} \quad (3-21)$$

Apply the following parameters: $\rho_0 = 10^3 \text{ kg/m}^3$, $\gamma_1 = 0.001 \text{ kg/ms}$, $\eta = 0.02 \text{ kg/ms}$, $K = 10^{-12} \text{ kg}\cdot\text{m/s}^2$, the grating period is $\Lambda = 2\pi/q_t = 20 \text{ }\mu\text{m}$, and the relaxation time τ_d and rise time τ_r are 0.1 s and 1 μs , respectively. Because $\tau_d \gg \tau_r$, the rise time can be neglected in 3-20, and the orientation angle can be simplified to:

$$\begin{aligned} \varphi(t) &= -\frac{\varepsilon_0\varepsilon_\perp E_0^2(\gamma_1+\gamma_2)}{4\eta Kq_t^2} \left[1 - \frac{\tau_d e^{-\frac{t}{\tau_d}} - \tau_r e^{-\frac{t}{\tau_r}}}{\tau_d - \tau_r} \right] \\ &= \frac{\varepsilon_0\varepsilon_\perp E_0^2(\gamma_1+\gamma_2)}{4\eta Kq_t^2} \frac{\tau_r}{\tau_d - \tau_r} \left(1 - e^{-\frac{t}{\tau_r}} \right) \\ &\cong \frac{\varepsilon_0\varepsilon_\perp E_0^2(\gamma_1+\gamma_2)}{4\eta Kq_t^2} \frac{\tau_r}{\tau_d} \left(1 - e^{-\frac{t}{\tau_r}} \right) \end{aligned} \quad (3-22)$$

Moreover, in the case of flat top laser pulse approximation where the pulse duration is much shorter than the rise time ($\tau_p \ll \tau_r$), the solution converts to:

$$\varphi(t) = -\frac{\varepsilon_0 \varepsilon_{\perp} E_0^2 (\gamma_1 + \gamma_2)}{4\eta K q_t^2} \frac{\tau_p}{\tau_d} = \varphi_m^{ss} \frac{\tau_p}{\tau_d} \quad (3-23)$$

To further understand the value of nonlinear coefficient n_2 , the reorientation angle dependence of the refractive index is now applied:

$$\Delta n = n_e(\varphi + \Delta\varphi) - n_e(\varphi) \frac{n_{\perp} n_{\parallel}}{(n_{\perp}^2 \cos^2 \Delta\varphi + n_{\parallel}^2 \sin^2 \Delta\varphi)^2} \quad (3-24)$$

For small angle approximation,

$$\Delta n = \frac{n_e(\beta) \varepsilon_a}{(n_{\perp}^2 \cos^2 \beta + n_{\parallel}^2 \sin^2 \beta)^2} \frac{\sin 2\beta}{2} \cdot \varphi_m \quad (3-25)$$

$$n_2^{ss} = \frac{\Delta n}{I} = \frac{\varepsilon_a \varepsilon_{\perp}}{n_e(\beta)} \cdot \frac{(\gamma_1 + \gamma_2) \sin 2\beta}{4c\eta K q_t^2} \quad (3-26)$$

Here, n_2^{ss} is the corresponding nonlinear coefficient at steady state associated with the optical-field-induced flow-orientation effect in liquid crystals. Use the following values for each parameter: $\gamma_1 = 0.001$ kg/ms, $\gamma_2 = -1.09 \gamma_1$, $\eta = 0.02$ kg/ms, $K = 10^{-12}$ kg·m/s², the grating period is $\Lambda = 2\pi/q_t = 20$ μm , and assuming $\sin 2\beta = 1$, the nonlinear coefficient is calculated to be 4×10^{-5} cm²/W.

3.2.2 Estimate of Optical Nonlinearity – Gaussian Pulse

For the real case in the application, the input laser is a Gaussian-shaped pulse in time. Therefore, the optical field should contain the delta function in order to solve the real case. The optical field is expressed as

$$|E(t)E^*(t)| = E_0^2 \delta(t), \quad (3-27)$$

and the reorientation angle thus becomes

$$\varphi(t) = \frac{\varepsilon_0 \varepsilon_{\perp} E_0^2 \gamma_1 \rho_0}{2q_t^2 (\eta \gamma_1 - \rho_0 K)} \left[e^{-\frac{t}{\tau_r}} - e^{-\frac{t}{\tau_d}} \right] \quad (3-28)$$

In addition, the laser pulse converts to the form of $E_p = E_0 e^{-(t-t_0/\tau_p)} e^{i\omega t}$, where τ_p is the pulse duration that gives out the temporal variation and the change in nonlinear coefficient. Using the same parameters as mentioned above and the beam size of input laser ω_0 as $100\mu\text{m}$ with pulse duration τ_p of 350 ns, the simulation result is demonstrated [10]. In Fig. 3-4, the laser-induced reorientation angle and change of refractive index as a function of input laser intensity are shown.

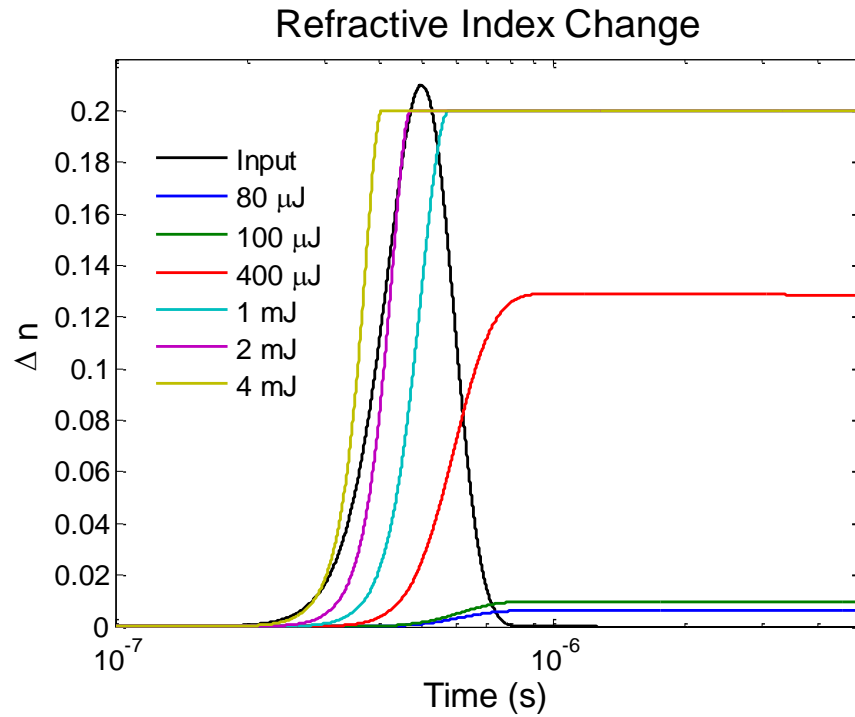


Fig. 3-4. Refractive index changes under different input intensity from reference [10].

In a typical case, the relaxation time of director axis reorientation in liquid crystal is much longer than the pulse duration, and, therefore, the reorientation angle and the induced refractive index change remain in peak value after the pulse is passed.

3.2.3 All-Optical Switching with Twist Nematic Alignment Cell

Twisted Nematic Liquid Crystal (TNLC) is undoubtedly the most widely used E-O modulator in the industry, i.e. Liquid Crystal Display (LCD). “Twisted” means the liquid crystal is experiencing a 90° twist between two substrates, as shown in Fig. 3-6. In a typical

electro-optic switching device, such as using TNLC for a display pixel, the input light from the back panel is polarized by the input polarizer and is parallel to the director axis on the input plane. When the optical intensity is weak, the polarization of light follows the rotation of the director axis, passes the analyzer with the polarization parallel to each other, and is then fully transmitted.

Electro-optic switching is demonstrated by applying an AC field across the NLC cell windows that realign the director axis to eventually be perpendicular to the cell windows, and the contrast ratio is determined by the field induced orientation [17].

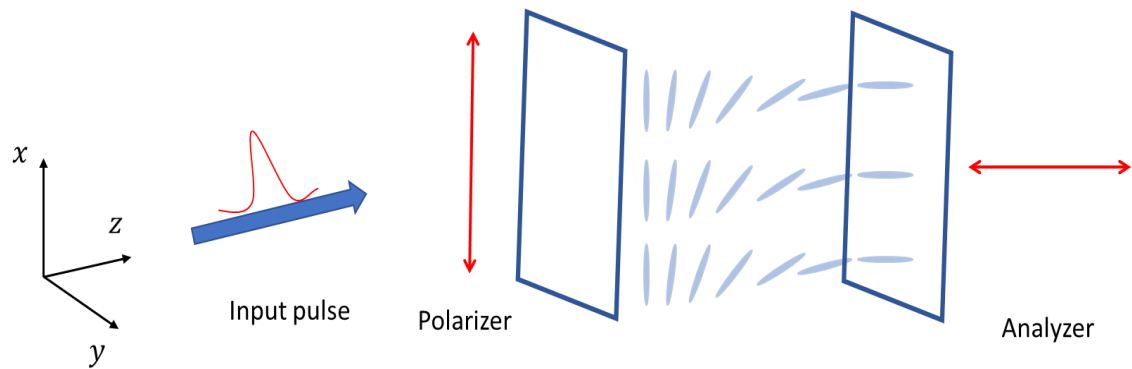


Fig. 3-5. Optical switching cell: Twist Nematic Liquid Crystal sandwiched between crossed polarizers.

In the all-optical switching devices using liquid crystal, the incident light is high enough to change the director axis orientation and create different kinds of optical limiting mechanism, as mentioned in Chapter 3-1 [46-48]. In this case, the Maxwell stress from the focused laser beam creates the radial flow reorientation in the liquid crystal and randomizes the director axis of the sample. The effective birefringence Δn of TNLC is reduced from

the maximum value to 0, and the order parameter is also decreased. This means the polarization rotation through the NLC cell is diminished, and the laser pulse exiting the cell with the polarization orthogonal to the output polarizer will be attenuated.

In the simulation, in which the results are shown below, an approximation is adopted in which the birefringence generated by the intense laser pulse induces the flow-orientation in the TNLC. It is the form of $\Delta n = n_2 I(t)$, where n_2 is the nonlinear coefficient calculated in Chapter 3-2. The Jones Matrix method is considered to calculate the time-dependent attenuation in transmission with the birefringence change using the same set of parameters in the previous section [48].

Figures 3-7 and 3-8 show the transmission and power dependence for different input laser energies. Note that under 200 μJ , there is no appreciable attenuation on the input pulse, thus the output pulse shape is similar to the incident field. At an energy higher than 200 μJ , the transmission begins to drop significantly, and the switching time is faster.

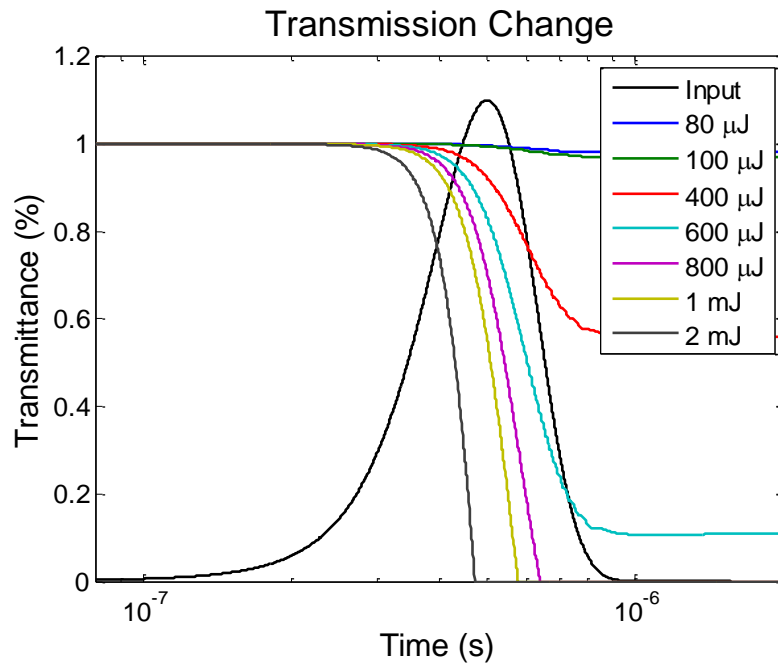


Fig. 3-6. Dynamical simulation of transmission under different input energies from reference [10].

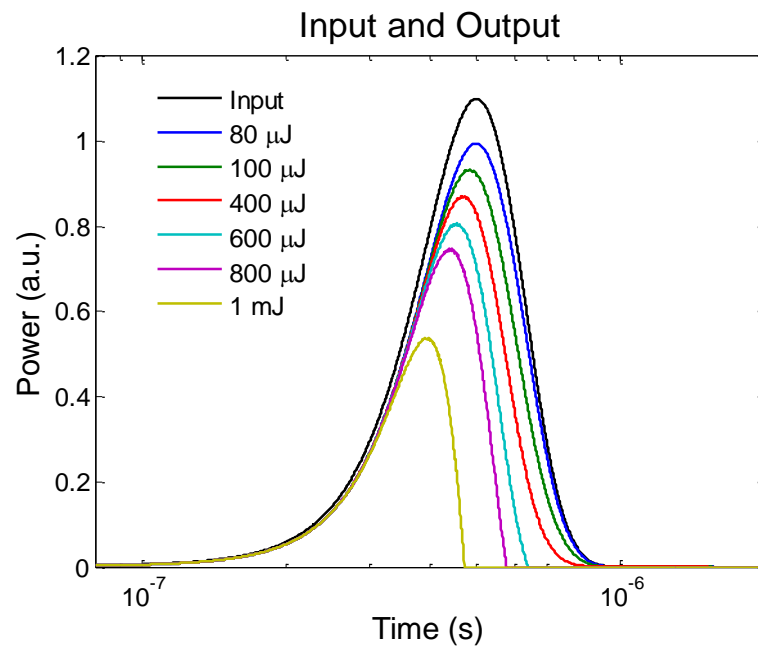


Fig. 3-7. Input versus output pulse shapes under different input pulse energies from reference [10].

To further prove the simulation, a 750nm laser is used to characterize the TNLC sample in order to demonstrate the switching-off effect. and the result is shown in Fig. 3-9. The sample is made by 5CB because of its linear absorption as well as its weak multi-photo absorption at 750nm. Two different input energies were used in the experiment, and the result showed the transmission of input laser pulse from the cell is largely attenuated by the TNLC sample.

This result shows a good agreement with the simulation, as the attenuation of transmission is proportional to the input intensity, and the threshold for triggering the effect is around 10 μ J (equivalent to a laser peak intensity value $I = 1.5 \times 10^5 \text{ W/cm}^2$ with a laser spot diameter $2\omega_0 \sim 140 \mu\text{m}$).

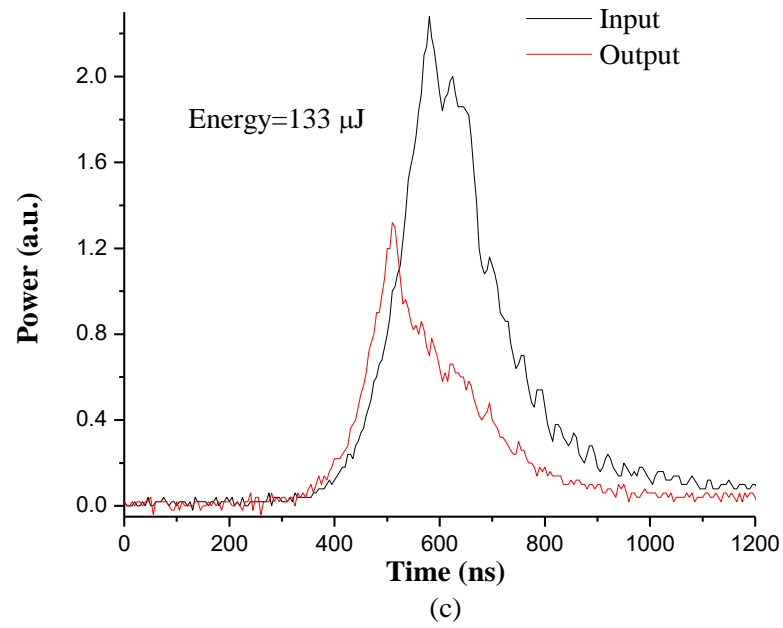
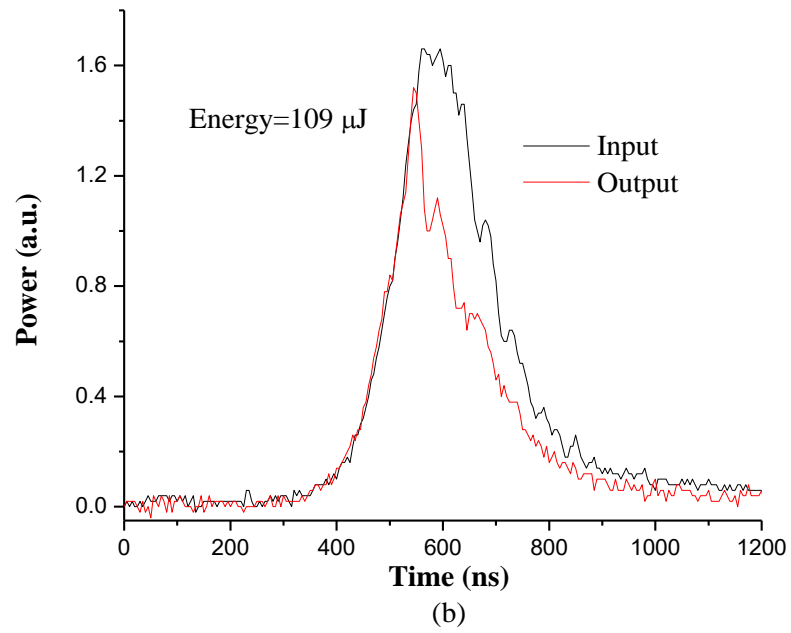


Fig. 3-8. (a) Oscilloscope traces of the input and output laser pulses for input laser energy = $109 \mu\text{J}$; (b) input laser energy = $133 \mu\text{J}$ from reference [10].

3.3 Laser-Induced Lattice Distortion in BPLC Cell

Research studies using blue-phase liquid crystal as a material for electro-or all-optical applications has been increasing recently [49-53]. Owing to its fast response time and unique optical properties, such as being polarization-free and easy to fabricate, BPLC becomes an alternative to NLC, and light-induced Maxwell stress promises a new approach for all-optical switching in BPLC.

To continue the discussion in the previous section, we found that the optical field of an intense laser pulse can generate Maxwell stress and cause a defocusing effect in transparent BPLC [10]. In fact, there are studies that show that, in general, the focused laser pulse requires an intensity around several MW/cm² to trigger the observable optical switching effect in BPLC [50, 54].

In the case of combining the Gaussian laser pulse with the intensity form of

$$I(r) \sim |E(t)E^*(t)|e^{-2r^2/\omega^2} \quad (3-29)$$

and the Maxwell stress from Eq. 3-6 we obtain

$$\langle f_E \rangle = \varepsilon_0 \varepsilon_{\perp} |E(t)E^*(t)|e^{-2(x^2+y^2)/\omega^2} \left[-\frac{x}{\omega^2}, \frac{y}{\omega^2}, 0 \right] \quad (3-30)$$

The equation of the field-induced flow process now can be described as:

$$\rho \frac{\partial v_x}{\partial t} - \eta \nabla^2 v_x = f_{E,x} = -\varepsilon_0 \varepsilon_{\perp} |E(t)E^*(t)| e^{-2 \frac{x^2+y^2}{\omega^2}} \cdot \frac{x}{\omega^2} \quad (3-31)$$

$$\rho \frac{\partial v_y}{\partial t} - \eta \nabla^2 v_y = f_{E,y} = \varepsilon_0 \varepsilon_{\perp} |E(t)E^*(t)| e^{-2 \frac{x^2+y^2}{\omega^2}} \cdot \frac{y}{\omega^2} \quad (3-32)$$

The simulation of the magnitude of Maxwell stress is depicted in Fig. 3-10, which has a volcano-shaped radian dependence profile with a peak value at $\sim 0.7 \omega$ and a minimum value occurring in the center. Here, the comprehensive calculation of dynamical response in the BPLC, including 3-D structural deformation and flow dynamics under the flow-induced distortion and director axis reorientation and relatively complicate and is out of the scope. However, it is obvious that the intense optical field from focusing the Gaussian laser pulse creates the corresponding radial flow, lattice distortion, and the refractive index modulation. Therefore, the input laser pulse experiences the self-focusing/defocusing effect created by the volcano-shaped phase modulation inside the BPLC.

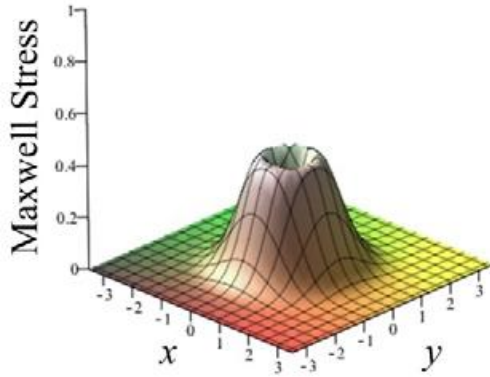


Fig. 3-9. Plot of the radial dependence of the magnitude of the Maxwell stress associated with a Gaussian laser beam from reference [10].

The optical switching by the phase modulation using nanosecond laser pulses was demonstrated in the previous studies [54]. The laser-induced negative refractive index change cause in the BPLC cell and the modulation result in defocusing laser beam and on-axis intensity attenuation. To further complete the studies, we repeated the experiment with the picosecond pulsed-laser system in order to understand the faster response in BPLC. The sample here consists of two nematics with positive dielectric anisotropy, E48 and 5CB, and adding chiral smetic S-811 with the ratio of: E48 (32%); 5CB (32%); S-811(36%). The laser pulse train with the following parameters (kilohertz repetition rate; individual pulse duration: 2 ps; pulse energy: 200 μ J; λ = 800 nm; focused laser diameter: \sim 200 μ m) was focused on the transparent sample. A mechanical shutter with 10 ms duration was applied to the system in order to control the amount of the pulses and act as a pump beam while a 532 nm CW laser with very low intensity was used for probing the refractive index profile through the process. Additionally, a photodiode and an oscilloscope are used to receive the information from the probe beam. The depiction of the experimental setup is shown in Fig. 3-10(a).

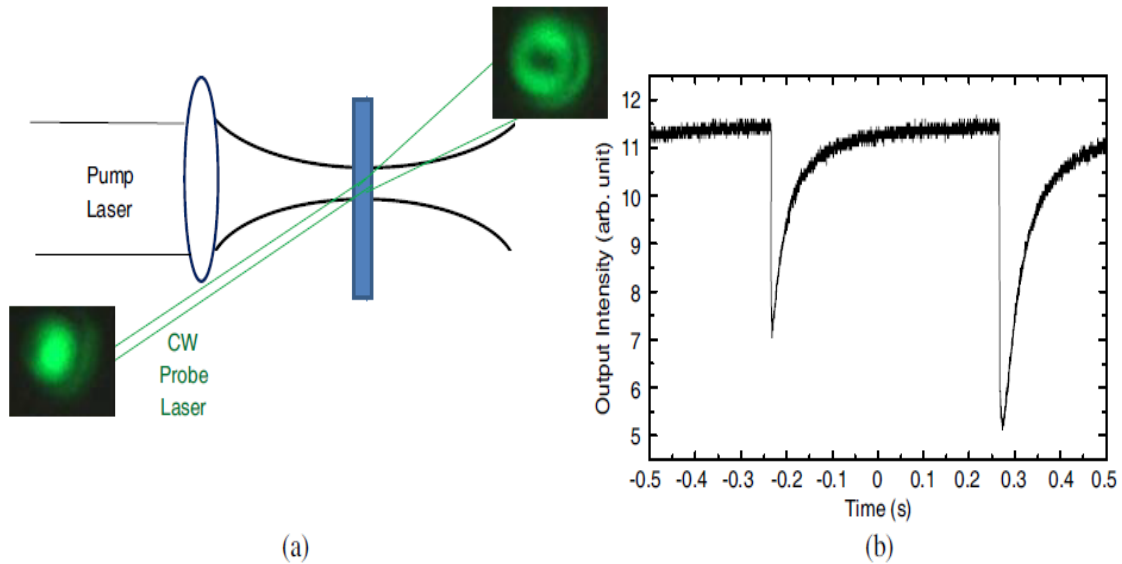


Fig. 3-10(a) Schematic depiction of the experiment set up for probing pulse laser induced flow and self-defocusing effect. (b) Measurement of the probe beam transmission showing the instant drop following by slowly recovering in [42].

As expected, the on-axis power of the laser beam was largely attenuated by the BPLC sample, and the intensity exhibited a very fast drop (almost vanishing), as shown in the photo of the transmitted probe beam in Fig. 3-10(a). In Fig. 3-10(b), the dynamical response of the probe beam is shown, and we can see that, after the fast drop from the intense input pulse, the recovery time is in the scale of seconds after the pump beam. This is due to the relaxation time of the director axis, and recovering from the flow is typically longer.

Here, we emphasize that Maxwell stress was not the only mechanism which occurred in the experiment. With this high intensity of optical field, all kinds of nonlinear

optical effect can happen in the material, such as multi-photon absorption, thermal effect, or electrostriction effect. However, the result is in a good agreement that in such high-power laser pulse, BPLC is a promising material for optical switching effect and a good candidate of optical limiting device. An example is using a BPLC-infiltrated fiber array faceplate as a sensor protection device, which can be placed in the optical image system [50].

Chapter 4

Photorefractive Effect of BPLCs

Photorefractive effects (PR) producing two-beam coupling and side diffraction was observed in fullerene-C₆₀-doped blue-phase liquid crystal using the DC-field assisting nonlinear effect [55]. By adding the space charge E_{photo} to the material and combining with the DC field E_{dc} , the mechanism here was lattice distortion in the BPLC generated by the DC field and optical field, as shown in the previous studies using dye-doped nematic liquid crystal. A first-order diffraction efficiency of $\sim 2 \times 10^{-3}$ and beam coupling gain of over 2% were observed in a 55 μm thick sample with input laser beam power of 5 mW at an applied DC voltage of 160V. The effective nonlinear index coefficient n^2 of BPLC-C₆₀ was measured to be on the order of $10^{-2} \text{ cm}^2/\text{W}$, slightly lower than their NLC counterparts. Owing to the isotropy of BPLC optical properties, these effects can be observed with more relaxed requirements on the laser polarizations, directions of incidence, and sample orientations. The details of the result will be discussed in this chapter.

4.1 Introduction of Photorefractive Effect

Great interest in the photorefractive effect in dye-doped or fullerene-doped liquid crystal has arisen since 1994 with the discovery of orientational photorefractivity in liquid crystalline material found by Khoo et al [56, 57]. Studies show the photo-charge-induced molecules, once photo-excited, can generate the intermolecular torque in the liquid crystal [55-61]. The applied voltage required to trigger the photorefractive effect is in the order of a few volts instead of kilovolts, as in the typical photorefractive crystals, and the optical nonlinearities are much larger than the traditional device, i.e. $\Delta n \sim 0.2$ with the input intensity $I \sim 100 \text{ mW/cm}^2$. Therefore, research groups are interested in developing the photorefractive material using liquid crystals.

The first photorefractive effect was observed in 1966 [62], and consists of the spatial modulation of the refractive index by the photo-induced redistribution of space charge carriers in the inorganic ferroelectric crystals, and it was then used for image storage and signal processing applications [63]. Nowadays, many electro-optic materials are found to have photorefractive effects, and each material has its own unique properties, such as fast response time, sensitivity, storage persistence, and storage density.

The schematic illustration of the basic photorefractive process is shown in Fig. 4-1. In the typical PR effect measurement system, two coherent laser beams are overlapped onto the photorefractive materials in order to create an interference pattern and the photo-induced spatial charges in illuminated regions, as shown in Fig. 4-1(a). The charges are produced by the optical field and then diffuse through the crystal toward the intensity

minimum regions or draft in response to the external DC field to create nonuniform space charge distribution, i.e. Figure 4-1 (b) and, therefore, result in sinusoidal refractive index modulation. Here, the magnitude of refractive index modulation is determined by the magnitude of the space charge field. This kind of refractive index modulation can occur in many different mechanisms, such as photoisomerization, thermorefraction, or generation of excited states. However, the photorefractive effect includes a unique property of nonlocal and asymmetric modulation arising from the physical motion of the diffusing charges in the materials. As shown in the Fig. 4-1(d), the diffusion of the space charges give rise to the phase difference between the optical interference pattern and the modulation of the refractive index. This mechanism is important to trigger the energy transferring between two incident light fields, which is known as the two-beam coupling effect.

In Kerr-like media, such as nematic liquid crystals, the refractive index modulation Δn created by mixing two coherent laser beams is proportional to the square modulus of the total fields acting on the liquid crystal director axis, i.e. $\Delta n \sim (E_{dc} + E_{photo})^2$, where E_{dc} is the applied DC field and E_{photo} is the total space charge [43, 56, 57, 64]. Although NLC doped with various photo-charge producing agents have been shown to have very high wave mixing efficiencies, their birefringent optical properties generally impose strict requirements on the laser polarization, incident angles, and sample orientations. Furthermore, the effects tend to be plagued by flows and instabilities by a very small increase in the applied voltage above the threshold value for wave mixing effect to manifest. At higher applied DC voltages, the NLC cells are degraded and no longer responsive.

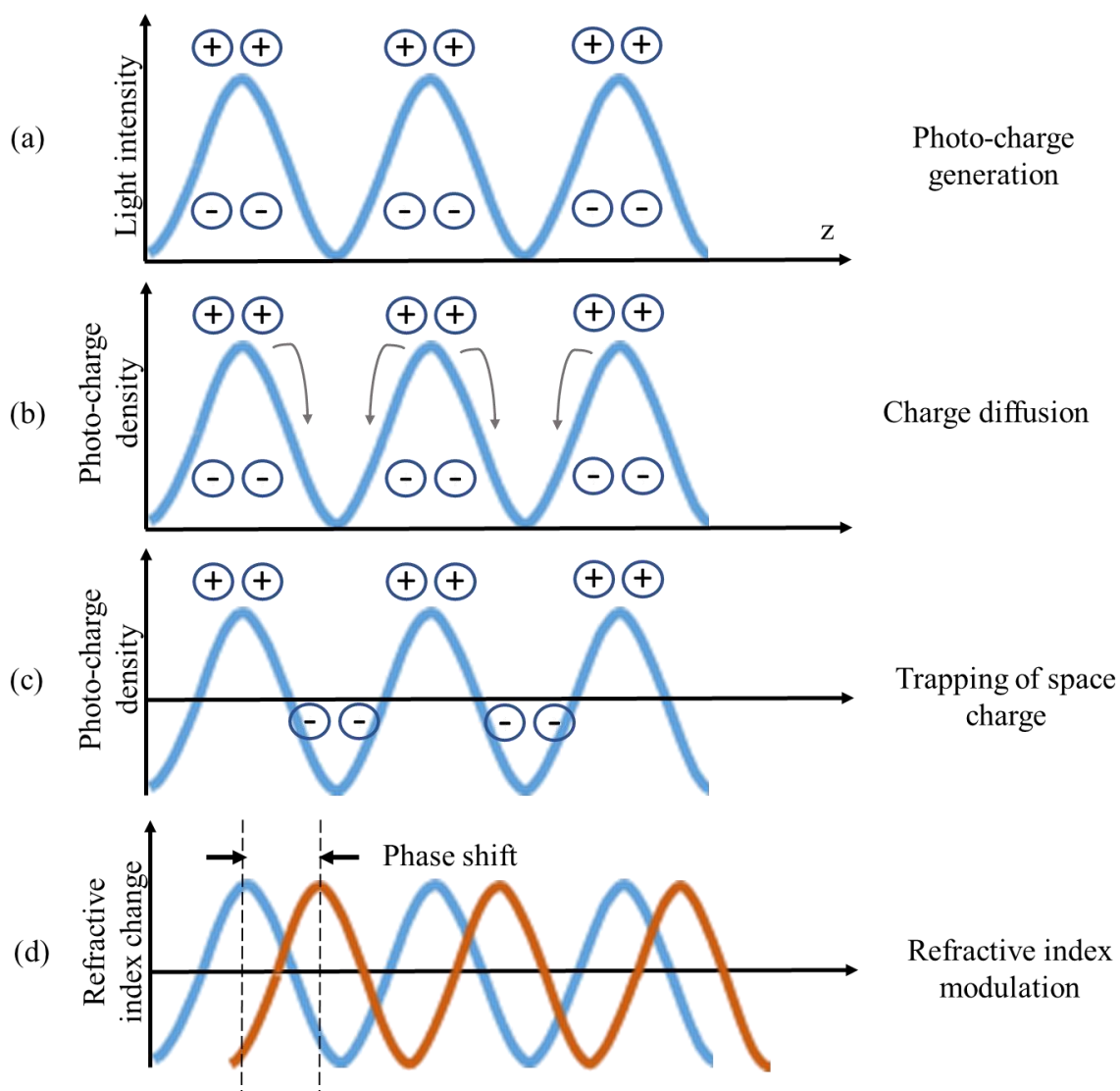


Fig. 4-1. Schematic depiction of the photorefractive effect along the spatial distribution.

In this chapter, we report to our knowledge the first observation of photorefractivity in another ordered phase of liquid crystals, namely, blue-phase liquid crystals (BPLC) lightly doped with a photo-charge producing agent such as Fullerene C_{60} . They are,

therefore, optically isotropic, i.e. respond to omnidirectional light of any polarization state. Our studies have shown that, in general, undoped BPLC exhibits vanishingly small nonlinearity under moderate laser intensity, but their dye-doped counterparts do possess optical nonlinearities of magnitude comparable to nematics. In our two-wave mixing studies, we have observed a beam coupling gain of about 2% with input laser beam power of 5mW at an applied DC voltage of 160V. The effective nonlinear index coefficient n^2 for this sample is measured to be on the order of $10^{-2} \text{ cm}^2/\text{W}$. The underlying mechanisms are attributed to DC + Photorefractive space charge field-induced director axis reorientation and BPLC crystalline distortion.

4.2 Sample Preparation and Experimental Setup

The BPLC mixture consisted of two different nematics with positive anisotropy, E48 and 5CB, and a chiral smectic was added in the ratio of E48 (32%), 5CB (32%), and S-811 (36%). The mixture of BPLC was designed to have the blue-phase in room temperature and a fairly large temperature range of 8 °C for the ease of measurement. The BPLC exhibits the phase transition temperature as the following: isotropic ($>31^\circ\text{C}$), BPII ($31^\circ\text{C}\sim 28^\circ\text{C}$), BPI ($28^\circ\text{C}\sim 23^\circ\text{C}$), and cholesteric focal conic phase N^* ($<23^\circ\text{C}$). The dopant we chose was fullerene- C_{60} because of its high production of photo-induced charges in a wide absorption wavelength. Owing to its low solubility, the concentration of C_{60} in the

BPLC was only around 0.1% which made the sample exhibit a very high transmission of over 90%. Moreover, this light-doped BPLC still yielded very high optical nonlinearities comparable to those highly absorptive dye-doped systems [65, 66].

Figure 4-2 depicts the experimental setup of the optical wave-mixing geometry. A CW laser with the wavelength at 532 nm was applied to the system, the laser beam was split into two coherent and co-polarized beams by the beam splitter and overlapped onto the BPLC sample with the very small crossing angle ($\alpha = 0.4^\circ$). A tilt angle of the sample was applied to create the unidirectional phase shift. This tilt angle β was 45° with regard to the normal direction. We have observed similar results for laser polarization in the y-direction or in the x-z plane (orthogonal to y-direction). It is important to note here that although BPLC bulk is isotropic in nature, an applied DC field that results in some realignment of the director axis or lattice distortion will break such ‘symmetry’ and create a field-direction dependent index modulation as shown in the following section.

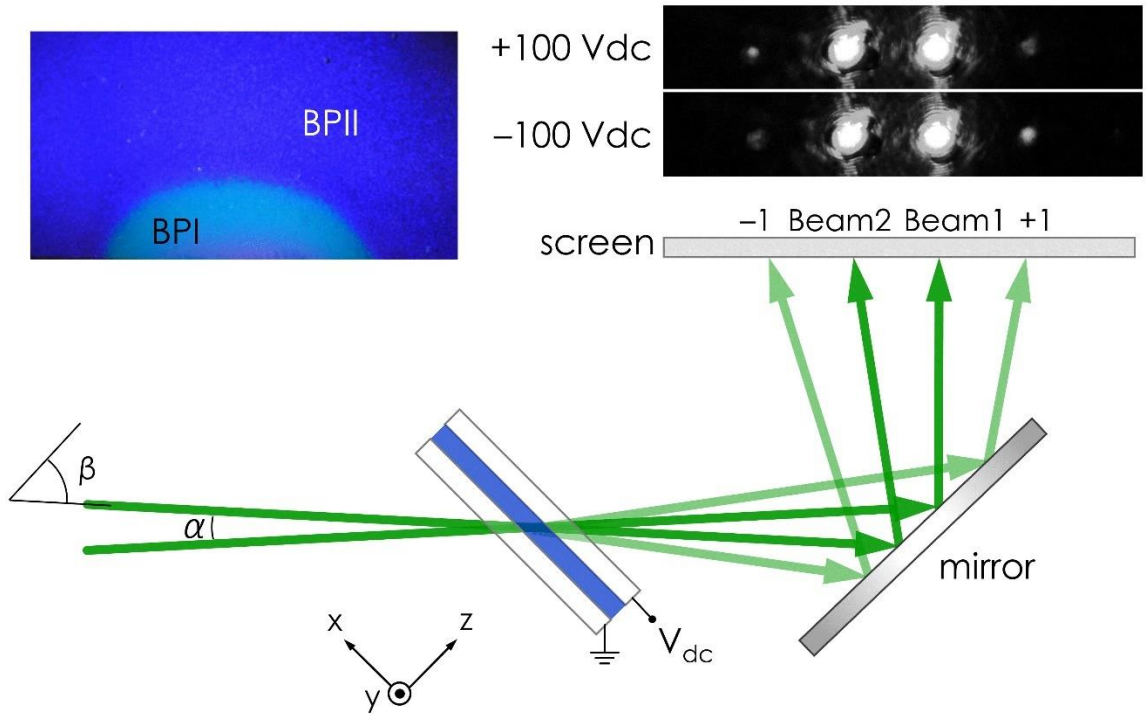


Fig. 4-2. Schematic depiction of the wave mixing experiment set up. Upper left photo shows the reflection colors corresponding to BPII and BPI phase of sample maintained at different temperatures. Upper right photo depicts the transmitted pump beams and diffractions under positive and negative DC biases.

4.3 Experimental Result of Photorefractive Effect in BPLC

In Fig. 4-2, the upper right photo shows the first-order diffraction on the both sides of the pump beam when the applied DC voltage was higher than 5V and the diffraction power was asymmetric depending on the direction of the applied DC field. For negative voltage, i.e. the voltage in the forward direction of the laser beam propagation, we observed much stronger +1 diffraction signal on the Beam 1 side than the Beam -1 side, as shown in

the photo. Notice that the asymmetry of the diffraction beam power distribution is reversible when the applied DC field is reversed. A detail study of this side diffraction as a function of applied voltage was revealed and will be discussed in the next section. In Fig. 4-3, the diffraction power with the relation to applied DC voltage is shown. The observed results clearly show two different responses, (i) and (ii), depending on the voltage level and how the voltage is applied.

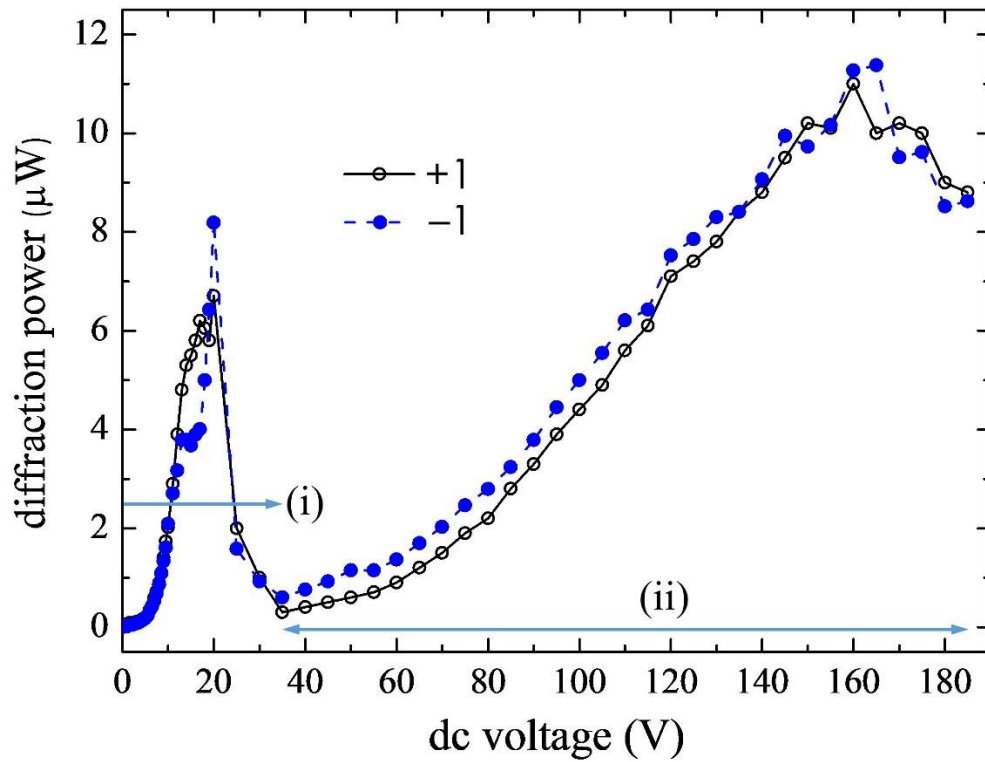


Fig. 4-3. Observed first-order (+1 and - 1) diffractions as a function of increasing applied DC voltages from a 55- μm thick sample. [Error bars of $<0.5\%$ in each data point not shown]. In the voltage region between 40 - 140 V_{dc} , the asymmetry in the +1 and -1 diffraction powers is particularly evident from reference [55].

In Section (i), well-formed and clear diffractions were observed above an applied DC voltage of 3V, and they developed to a peak value of a few microwatts (around 6 ~ 8 μW) at an applied voltage of 20V before significantly dropping to an almost vanishing value (0.1 μW) at 30V, when the diffraction signal was diffused. Repeated experiments in this applied voltage region (0V–30V) showed that the maximum diffraction value observed at ~ 20V was relatively unstable and fleeting in nature, i.e. the signal would rise to the peak value of a few μW , and then rapidly drop to a much lower value of 1 μW . Also, once diminished by the higher applied voltage, the diffractions signals could not be recovered if the applied voltage was lowered. The major mechanism here was owing to field-induced director axis reorientation of those loosely bound, randomly oriented molecules situated in the defect lines, similar to those occurring in methyl-red dye doped BPLC [66]. We have also observed evidence of flows at the applied voltage region around 20 V_{dc} ; dynamic scatterings from the sample and motion of trace ‘foreign’ particles in the intensity grating maxima were visible by eye. This was accompanied by an overall drop in transmission, as shown in the later section on the transmission spectra as a function of the applied voltage in the 8 ~ 20 V_{dc} regions.

For the case in which applied voltage is above 30V as in (ii), the sample started to assume a clearer appearance when dynamic scattering was observed to cease; visible side-diffraction reappeared and gradually increased in magnitude as the applied voltage was increased, rising to a peak value of 12 μW at around 160V before beginning to decrease for higher applied voltages. Unlike the transient signals observed in (i), the side-diffractions signal for this voltage range were stable and completely reversible; they

retained a well-formed beam appearance and were reproduced as the applied voltage was ramped up and down between 30V–180V. The major effect attributed to the results was the BPLC lattice distortion by the combined DC (E_{dc}) and photorefractive space-charge (E_{photo}) fields, similar to the DC + optical field induced effects reported in previous studies of dye-doped system [65, 66]. In other words, there were two major components of the induced refractive index change: a local index change Δn_1 due to the DC + optical field induced effects as in dyed-BPLC, and a non-local (phase shifted) index change $\Delta n_2 e^{-i\varphi}$ due to the DC + space-charge fields where $\varphi = \pi/2$ is the phase shift. The nonlocal (phase-shifted) index change gave rise to beam coupling and asymmetric side diffractions, as previously shown in Fig. 4-2 (insert photos), the side diffractions from equal pump beam powers were asymmetric with the +1-order diffraction clearly stronger (weaker) to the -1 order, depending on the direction of the applied DC field. The asymmetry in the +1 and -1 diffraction power was particularly evident in the applied voltage region between 40 – 120 V_{dc} and began to vanish above 140 V_{dc}, even as the diffractions continued to increase with increasing voltage up to ~160 V_{dc}. A complete quantitative analysis of the contributions from individual mechanism contributing to these multi-beam wave mixing process and the resulting power distributions arising from the complex interactions of the local and non-local responses to the applied and induced fields in BPLC is extremely complex and is clearly outside the scope of this chapter. However, from the observed asymmetry in the first order diffractions one could make a qualitatively assessment of the relative contribution of the photorefractive effect to the overall diffraction. This rough estimate based on the ratio of the asymmetry in the diffractions to the overall diffraction in Fig. 4-3 shows that it is clearly dependent on the applied DC field; the relative contribution from

photorefractivity was around 30 % at 40 V_{dc}, gradually decreased to about 15% at 80 V_{dc}, and, finally, the asymmetry vanished around 160 V_{dc}.

Owing to the tight bound structure of the crystalline lattice of BPLC, the responses did not show any sign of deterioration by these applied fields. We have repeated these experiments with a 35-μm thick sample and observed similar dependence with the applied voltages of equivalent electric field strengths. In the case of the 35-μm sample, an applied DC voltage of 210V totally extinguished the wave mixing effects when the sample was observed to be completely aligned along the field direction (became homeotropic) with transmission that approached nearly 100%.

To obtain a measure of the magnitude of the nonlinearity, we used the nonlinear diffraction data collected for the 55 μm thick sample, where the peak first order diffraction efficiency $\eta \sim 0.24$ % was produced by at an input laser intensity of $\sim 5.5 \times 10^{-2}$ W/cm² (beam power: 5mW; beam diameter: 3mm). Using the Raman-Nath diffraction formula

$$\eta = (\pi d \Delta n / \lambda)^2 \quad (4-1)$$

with d as the thickness, and λ as the wavelength, the grating index modulation was estimated to be $\Delta n \sim 1.51 \times 10^{-4}$. If we expressed Δn in terms of an effective refractive index coefficient n^2 , i.e. $\Delta n = n_2 I$, this provided $n_2 \sim 0.27 \times 10^{-2}$ cm²/W for BPLC-C₆₀, which was about two orders of magnitude smaller than the Methyl-red dye-doped sample [66], and was simply due to the low solubility of C₆₀ in BPLC. Nevertheless, such n_2 value (>

$10^{-2} \text{ cm}^2/\text{W}$) still put BPLC- C_{60} in the ‘giant optical nonlinearity’ category when compared to other NLC systems [67].

These dependencies on the applied voltage were also manifested in the two-beam coupling effect, i.e. unidirectional transfer of energy from one beam to the other, similar to photorefractive effects in NLC [43, 56, 64]. The field induced index modulation was $\pi/2$ phase shifted from the optical intensity grating. By reversing the applied voltage, and, therefore, the sign of E_{dc} , the phase shift became $-\pi/2$, which resulted in energy transfer in the opposite direction. Figure 4-4 demonstrated the ratio of the transmitted pump beams as the applied voltage was increased from 30V to 160V in both directions—+V and -V direction. For negative biased voltage ($-V$), pump Beam 1 experienced growth at the expense of Beam 2. On the other hand, for positive bias (+V), Beam 2 experienced growth at the expense of Beam 1. We have repeated these experiments for the case where the sample is tilted in the opposite directions, i.e. changing the angle β to $-\beta$, and observed the inverse of these gain/loss beam coupling effects.

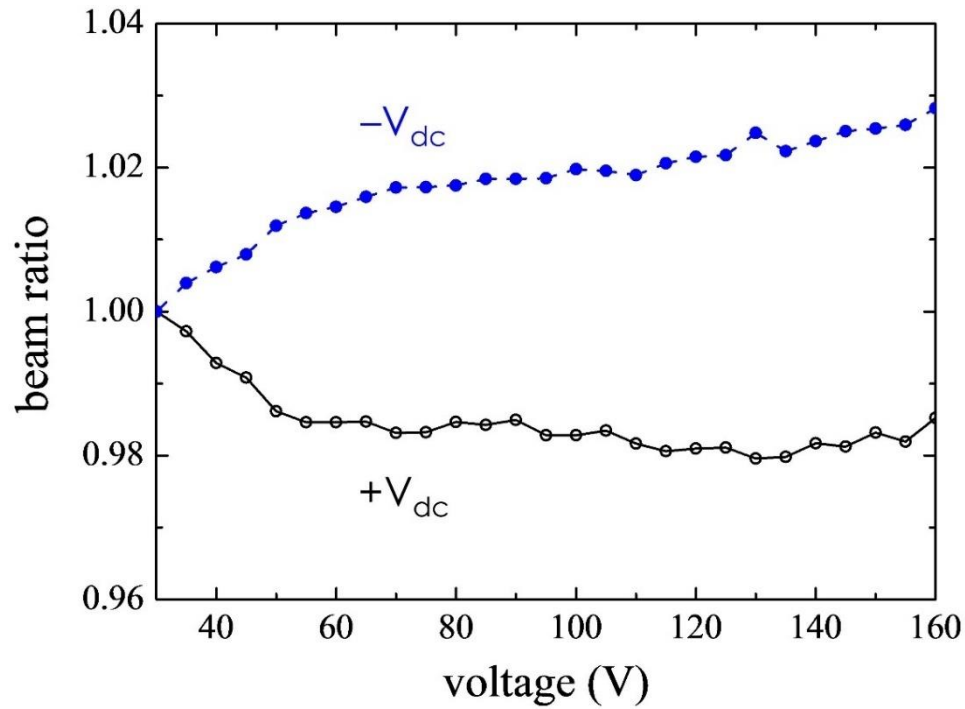


Fig. 4-4. Observed Pump Beam 1 to Beam 2 ratio as a function of applied DC voltage, showing the beam coupling effect [Error bars of <0.5% in each data point not shown] from reference [55].

The transmission spectra indicates the field-induced lattice distortion in BPLC causes a huge change in photonic bandgap, as shown in Fig. 4-5. In the 8–20V range for example, the transmission decreased substantially as the applied voltage was raised, reaching its lowest value at around 20V. The BPLC lattice, nevertheless, remained largely intact, as reflected in the minimal change to the shape/slope of the bandgap. On the other hand, for higher a voltage region (e.g. 60–160Vdc), very pronounced changes were produced by the fields-induced lattice distortion, which depicted a large increase in the transmission as the voltage was raised. In all cases, note that the impinging laser generally produced an overall appreciable increase in the transmission.

Moreover, we demonstrated some preliminary studies of the dynamics of these DC + optical fields-induced wave-mixing effects by monitoring the grating side-diffractions, whose magnitudes are more sensitively dependent on the applied voltage than the beam coupling effect. Using 0-150V square voltage pulses of 5–10ms duration at a repetition rate of 1 Hz, we had observed a diffraction signal rise time of ~ 1 ms and a relaxation time of ~ 2.5 ms for sample maintained in the BP_{II}. In the BP_I, the observed rise time was much longer (~ 10 ms), and the decay dynamics exhibited an initial fast decay time of ~ 2.5 ms followed by a slow ‘tail’ that lasted for several tens of ms. These response dynamics, which are slower in BP_I than in BP_{II}, are consistent with other studies of the electro-optical responses of BPLC [30-33].

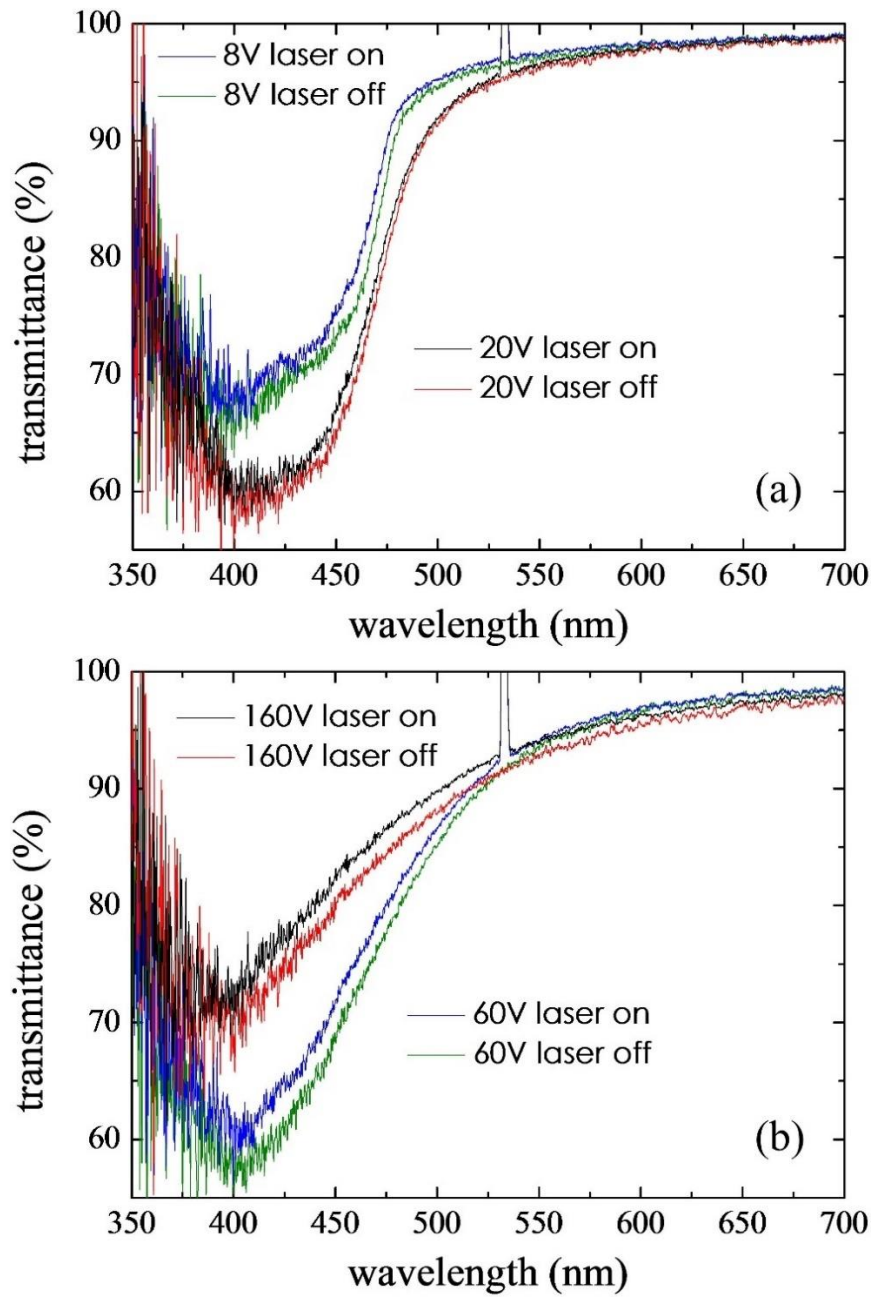


Fig. 4-5. Transmission spectra of a 55- μm thick BPLC cell maintained at BPII phase for two representative regions (a) and (b) of applied DC voltages with or without illumination by a 6 mW pump laser from reference [55].

Chapter 5

High-Efficiency Bragg Grating with BPLCs

In this chapter, the results of detail study of the mechanism and dynamics of photosensitive azo-dye doped blue-phase liquid crystals under holographic Bragg grating formation are demonstrated. The azo-dye blue-phase liquid crystals (A-BPLC) are capable of high diffraction efficiency holographic recording, and the memory can be prolonged from few seconds to several minutes by uniform illumination with the reference beam. The principal mechanism related to the refractive index modulation here is attributed to the lattice distortion caused by photo-induced trans-cis isomerism of the azo-dye dopant. Under the Bragg grating regime, an improvement of diffraction efficiency up to 70% and shorter recording time was observed.

We also showed the azo-dye photoisomerization triggered the lattice distortion along with the coupled flow-reorientation to the surrounding BPLC molecules. The effect can also further prove the mechanism that the frustration of free relaxation of lattice distortion by uniform illumination, thereby prolong the diffraction lifetime.

A-BPLCs present themselves as a highly promising photosensitive material for holographic storage and image processing applications. An experimental demonstration of holographic image reconstruction and phase conjugation image will be demonstrated in this chapter along with detail study of the dynamical response of the diffraction signal.

5.1 A Promising Holography Material: BPLC

Holographic research has received much attention for decades. Research groups are trying to develop materials that meet requirement for holographic recording and display application, such as high diffraction efficiency, faster writing/erasure/reading and refresh speed. The cost of the material and the complexity of fabrication are also important factors to meet the industrial production [11, 24, 68-73]. The holographic materials cover a wide range of crystals, photosensitive polymers, nano-particles, and soft-maters; the fabrication procedures vary from simple chemical synthesis or crystal growth to complicated pulsed laser modulation of nano-particles. However, state-of-art holographic materials developed so far are still saddled with the limitation with one kind or the other. For example, a photosensitive polymer, in general, exhibits a very fast response time but with short memory. The crystal, such as ion-doped lithium niobite, has a very high quality of optical storage application, but the recording time is relatively long, i.e. several minutes. Updatable materials generally require complex processing or an extremely high electrical field to erase or write [72].

Nonlinear optical materials, such as inorganic crystals, semiconductors, photorefractive polymers, and liquid crystals, are naturally suitable for direct holographic recording involving light-matter interaction by nonlinear optical responses. Among those materials, liquid crystals and organic polymers are most-widely studied due to the ease of fabrication and flexibility and their low optical power requirement associated with highly nonlinear optical responses [16, 74-77]. However, shortcomings still exist in those materials. Photorefractive polymer, for instance, requires a very high electric voltage for

recording and writing, while the birefringence of liquid crystals mandates the use of a polarized optical field. Moreover, the nonlocal forces from the boundary surface and unactivated region in the typical nematic liquid crystals become stronger when the cell thickness increases or the grating spacing decreases.

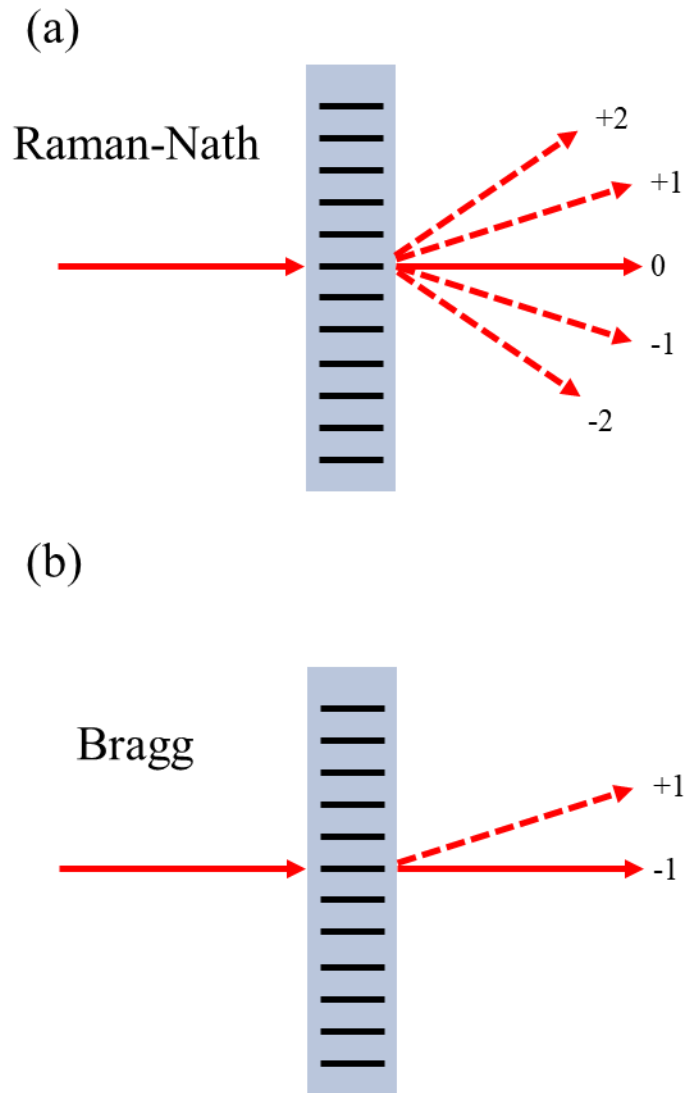


Fig. 5-1. (a) Schematic of the Raman-Nath grating with multi-order diffraction and (b) Bragg grating with single order diffraction.

Therefore, most research of holographic recording using nematic liquid crystals with visible light is conducted in the Raman-Nath region ($\Lambda^2 \gg \lambda d$), requiring a large grating constant up to 10 μm in the thin sample down to 100 μm . As shown in Fig. 5-1(a), this regime tends to have undesirable multi-order diffraction and low diffraction efficiency. Attempts to operate in Bragg grating regime ($\Lambda^2 \ll \lambda d$) using the same mechanism of optical field-induced director axis reorientation are plagued with inefficiency due to the strong anchoring force to boundary surface when the grating constant decrease.

Here, we demonstrate the possibility of circumventing these limitations of nematics and obtaining dramatic improvement on all major performance factors by using mm-thick photosensitive azo-dye-doped blue-phase liquid crystals (A-BPLCs) and operating in the hitherto unexplored Bragg regime ($\Lambda^2 \ll \lambda d$) [11].

Because of the tightly bound molecules in the doubly-twisted cholesteric spirals, nonlinear response associated with molecular reorientation by optical field is generally weak in comparison to nematic. However, by incorporating photosensitive dyes that reside mainly in the defect region, c.f. Fig. 5-2, a more efficient mechanism for index modulation associated with the action of light on the azo-dopant is manifested. In the experiment, we observed polarization-independent grating diffraction efficiency as high as 50% instead of ~1% and writing time of a few seconds instead of minutes. Furthermore, we have discovered a simple optical means of prolonging the lifetime of the written grating using the reference beam that is already in place; by keeping the reference beam on when the other beam (input signal) is turned off, the lifetime of the written grating/hologram can be prolonged from its natural relaxation time of a few seconds to several minutes.

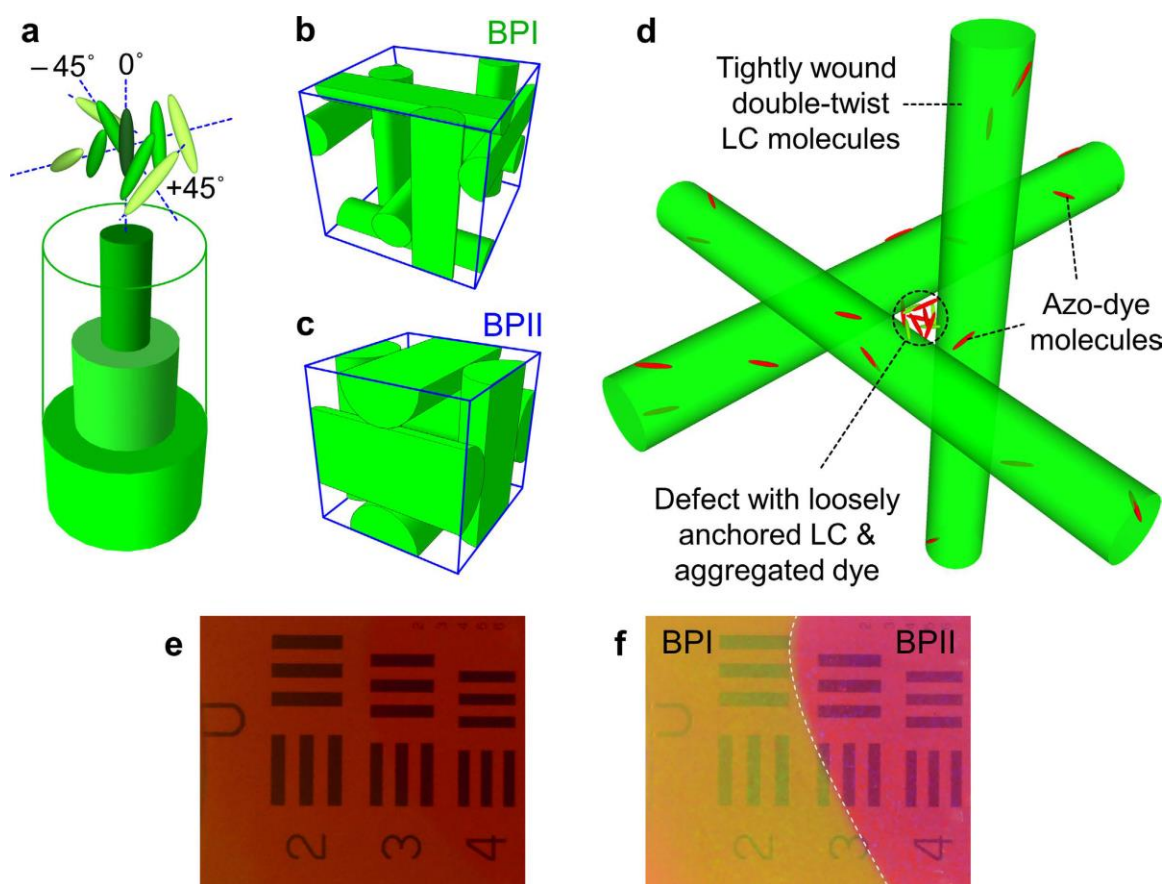


Fig. 5-2. Schematic depiction of the make-up of an azobenzene-doped blue-phase liquid crystal: (a) liquid crystal molecules in tightly wound double-twist cylinder; (b) BPI crystalline lattice; (c) BPII crystalline lattice; (d) enlarged view of the crystalline lattice and defect region where majority of dopant dye molecules aggregate, and participate actively in laser-induced lattice distortion (e) Photograph of the BPLC placed on top of the Air Force resolution chart; reddish coloration is due to the CPND-57 azo-dopant in BPLC; (f) Same as (e) but photo is taken with flash and exhibits more color display and contrast from the two blue-phase regions [regions of sample deliberately maintained at different temperatures] from reference [11].

Furthermore, a more efficient means of producing director axis reorientation or crystalline lattice deformation is by doping BPLC with azo-dyes. Upon photo-excitation, the azo-molecules transform from the oblong-shaped trans-state to the bent-shaped cis-

state, causing disorder and the surrounding BPLC molecules to undergo coupled flow-reorientation processes, resulting in substantial lattice distortion and resultant index modulation, characterized by an intensity-dependent index change coefficient n_2 , defined by index change per unit intensity, on the order of $10^{-3} \text{ cm}^2/\text{W}$. Similar to their nematic counterparts, giant optical nonlinearities of such magnitude enable various all-optical processes with low power lasers. In our studies, we used the azo-dye CPND-57 provided by BEAM Co., which is a eutectic mixture of CPND-5 and CPND-7 azo dyes, 1-(2-Chloro-4-N-nalkylpiperazinylphenyl)-2-(4-nitrophenyl) diazene, in the ratio 1:3. Because the slower trans–cis isomerism dynamics, CPND-57-doped BPLC reveals new features such as prolonged grating memory in the seconds–sub-seconds time regime not previously observed with methyl-red doped BPLC.

5.2 Wave-Mixing Setup and Sample Preparation

The mixture material for blue-phase liquid crystal consists of a chiral dopant S-811 (Merck) dissolved in two nematic hosts with positive dielectric anisotropy, E48 and 5CB, in the ratio E48 (32%), 5CB (32%), and S811 (36%). An important advantage of blue-phase liquid crystals (BPLC) over other ordered phases of liquid crystals, such as nematic and cholesteric, is that there is no need for surface alignment treatment when assembling the cell. Large area samples can be simply made by inserting isotropic liquid phase BPLC mixture between clean uncoated glass slides with plastic spacers (for thin samples) or filling flat glass cuvettes for the mm-thick BPLC cells used in our studies. As

a function of temperature, pristine BPLCs exhibit the following phases: transparent isotropic liquid phase for temperature above 31°C, bluish color BPII phase (at ~ 31°C–28°C), greenish-color BPI (at ~ 28°C–23°C), and cholesteric focal conic phase N* (below 23°C). In our studies, we have used two azo-dyes to enhance the nonlinear optical responses of BPLC: non-mesogenic Methyl-red dye [Aldrich] used previously and a mesogenic compound CPND-57 [Beam Engineering]. The latter is a eutectic mixture of CPND-5 and CPND-7 azo dyes, 1-(2-Chloro-4-N-nalkylpiperazinylphenyl)-2-(4-nitrophenyl) diazene, in the ratio 1:3. CPND-57 is known to be very stable under optical excitation compared to Methyl-red. These azo-dyes generally absorb in the blue-green spectral region. Dye-dopant concentration used in our study was guided by the desired sample transmission level at the writing beam wavelength (532 nm). For the 1-mm thick sample in the BPII phase, a small concentration of dyes (< 0.1%) resulted in an absorption loss of ~ 50% at 532-nm, but negligible small absorption loss at the probe wavelength (633 nm). Samples with this level of transmission were found to yield very large diffraction efficiency.

An electronically modulated CW laser at $\lambda=532$ nm was used in the wave-mixing experiment as the pump beam. The laser beam was expanded and collimated through the spatial filter (pin hole and objective lens). the beam was then split into two coherent beams with roughly equal power. Two coherent pump beams were then overlapped on the sample at large angle with different grating constant. The grating spacing here was at the range of 1~4 μm which is operating in Bragg grating regime. The Gaussian laser beam diameter was around 3 mm. A CW laser at 633nm was introduced as a probe beam traveling from the opposite side of the sample at the Bragg grating phase matching angle in order to have

high diffraction efficiency. The reason for choosing different wavelengths for the probe beam was to avoid the absorption of the azo-dye molecules. The sample was kept in the temperature-controlled cavity with the window for the incoming and exiting laser beams. The experimental setup is shown in the Fig. 5-3.

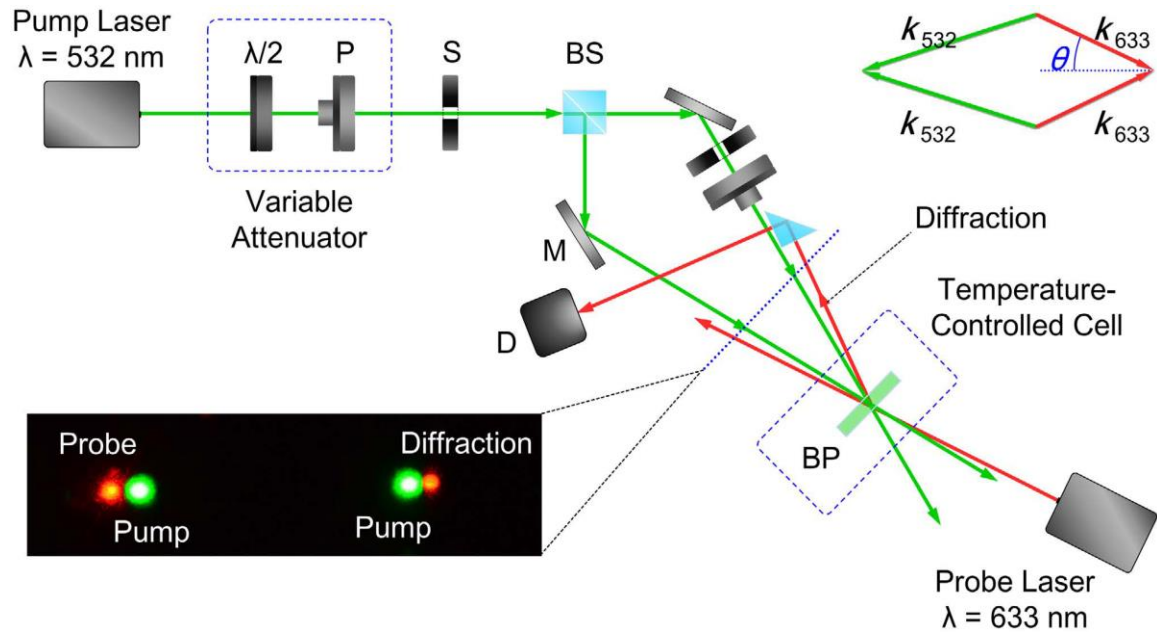


Fig. 5-3. Schematic depiction of the experimental setup for the wave-mixing and grating formation. The phase matching condition is shown at the upper-right diagram involving two pump beams ($\lambda=532\text{nm}$) and two probe beams ($\lambda=633\text{nm}$). P: polarizer; BP: a-BPLC sample; S: mechanical shutter; BS: beam splitter; $\lambda/2$: half-wave plate; D: photodetector; M: mirror]. The photo insert on lower left corner shows the writing beams, the probe beam and the diffracted beam on the screen from reference [11].

5.3 High-Efficiency Diffraction Result and Dynamical Response of A-BPLC

In the experiment, a strong diffraction signal began to build up with the writing beam power on the order of a few mW (beam diameter = 3mm), the corresponding intensity

was around several tens of mW/cm^2 . In Fig. 5-4 (a) (b), the typical dynamical diffraction response for simultaneous tuning on and off of two pump beams is shown with two different writing times. For the case of short writing time (~ 5 sec or less), the diffraction signal was observed to build up to maximum value till the end of the excitation pulse and decay monotonically to vanishing value after the pulse was off in around 5 seconds, as shown in Fig. 5-4 (a). If the writing time was longer than 8 seconds, the diffraction signal appeared to reach its maximum value in about the same time, but there was a small abrupt upturn in a relatively short time scale when the writing beams were turned off. As a result, the following decay dynamic was similar to the case of short writing time as depicted in Fig. 5-4 (b). The small abrupt rise in this case was most likely due to the fast decay of a small index component of opposite sign to the main contribution of lattice constant, and the component was because of the local disorder caused by the relaxation of bent-shaped cis-isomers to oblong-shaped trans-isomer, which is typically less than 1 second [74].

However, the dominant effect here comes from lattice distortion associated with slower rearrangement of the defect structure (disclination lines) associated with migration/flow of molecules away from the high intensity regions (grating maxima) to the low intensity regions (grating minima); such processes take longer (~ 5 sec) to develop. The peak diffraction value in this case was observed to be more than 50% for the writing beam powers of 6 mW [11]. The corresponding laser intensity was around $70\text{mW}/\text{cm}^2$ for the laser beam diameter of 3mm. Under the Bragg condition ($\Lambda^2 \ll \lambda d$, where $\Lambda \sim 3 \mu\text{m}$; thickness $d = 1 \text{ mm}$, $\lambda = 0.532 \mu\text{m}$), the probe diffraction sharply peaked at the wave-vector matching angle $\theta \sim 5.5^\circ$ with a half-width of $\sim 0.5^\circ$, as shown in Fig. 5-4 (c). The diffraction was also shown to be largely independent of the probe polarization relative to

the writing beams, manifesting the optical isotropy of the BPLC and the underlying mechanism that mediates the coherent optical wave mixing process.

In order to have further understanding of the mechanism, we repeated the experiment and other similar studies with various writing beam powers and durations, and we observed that the holographic grating structure took almost the same amount of time to decay as the build-up time which meant that the memory lasted as long as it took to record. In fact, when the writing duration (when both beams are on) was longer than 40 seconds, the index grating began to deteriorate due to several factors, including migration of the dyes from the illuminated region and/or heating of the sample beyond to the isotropic phase. For the holographic storage purpose, the long-lasting grating memory was required. In the previous studies using Methyl-red dye-doped BPLC, a small DC field ($\sim 5\text{V}/\mu\text{m}$) during the holographic recording resulted in an index grating that can last very long time (days if the sample is undisturbed) [66, 76]. However, to have an updatable holographic storage material, the complete erasure in the previous study had to be done by heating the sample over the isotropic phase and cooling back to blue phase, which normally takes several minutes. Although the required electric field was much lower than the photosensitive polymer case (up to 9 kV for complete erasure), the refresh time of a few minutes remained an undesirable drawback of such field DC field induced memory storage effects in these material systems. Therefore, an interesting discovery of a way to prolong the grating memory as well as erasure will be discussed in the next section.

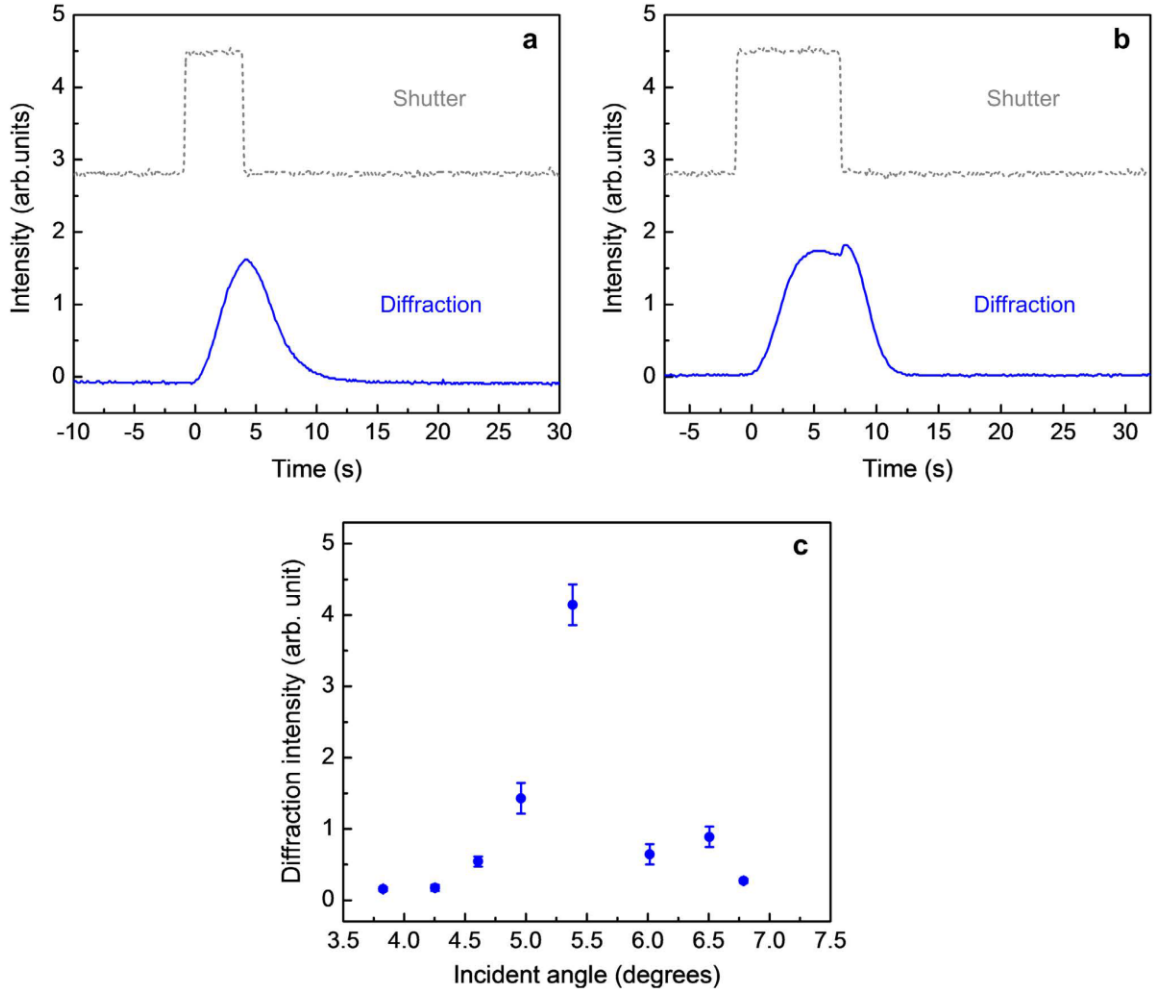


Fig. 5-4. Typical dynamical evolution of the probe diffraction with step-on/off writing beams for beam powers: 3.2 mW and 3.7 mW; samples maintained in BPII phase. Similar results are obtained in BPI phase. (a) 5 s writing time, showing a smooth build up and decay (b) 8 s writing time, showing an abrupt increase when the writing beams are turned off. (c) Plot of the diffraction signal showing the sharp spike centered at the phase-matched angle, obtained from reference [67].

The temporal dependence of the diffraction signal exhibited some interesting features for short writing time and the timing in which the writing beams turned off. Figure 5-5 shows the temporal response and the peak values of the diffraction signal with the

writing pulse duration of ~ 1 s for various temperatures in BPI and BP II. The maximum diffraction efficiency was observed at 28.8°C , which is the BPI-BP II transition [12].

In general, with beam power of ~ 0.5 mW, the diffraction signal built up to a maximum before beginning a monotonic decay to almost vanishing values in tens of seconds. The smaller was the grating constant Λ , and the shorter was the build-up time to maximum; for $\Lambda = 2$ μm , the build-up time was ~ 0.5 s compared to ~ 5 s for the case where $\Lambda = 4$ μm , cf. Fig. 5-6 (a,b). The build-up time was also observed to be dependent on the input laser power, i.e., the higher was the input (writing) beam power, the faster was the build-up to the maximum.

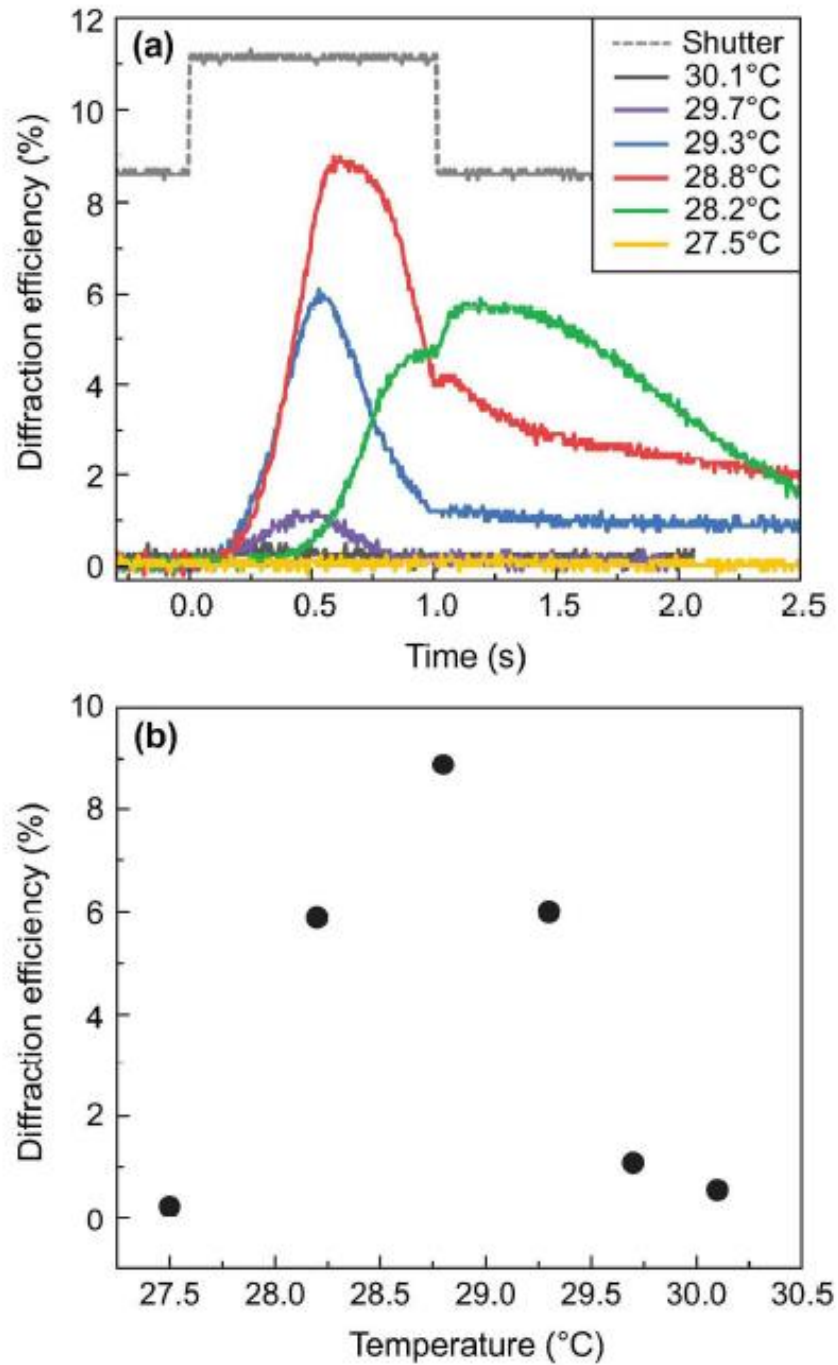


Fig. 5-5. (a) Time evolution of the diffraction signals in BPI and BPII phases for gated (1 second square pulse) writing beams at different temperatures. Sample thickness: 1 mm; grating spacing: 2 μm . Pump beam input powers at sample: ~ 7.5 mW. (b) Peak diffraction efficiency as a function of the sample temperature from reference [12].

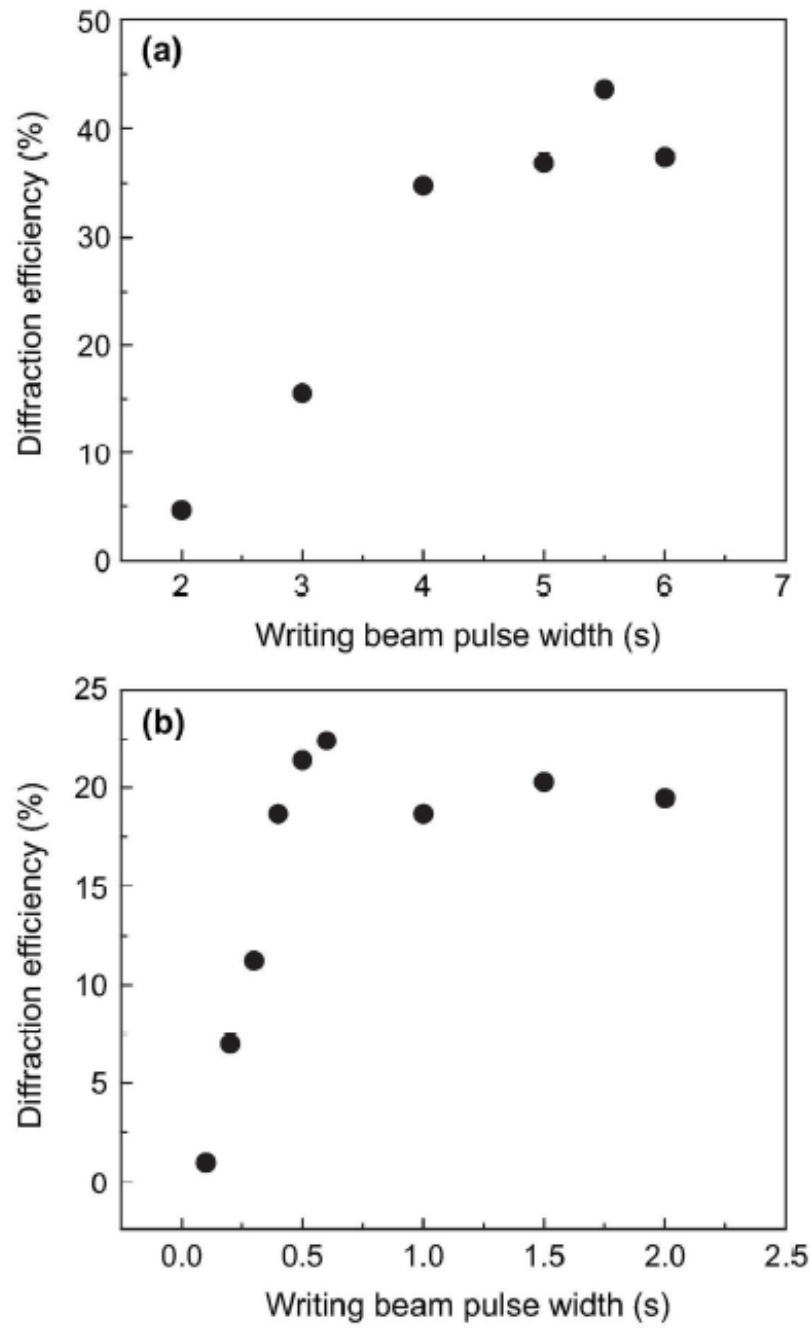


Fig. 5-6. Peak diffraction efficiency in BPII as a function of the writing beam pulse width. (a) Grating spacing: 4 μm ; temperature: 28.8°C; pump beam power: 5 mW. (b) Grating spacing: 2 μm ; temperature: 28.4°C; pump beam power: 15 mW from the reference [12].

Moreover, unlike director axis reorientation or disorder in a nematic liquid crystal (NLC) where strong, highly nonlocal anchoring forces from cell boundaries or unperturbed regions give rise to diminished process efficiency for small grating spacing, distortion in the lattice structure of BPLC can be produced quite efficiently even for small grating spacing. As shown in Fig. 5-7, for the grating spacing dependence of the probe diffraction for similarly doped BPLC and NLC samples, A-BPLC generally yields substantial grating diffraction efficiency for small grating constants on the order of microns, whereas NLC samples yield essentially vanishing values ($< 0.1\%$).

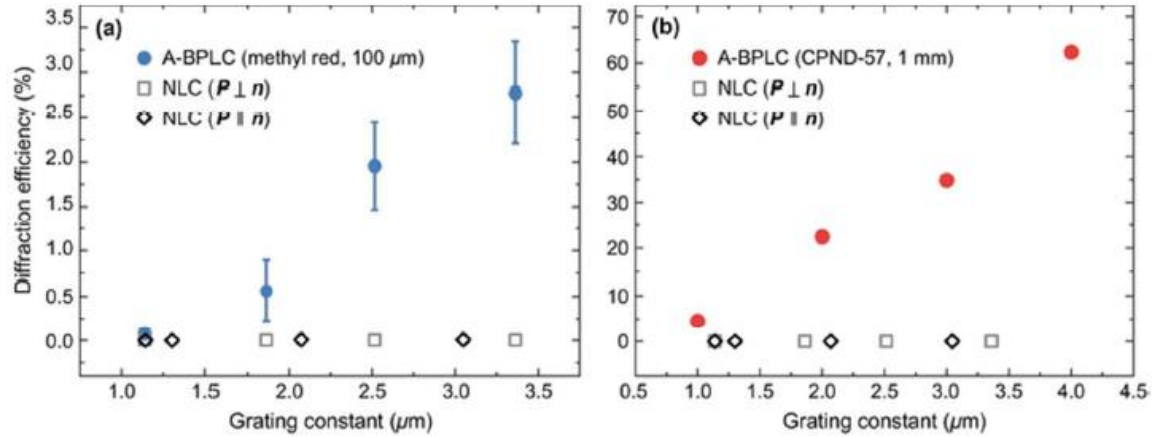


Fig. 5-7. Comparison of the diffraction efficiency from BPLC (BPI near the BPI–BPII transition point) and NLC samples. (Left) Both samples. Thickness: $100\ \mu\text{m}$ thick; dopant: methyl red; pump beam power $\sim 1\ \text{mW}$; probe beam $1.5\ \text{mW}$. (Right): BPLC thickness: $1\ \text{mm}$; NLC thickness: $100\ \mu\text{m}$; dopant: CPND-57 (BPLC), methyl red (NLC). In the case of NLC, the incident laser polarization is set to be parallel (\parallel) or perpendicular (\perp) to the director axis n from the reference [12].

For this azo-dye-doped BPLC, mW-power of the pump beam with diameter of 3 mm was suffice under few seconds duration, and the best diffraction efficiency was obtained from the sample maintained in the temperature range around the BPI-BPII transition, as shown in Fig. 5-8. If operating in the temperature too close to isotropic or in focal conic cholesteric phase, the diffraction signal would be very small. The reason why the diffraction efficiency would be higher in BPII versus BPI was mostly due to the temperature dependence of the photonic band-gap, i.e. the transmission dip. The transmission of 532nm pump beams in BPII was much higher than in BPI (50% versus 10%). According to that, the effective optical power incident into the sample was higher in BPII and, thus, yielded a higher diffraction efficiency.

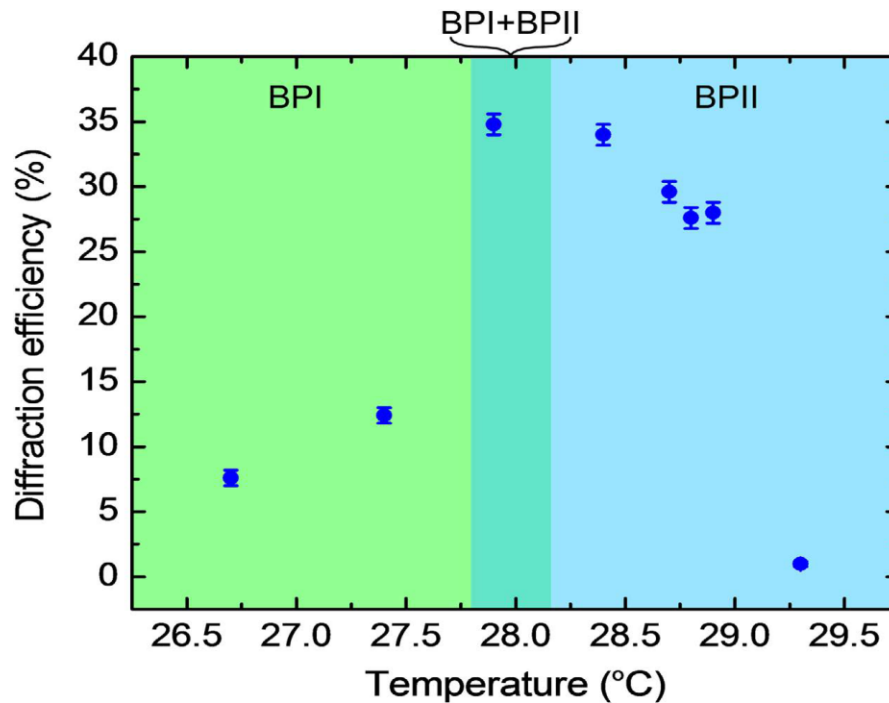


Fig. 5-8. Observed dependence of the maximum Bragg diffraction efficiency on the sample temperature in the BPI-BPII phases. Writing beam powers: 5.5 mW and 4.8 mW; writing time: 2 seconds from the reference [67].

5.4 Optically Prolong Memory Effect

We have observed a very simple way to obtain all-optical means of significantly prolonging the memory of a grating structure written within a short exposure time while keeping the refresh time relatively short [11]. In our first attempt, the purpose was to find a way to speed up the relaxation in order to have fast refreshing and erasure time, which is similar to other holographic recording requirements in photorefractive crystal or photosensitive polymer. Therefore, we kept one of the pump beams on for uniform illumination and expected to erase the grating structure in a shorter time scale. Instead, we observed that the diffraction signal was significantly prolonged by the single reference beam, as the results show in Fig. 5-9. In general, when the pump beams were both off, the diffraction signal continued to build up to maximum and monotonically decayed in a much longer time than the free relaxation. In the BPII phase, such optically prolonged memory with the reference beam kept on lasted over 50 seconds compared to the 5 seconds free relaxation time when both writing beams were turned off. In the BPI phase, we had observed that the decay proceeded at a much slower pace than in the BPII case. In particular, if the grating was allowed to build up to the maximum before the object beam was turned off, the diffraction signal could be held at a steadily unchanged level for a long period until the reference beam was switched off. By varying the initial writing beam power and duration, we had found that this period of steady diffraction signal could last as long as 2 to 3 minutes before experiencing a slow decay to eventually vanishing value.

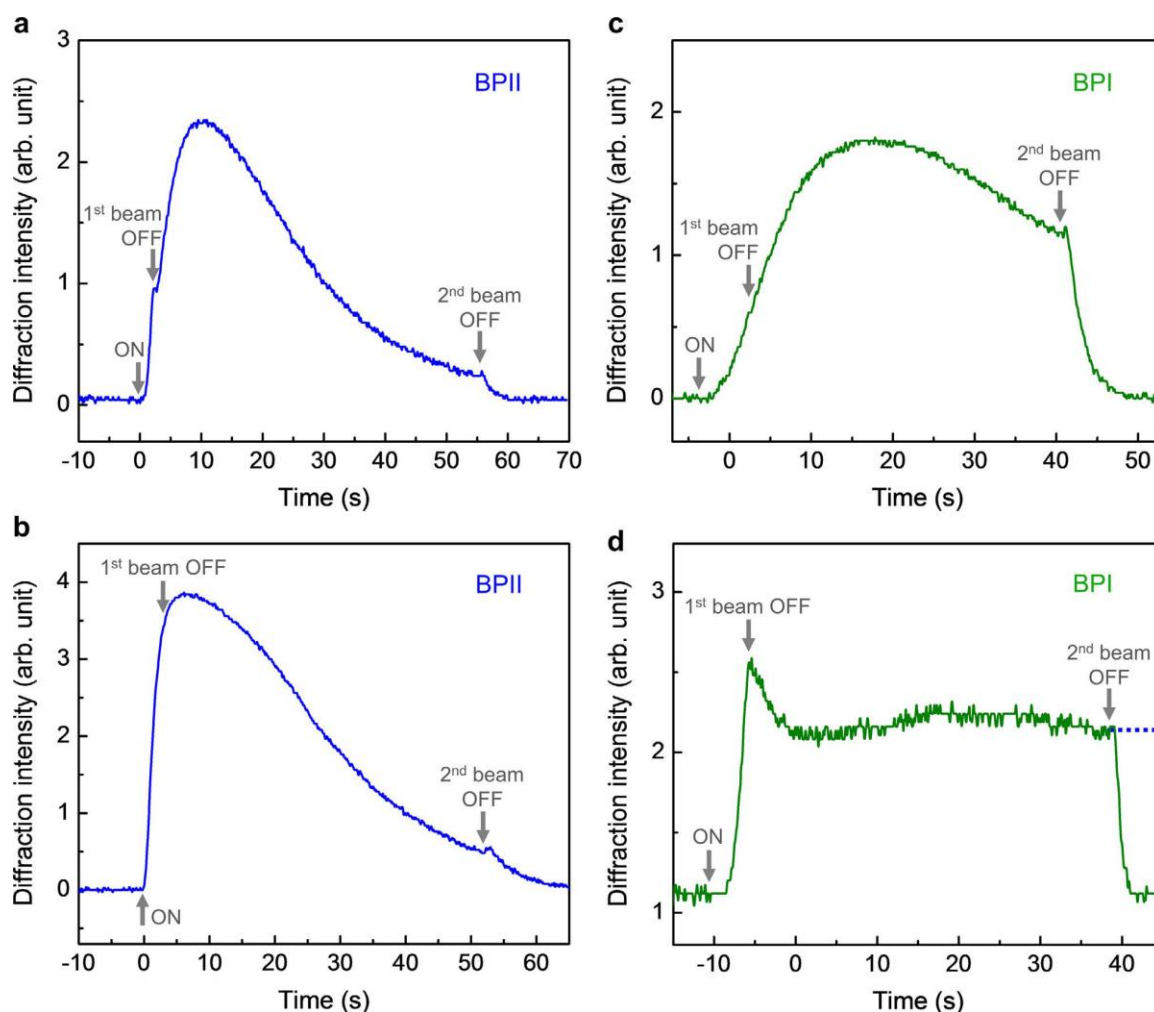


Fig. 5-9. (a) BPII phase, one beam on for 2 seconds and switched off while the other beam is kept on for 55 seconds. Writing beam powers: 2.4 and 2.1 mW. (b) Same as (a) but for writing beam powers: 3.6 and 3.1 mW. (c) BPI phase, one beam on for ~6 seconds and switched off while the other beam is kept on for ~45 seconds. Writing beam powers: 2.4 and 2.1 mW. (d) Same as (c) but for writing beam powers: 3.6 and 3.1 mW. Dotted line indicates how the diffracted signal would persist for another 2 to 3 minutes if the reference beams are not switched off. In all cases, when the second beam is turned off, the diffraction signal disappears in <5 sec from reference [11].

A plausible explanation of this prolonged memory effect is as follows. When both writing beams were turned on, an intensity grating was imparted on the sample and generated a population grating of bent-shaped cis-isomers which created local disorder at the intensity grating maxima (bright regions). At the same time, the excess cis-isomers in this intensity grating maxima migrated towards the intensity minima (dark regions) while relaxing to the oblong-shaped trans-state and caused the surrounding BPLC molecules in the defect regions to undergo coupled flow/reorientation. These local and nonlocal processes resulted in reconfiguration of the defect structure, thus forming a lattice distortion grating and the accompanying index grating to diffract the probe beam. When both writing beams were then turned off, the cis-isomers returned to the ground trans-state in ~ 1 seconds; such fast decaying local disorder was responsible for the observed small abrupt change (upturn) in the diffraction signal. Absent such cis-isomers, the perturbed BPLC molecules underwent a reverse flow-reorientation process to recover the initial defect structure in a characteristic lattice relaxation time of ~ 5 sec, as depicted in Fig. 5-4.

However, if only one of the writing beams was switched off, the other beam that was kept on would then uniformly illuminate the entire region and produce cis-isomers in (previously) dark regions [grating minima] as well as in (previously) bright regions [grating maxima], albeit at a lower rate due to the reduced light level from one beam. Consequently, the lattice distortion associated with the molecular movement and disorder caused by cis-isomers continued to build up in both the bright and dark regions. Because of the prevailing different degrees of lattice distortion between the bright and dark regions, i.e. an index grating formed just before the first beam switch-off, the above-mentioned lattice distortion built up in both regions effectively enhanced the index grating as manifested by the

continued build-up of the diffraction signals after the first beam switch-off. As the uniform illumination by the second beam continued, the index grating reached a saturated level, i.e. maximum diffraction signal, when the lattice distortion in the bright region had fully developed while the distortion in the dark region was still developing. Subsequently, as the distortion in the dark region began to ‘catch up’ with those in the bright region, the resulting index grating was diminished. As shown in Fig. 5-9 (a) (b) for the BPII phase and Fig. 5-9 (c) (d) for the BPI phase, under continuous illumination by the second laser, the time it took for the lattice distortion to equilibrate (corresponding to vanishing index grating and diffraction signal) was considerably longer than the free-relaxation time when both beams were switched off. In this respect, we regarded the uniform illumination as an optical means to frustrate the free-relaxation of the lattice distortion and thus prolong the grating memory. Owing to the different defect structures in the BPI and BPII phase, the former being characterized by multiple separate disclinations which are prone to assume metastable configuration whereas the latter possesses continuous defect structure and undergoes direct transition from one configuration to another, the time it takes for the system to approach final equilibrium configuration in the BPI phase is longer than in the BPII phase.

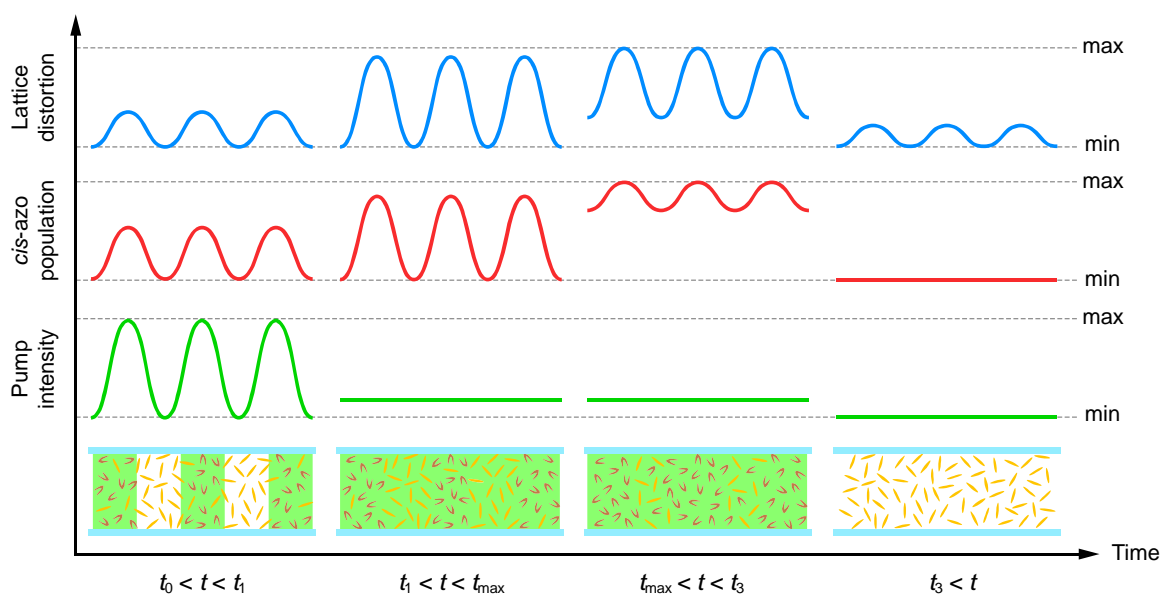


Fig. 5-10. Schematic depiction of the optical intensity grating, cis-isomers population grating, and lattice distortion grating for various time regimes

Figure 5-10 gives a better understanding of the prolonging effect. From t_0 to t_1 , before one or both writing beams were turned off, the excess cis-isomers in the bright regions migrated (diffuse) towards the intensity minima (dark regions) while relaxing to the oblong-shaped trans-state, causing the surrounding molecules to undergo coupled flows/reorientations. These disorder and flow/reorientation processes resulted in reconfiguration of the defect structure, i.e., lattice distortion and, therefore, an index grating. If both writing beams were turned off simultaneously at t_1 before the grating builds up to the maximum, it would continue to rise to the maximum before subsequent decay due to the slow response of the lattice distortion. If they were both turned off after the grating has built up to the maximum, it would simply relax to a vanishing value in a characteristic lattice relaxation time of ~ 5 s. However, if only one of the writing beams was

switched off at t_1 , i.e., the other beam now had a uniform illumination on the entire region and generates cis-isomers in both dark and bright regions, this caused the lattice distortion in both regions to build up for the time interval $t_1 < t < t_{\max}$. As a result of the different degrees of prevailing lattice distortion between the bright and dark regions at time t_1 , such build-up in both regions effectively enhanced the index grating and the diffraction signals. As the uniform illumination continued, the index grating eventually reached a saturated level at t_{\max} , i.e., when the lattice distortion in the bright region had fully developed while the distortion in the dark region was still developing for the time interval. After t_{\max} , i.e., for time $t_{\max} < t < t_3$, the distortion in the dark region began to catch up with the bright region, and the resulting index grating began to slowly diminish until t_3 . When the remaining writing beam was turned off at t_3 , the production of cis-isomers ceased, and the lattice distortion grating decayed to a vanishing value with a free relaxation time constant of a few seconds.

This scenario of molecules' migration and flow/reorientation caused by laser excited trans-cis isomerism of the azo-dopant in A-BPLC's under continuous illumination by a single pump beam is further supported by the following experiments on the transmission spectra, which depict how the photonic bandgap is modified by the laser induced lattice distortion. As shown in Fig. 5-10, for the case of 10 seconds of illumination, the transmission dip was observed to shift from 530 nm to 560 nm; a much longer (1 minute) illumination achieved the same 30 nm shift but an overall increase in the transmission level. The spectral shift was due to lattice distortion and it reached saturation in < 10 sec, whereas the overall increase was attributed to azo-molecule migration away from high to low intensity region following the spatially varying intensity profile of the

Gaussian laser beam. The difference in azo dye concentration also accounted for a different reflection color of the illuminated area (circular pattern) from the surrounding unexposed area, c.f. photo-inserts in Fig. 5-11 taken immediately after the pump beam was removed. The different-colored pattern was observed to persist for tens of seconds to minutes for the sample maintained in the blue-phases, depending on the illumination duration and beam power. We note here that such massive dopant migration and changes in the sample reflection/transmission spectrum was not evident if the illumination time was short (< 10 seconds) and the laser power was low (\sim a few mW or less). For holographic recording purposes, therefore, prolonged writing time and/or high beam power not only are unnecessary but also could lead to deleterious effects.

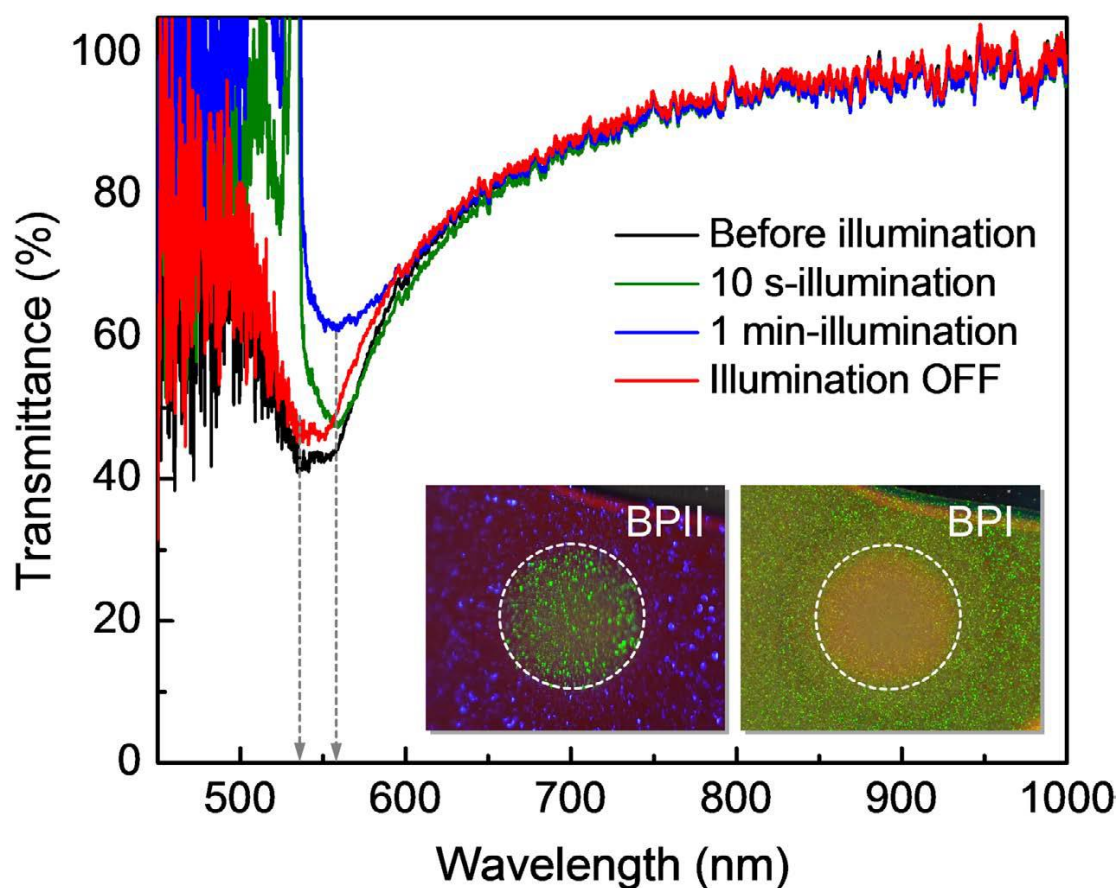


Fig. 5-11. Transmission spectra exhibiting photonic bandgap (transmission dips) of the 1-mm thick A-BPLC sample illuminated by a 532-nm pump beam intensity $\sim 15 \text{ mW/cm}^2$ (pump power $\sim 1.5 \text{ mW}$). The spectra are normalizing with the transmission spectrum of the sample in the isotropic (liquid) phase. Photo inserts show the different reflection colors from the regions under prolonged laser illumination at higher pump intensity $\sim 80 \text{ mW/cm}^2$ for BPI and BPII phase, obtained from reference [11].

5.5 Phase Conjugation Using A-BPLC

We have conducted several all-optical image processing operations by exploiting these unusual responses and advantages of A-BPLC. Figure 5-12 (a) depicts the experimental setup for optical phase conjugation that allows holographic recording and aberration-free image reconstruction [69, 76, 78, 79].

For this study, an Air Force resolution chart was placed in the path of one of the pump beams and acted as an object beam, as shown in Fig. 5-12 (b). The object beam intersected at the sample to record a hologram with the coherent reference beam, which was derived from the same laser as the object beam. The transmitted reference beam was retro-reflected to ‘read’ the holographic interference pattern and generated an image beam that counter-propagated to the object beam. Viewing of the reconstructed image was made easy by utilizing the prolonged grating lifetime effect discussed previously. We employed a screen that initially allowed both object and reference beams to pass to write the hologram for ~1 s.; the screen was then moved to block the object beam and allow only the reference beam and its retro-reflection acting as the reading beam to be incident on the recorded hologram. The reconstructed image/diffraction coming from the sample in the reverse direction to the object beam and lasted several tens of seconds due to continuous illumination by the reference, and reading beams were captured by the beam splitter and photographed. Figure 5-12 (c) shows the reconstructed image. To demonstrate the well-known ability of optical phase conjugation process to compensate for aberration experienced by the object beam, a corrugated plastic sheet was placed in the path of the

object beam, *cf.* Fig. 5-12 (d), which shows very severe distortion. As clearly shown in Fig. 5-12 (e), the phase conjugated signal, which retraced the path of the object beam through the aberration, emerged with most of the aberration compensated and closely resembled the undistorted image shown in Fig. 5-12 (c).

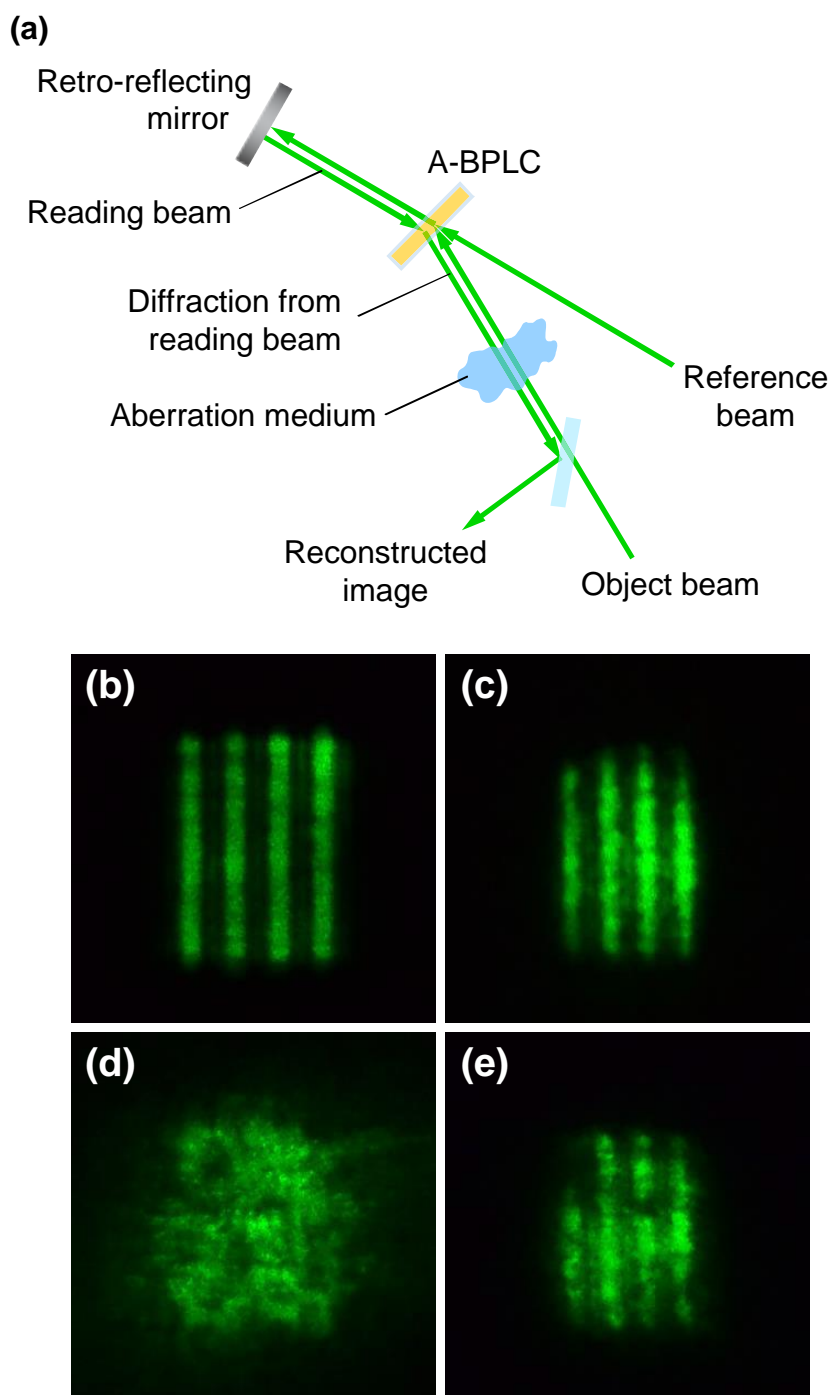


Fig. 5-12. (a) Schematic depiction of the experimental setup for optical phase conjugation by degenerate four wave mixing in A-BPLC. (b) Photograph of the input object. (c) Reconstructed image without the aberration. (d) Input object beam after traversing the corrugated plastic film exhibiting severe aberration. (e) Reconstructed image that demonstrates the ability of optical phase conjugation to correct for the aberration from reference [12].

Chapter 6

Conclusion and Future Work

6.1 Optical Limiting with BPLC

As discussed in Chapter 3, undoped blue-phase liquid crystals exhibit ultrafast optical nonlinear responses under picosecond laser pulses. This result makes the material one of the promising candidates for optical limiting applications. Without further investigation, we demonstrated that undoped BPLCs are able to largely attenuate the picosecond laser pulse train due to the lattice distortion and flow-orientation induced by Maxwell stress. This effect was done before by using nematic liquid crystals. However, BPLC provides a more efficient and feasible way for optical limiting with the properties of polarization-free and incident angle dependence.

A practical application of using liquid crystal as an optical limiting device is the nonlinear fiber imaging faceplates as depicted in Fig. 6-1 [10]. Placing the faceplates in an imaging system, one can have fully transmitted, low intensity light from the device, but the high intensity incident light, such as a laser pulse, will be self-attenuated, significantly owing to the high optical nonlinearity of BPLC.

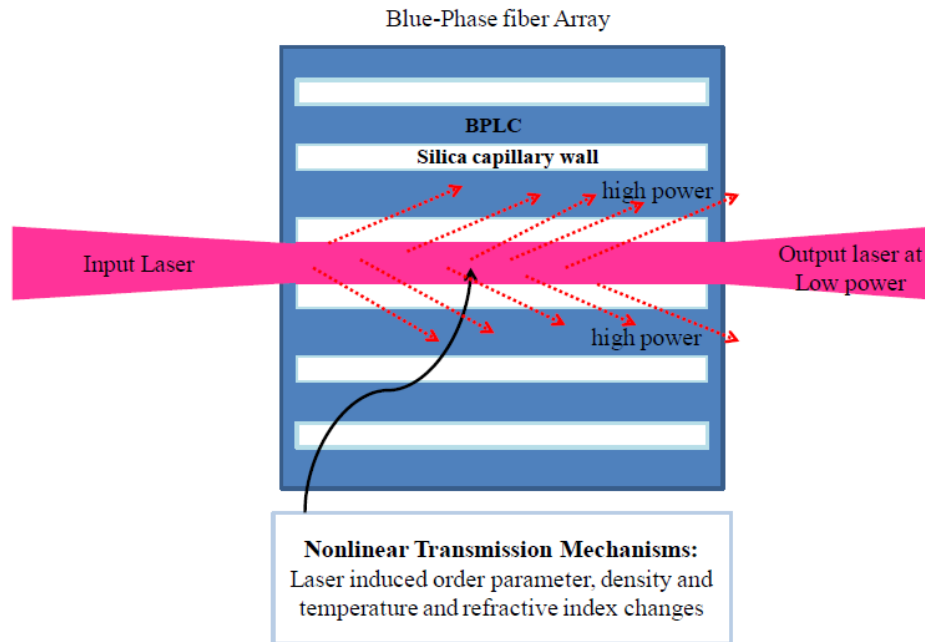


Fig. 6-1. Schematic depiction of the various mechanisms that could come into play in affecting the transmission of a laser pulse through a BPLC cored constituent fiber in a BPLC fiber array for passive sensor protection applications[10].

For the future work, we can use the new tunable-wavelength picosecond laser to investigate the nonlinear dynamical responses in undoped and doped blue-phase liquid crystals in all-optical wavelength range. With BPLCs, we are able to demonstrate faster, polarization-free all-optical switching and limiting.

6.2 Fast Optical Response with Bragg Grating In BPLC

In Chapter 5, we demonstrated that the photosensitive azo-dye-doped BPLCs are capable of high-efficiency holographic recording with memory that can be prolonged from a few seconds to several minutes by uniform illumination with the reference beam. Unlike Raman-Nath grating, operating in the Bragg grating regime provides much higher grating efficiency—up to 50 times improvement as compared to previous studies. The mechanism here is BPLC's lattice distortion and index modulation caused by azo-dopant, which means the azo-dye provides coupled flow and orientation under laser illumination and lead to lattice distortion.

Yet, the optical set up still requires optimization as well as the dopant choice and sample quality. With higher quality mirrors and more precise optical path, we expect higher efficiency, which is more suitable for holographic recording and display applications. Furthermore, one can try to apply different laser systems, such as the microsecond pulse laser and the tunable-wavelength picosecond laser, in order to study the fast optical nonlinear responses of azo-dye-doped BPLC. Using a laser system having better coherent length and beam profiles, we will be able to demonstrate better performance on various applications, such as holographic recording and phase conjugation.

6.3 Theoretical Simulation

In Chapter 2, the general discussion on the free energy theory in BPLC was shown. The Oseen-Frank theory is able to calculate the minimum free energy in certain temperatures and the elastic constant of BPLC. However, this discussion is not enough to understand the liquid crystalline dynamic under the electrical and optical fields. Blue-phases provide a fascinating example of liquid crystal ordering as they correspond to complicate director fields which connect by a network of disclinations. Therefore, in Landau-de Gennes theory, the director fields can be used to define a traceless, symmetric and second rank tensor:

$$Q_{\alpha\beta} = \frac{2S}{3}(n_\alpha n_\beta - \frac{1}{3}\delta_{\alpha\beta}) \quad (6-1)$$

where S represents the magnitude of the liquid crystalline order with the value between 0 and 1. The Q tensor described by Landau-de Gennes is powerful and able to simulate the equilibrium of blue-phases [29, 80].

In the Landau-de Gennes theory, the free energy comprises a bulk term F_b and a distortion term F_d :

$$F_b = \frac{A_0}{2} \left(1 - \frac{\gamma}{3}\right) Q_{\alpha\beta}^2 - \frac{A_0\gamma}{3} Q_{\alpha\beta} Q_{\beta\gamma} Q_{\gamma\alpha} + \frac{A_0\gamma}{4} (Q_{\alpha\beta}^2)^2 \quad (6-2)$$

$$F_d = \frac{K}{2} [(\partial_\beta Q_{\alpha\beta})^2 + (\epsilon_{\alpha\zeta\delta} \partial_\zeta Q_{\delta\beta} + 2q_0 Q_{\alpha\beta})^2], \quad (6-3)$$

where K is an elastic constant, $q_0 = 2\pi/p$, p is the pitch of the cholesteric liquid crystals, A_0 is a constant, and γ controls the order of magnitude. By adding the external electric field term $-(\varepsilon_a/12\pi)E_\alpha Q_{\alpha\beta}E_\beta$ and the certain boundary condition, the hydrodynamic simulation of BPLC under electric fields was demonstrated in [52]. The goal for us is to insert the optical field term in the Landau-de Gennes theory in order to understand the optical nonlinear effect and the hydrodynamic in the un-doped and doped blue-phase liquid crystals. It is important to simulate the blue-phases dynamic under the all-range optical fields and study the molecules flow and orientation to prove the previous experimental results.

References

1. Reinitzer, F., *Beiträge zur Kenntnis des Cholesterins*. Monatshefte für Chemie, 1888. **9**:421–41.
2. Frank, F.C., *I. Liquid crystals. On the theory of liquid crystals*. Discussions of the Faraday Society, 1958. **25**: p. 19-28.
3. Lin, Y.-H., et al., *Polarizer-free and fast response microlens arrays using polymer-stabilized blue phase liquid crystals*. Applied Physics Letters, 2010. **96**(11): p. 113505.
4. Yang, D.-K., *Fundamentals of liquid crystal devices*. 2014: John Wiley & Sons.
5. Kikuchi, H., et al. 62.2: *Invited Paper: Fast Electro-Optical Switching in Polymer-Stabilized Liquid Crystalline Blue Phases for Display Application*. in *SID Symposium Digest of Technical Papers*. 2007. Wiley Online Library.
6. Wu, S.-T. and D.-K. Yang, *Reflective liquid crystal displays*. 2001: Wiley.
7. Ito, M., et al., *Structure, transmission type liquid crystal display, reflection type display and manufacturing method thereof*. 2007, Google Patents.
8. Lee, S., S. Lee, and H. Kim, *Electro-optic characteristics and switching principle of a nematic liquid crystal cell controlled by fringe-field switching*. Applied physics letters, 1998. **73**(20): p. 2881-2883.
9. Clark, N.A. and S.T. Lagerwall, *Submicrosecond bistable electro-optic switching in liquid crystals*. Applied Physics Letters, 1980. **36**(11): p. 899-901.
10. I. C. Khoo, S.Z., Chun-Wei Chen and Tsung-Jui Ho, *Maxwell Stress Induced Flow-Deformation and Optical Nonlinearities in Liquid Crystals*. Progress In Electromagnetics Research, 2015. **154**: p. 51–63.
11. Khoo, I.C., C.-W. Chen, and T.-J. Ho, *High efficiency holographic Bragg grating with optically prolonged memory*. Scientific reports, 2016. **6**: p. 36148.
12. Ho, T.-J., C.-W. Chen, and I.C. Khoo, *Polarization-free and high-resolution holographic grating recording and optical phase conjugation with azo-dye doped blue-phase liquid crystals*. Submitted to Liquid Crystal Review 2018.
13. Ericksen, J.L., *Continuum theory of liquid crystals of nematic type*. Molecular crystals and liquid crystals, 1969. **7**(1): p. 153-164.
14. De Gennes, P., J. Prost, and R. Pelcovits, *The physics of liquid crystals*. Physics Today, 1995. **48**: p. 70.
15. Tsvetkov, W., W. Tsvetkov, *Acta Physicochim.* 11, 97 (1939). Acta Physicochim., 1939. **11**: p. 97.
16. Khoo, I.C., *Nonlinear optics of liquid crystalline materials*. Physics Reports, 2009. **471**(5-6): p. 221-267.
17. Khoo, I.C., *Liquid Crystals, 2nd Ed.* 2007.
18. Yariv, A., *Introduction to optical electronics*. 1976.
19. Franken, e.P., et al., *Generation of optical harmonics*. Physical Review Letters, 1961. **7**(4): p. 118.

20. Yariv, A. and P. Yeh, *Optical waves in crystals*. Vol. 5. 1984: Wiley New York.
21. Hwang, J., et al., *Enhanced optical nonlinearity near the photonic bandgap edges of a cholesteric liquid crystal*. Optics letters, 2004. **29**(22): p. 2644-2646.
22. Khoo, I.C. and S. Zhao, *Multiple time scales optical nonlinearities of liquid crystals for optical-terahertz-microwave applications (Invited Review)*. Progress In Electromagnetics Research, 2014. **147**: p. 37-56.
23. Khoo, I., et al., *Optically induced space-charge fields, dc voltage, and extraordinarily large nonlinearity in dye-doped nematic liquid crystals*. Optics letters, 1998. **23**(4): p. 253-255.
24. Ikeda, T. and O. Tsutsumi, *Optical switching and image storage by means of azobenzene liquid-crystal films*. Science, 1995. **268**(5219): p. 1873-1875.
25. Lin, T.-H., C.-W. Chen, and Q. Li, *Self-Organized 3D Photonic Superstructure: Blue Phase Liquid Crystal*, in *Anisotropic Nanomaterials*. 2015, Springer. p. 337-378.
26. Leslie, F., *Theory of flow phenomena in liquid crystals*, in *Advances in liquid crystals*. 1979, Elsevier. p. 1-81.
27. Meiboom, S., M. Sammon, and W. Brinkman, *Lattice of disclinations: The structure of the blue phases of cholesteric liquid crystals*. Physical Review A, 1983. **27**(1): p. 438.
28. Meiboom, S., et al., *Theory of the blue phase of cholesteric liquid crystals*. Physical Review Letters, 1981. **46**(18): p. 1216.
29. Wright, D.C. and N.D. Mermin, *Crystalline liquids: the blue phases*. Reviews of Modern physics, 1989. **61**(2): p. 385.
30. Dierking, I., *Textures of liquid crystals*. 2003: John Wiley & Sons.
31. Brinkman, W.F. and P.E. Cladis, *Defects in liquid crystals*. Physics Today, 1982. **35**(5): p. 48-54.
32. Yang, D. and P. Crooker, *Chiral-racemic phase diagrams of blue-phase liquid crystals*. Physical Review A, 1987. **35**(10): p. 4419.
33. Blu, T., et al., *Phase diagrams of the blue phases*. Chemical physics letters, 1985. **116**(6): p. 529-533.
34. Hornreich, R. and S. Shtrikman, *Landau theory of blue phases*. Molecular Crystals and Liquid Crystals, 1988. **165**(1): p. 183-211.
35. Grebel, H., R. Hornreich, and S. Shtrikman, *Landau theory of cholesteric blue phases: The role of higher harmonics*. Physical Review A, 1984. **30**(6): p. 3264.
36. Grebel, H., R. Hornreich, and S. Shtrikman, *Landau theory of cholesteric blue phases*. Physical Review A, 1983. **28**(2): p. 1114.
37. Berreman, D.W. and S. Meiboom, *Tensor representation of Oseen-Frank strain energy in uniaxial cholesterics*. Physical Review A, 1984. **30**(4): p. 1955.
38. Miller, M.J., A.G. Mott, and B.P. Ketchel. *General optical limiting requirements*. in *SPIE's International Symposium on Optical Science, Engineering, and Instrumentation*. 1998. SPIE.
39. Tutt, L.W. and T.F. Boggess, *A review of optical limiting mechanisms and devices using organics, fullerenes, semiconductors and other materials*. Progress in Quantum Electronics, 1993. **17**(4): p. 299-338.
40. America, L.I.o., *American National Standard for Safe Use of Lasers*, in

2007: American National Standards Institute, Inc. .

41. Hoffman, R.C., et al., *Reverse saturable absorbers: indanthrone and its derivatives*. Journal of the Optical Society of America B, 1989. **6**(4): p. 772-777.
42. Tutt, L.W. and A. Kost, *Optical limiting performance of C60 and C70 solutions*. Nature, 1992. **356**: p. 225.
43. Khoo, C., H. Li, and Y. Liang, *Observation of orientational photorefractive effects in nematic liquid crystals*. Optics letters, 1994. **19**(21): p. 1723-1725.
44. Eichler, H.J. and R. Macdonald, *Flow-alignment and inertial effects in picosecond laser-induced reorientation phenomena of nematic liquid crystals*. Physical Review Letters, 1991. **67**(19): p. 2666-2669.
45. Jackson, J.D., *Classical Electrodynamics*. 1975.
46. Khoo, I.C., J. Liou, and M.V. Stinger, *Microseconds–Nanoseconds All-Optical Switching of Visible-Near Infrared (0.5 μm –1.55 μm) Lasers with Dye-Doped Nematic Liquid Crystals*. Molecular Crystals and Liquid Crystals, 2010. **527**(1): p. 109/[265]-118/[274].
47. Khoo, I.C., et al., *Ultrafast All-Optical Switching with Transparent and Absorptive Nematic Liquid Crystals–Implications in Tunable Metamaterials*. Molecular Crystals and Liquid Crystals, 2011. **543**(1): p. 151/[917]-159/[925].
48. Khoo, I.-C., J.-H. Park, and J.D. Liou, *Theory and experimental studies of all-optical transmission switching in a twist-alignment dye-doped nematic liquid crystal*. Journal of the Optical Society of America B, 2008. **25**(11): p. 1931-1937.
49. Chen, C.-W., T.-H. Lin, and I.C. Khoo, *Dynamical studies of the mechanisms for optical nonlinearities of methyl-red dye doped blue phase liquid crystals*. Optics Express, 2015. **23**(17): p. 21650-21656.
50. Khoo, I.C., et al., *Blue-phase liquid crystal cored optical fiber array with photonic bandgaps and nonlinear transmission properties*. Optics Express, 2013. **21**(4): p. 4319-4328.
51. Khoo, I.C. and T.-H. Lin, *Nonlinear optical grating diffraction in dye-doped blue-phase liquid crystals*. Optics Letters, 2012. **37**(15): p. 3225-3227.
52. Tiribocchi, A., et al., *Switching dynamics in cholesteric blue phases*. Soft Matter, 2011. **7**(7): p. 3295-3306.
53. Tsung-Hsien, L., et al., *Red, Green and Blue Reflections Enabled in an Optically Tunable Self-Organized 3D Cubic Nanostructured Thin Film*. Advanced Materials, 2013. **25**(36): p. 5050-5054.
54. Khoo, I.C., et al., *Nonlinear Optics of Nematic and Blue Phase Liquid Crystals*. Molecular Crystals and Liquid Crystals, 2014. **594**(1): p. 31-41.
55. Khoo, I.C., C.-W. Chen, and T.-J. Ho, *Observation of photorefractive effects in blue-phase liquid crystal containing fullerene-C60*. Optics Letters, 2016. **41**(1): p. 123-126.
56. Khoo, I.C., *Orientational photorefractive effects in nematic liquid crystal films*. IEEE Journal of Quantum Electronics, 1996. **32**(3): p. 525-534.
57. Rudenko, E. and A. Sukhov, *Optically induced spatial charge separation in a nematic and the resultant orientational nonlinearity*. JETP, 1994. **105**: p. 1621-1634.

58. Khoo, I., et al., *Coherent beam amplification with a photorefractive liquid crystal*. Optics letters, 1997. **22**(16): p. 1229-1231.
59. Khoo, I., et al., *Extremely nonlinear photosensitive liquid crystals for image sensing and sensor protection*. Optics Express, 1999. **4**(11): p. 432-442.
60. Sasaki, T., et al., *Real-time dynamic hologram in photorefractive ferroelectric liquid crystal with two-beam coupling gain coefficient of over 800 cm⁻¹ and response time of 8 ms*. Applied Physics Letters, 2013. **102**(6): p. 31.
61. Sasaki, T. and Y. Naka, *Dynamic amplification of optical signals in photorefractive ferroelectric liquid crystals*. Molecular Crystals and Liquid Crystals, 2015. **614**(1): p. 106-117.
62. Ashkin, A., et al., *OPTICALLY-INDUCED REFRACTIVE INDEX INHOMOGENEITIES IN LiNbO₃ AND LiTaO₃*, in *Landmark Papers On Photorefractive Nonlinear Optics*. 1995, World Scientific. p. 29-31.
63. Günter, P., J.-P. Huignard, and A.M. Glass, *Photorefractive materials and their applications*. Vol. 1. 1988: Springer.
64. Khoo, I., *Holographic grating formation in dye-and fullerene C₆₀-doped nematic liquid-crystal film*. Optics letters, 1995. **20**(20): p. 2137-2139.
65. Khoo, I. and T.-H. Lin, *Nonlinear optical grating diffraction in dye-doped blue-phase liquid crystals*. Optics letters, 2012. **37**(15): p. 3225-3227.
66. Khoo, I.C., *DC-field-assisted grating formation and nonlinear diffractions in methyl-red dye-doped blue phase liquid crystals*. Optics letters, 2015. **40**(1): p. 60-63.
67. Khoo, I.C., *Nonlinear optics of liquid crystalline materials*. Physics Reports, 2009. **471**(5): p. 221-267.
68. Hesselink, L., S.S. Orlov, and M.C. Bashaw, *Holographic data storage systems*. Proceedings of the IEEE, 2004. **92**(8): p. 1231-1280.
69. Huignard, J.-P. and P. Günter, *Optical processing using wave mixing in photorefractive crystals*, in *Photorefractive Materials and Their Applications II*. 1989, Springer. p. 205-273.
70. Ostroverkhova, O. and W. Moerner, *Organic photorefractives: mechanisms, materials, and applications*. Chemical reviews, 2004. **104**(7): p. 3267-3314.
71. Solyman, L. and D.J. Cooke, *Volume Holography and Volume Gratings: L. Solyman and D.J. Cooke*. 1981: Academic press.
72. Tay, S., et al., *An updatable holographic three-dimensional display*. Nature, 2008. **451**(7179): p. 694.
73. Yoneyama, S., et al., *High-performance material for holographic gratings by means of a photoresponsive polymer liquid crystal containing a tolane moiety with high birefringence*. Macromolecules, 2002. **35**(23): p. 8751-8758.
74. De Sio, L., et al., *Mesogenic versus non-mesogenic azo dye confined in a soft-matter template for realization of optically switchable diffraction gratings*. Journal of Materials Chemistry, 2011. **21**(19): p. 6811-6814.
75. Zheng, Z.-g., et al., *Three-dimensional control of the helical axis of a chiral nematic liquid crystal by light*. Nature, 2016. **531**(7594): p. 352.

76. Khoo, I.C., et al., *Dye-doped photorefractive liquid crystals for dynamic and storage holographic grating formation and spatial light modulation*. Proceedings of the IEEE, 1999. **87**(11): p. 1897-1911.
77. Caputo, R., et al., *Development of a new kind of switchable holographic grating made of liquid-crystal films separated by slices of polymeric material*. Optics letters, 2004. **29**(11): p. 1261-1263.
78. Khoo, I.-C., *Dynamic gratings and the associated self diffractions and wavefront conjugation processes in nematic liquid crystals*, in *Optical Effects in Liquid Crystals*. 1986, Springer. p. 214-221.
79. White, J.O. and A. Yariv, *Real-time image processing via four-wave mixing in a photorefractive medium*, in *Landmark Papers On Photorefractive Nonlinear Optics*. 1995, World Scientific. p. 455-457.
80. Dupuis, A., D. Marenduzzo, and J. Yeomans, *Numerical calculations of the phase diagram of cubic blue phases in cholesteric liquid crystals*. Physical Review E, 2005. **71**(1): p. 011703.

VITA

Tsung-Jui Ho

Education:

The Pennsylvania State University, University Park, PA

2014-2018

Ph.D. Electrical Engineering.

GPA: 3.74

National Chung Cheng University, Taiwan

2009 – 2013

Bachelor's degree in physics

Publication and conference presentation:

TJ HO, CW Chen, IC Khoo. *"Polarization-free and high-resolution holographic grating recording and optical phase conjugation with azo-dye doped blue-phase liquid crystals"* Submitted to Liquid Crystal Review 2018.

IC Khoo, CW Chen, TJ Ho. *"Normally Transparent Liquid-Crystal Smart Glass for Augmented Reality Head-Up Displays"* OSA FiO/LS 2017.

TJ HO, IC Khoo, CW Chen *"Azo-blue phase liquid crystals for high efficiency holographic Bragg grating with optically prolonged memory"* SPIE Optics + Photonics 2017, San Diego, USA, 2017.

IC Khoo, CW Chen, TJ Ho, TH Lin. *"Femtoseconds-picoseconds nonlinear optics with nearly-mm thick cholesteric liquid crystals"* SPIE OPTO, 2017

I.C. Khoo, C.-W. Chen, and T.-J. Ho. *"High efficiency holographic Bragg grating with optically prolonged memory."* Scientific Reports 6 (2016): 36148.

I.C. Khoo, C.-W. Chen, and T.-J. Ho, *"Observation of photorefractive effects in Blue-phase liquid crystal containing Fullerene-C60"* Opt. Lett. 41, 123-126 (2016).

I. C. Khoo, S. Zhao, T.-J. Ho and C.-W. Chen, *"Maxwell Stress induced flow- deformation and optical nonlinearities in liquid crystals,"* Progress in Electromagnetic Research [Invited paper for commemorative issue on 150 years of Maxwell Equations] Vol. 154, 51-63, 2015.

C.-W. Chen, I. C. Khoo, S. Zhao, T.-H. Lin, and T.-J. Ho, *"Studies of the underlying mechanisms for optical nonlinearities of blue phase liquid crystals,"* SPIE Optics + Photonics 2015.

I. C. Khoo, T. J. Ho, C. W. Chen and T. H. Lin, *"New Nonlinear Optics Possibilities with Blue Phase Liquid Crystals,"* Nonlinear Optics Conference, Kauai, Hawaii 7/2015.